Dissertation

Large-scale light-sheet imaging in combination with versatile clearing and labeling methods provides systemic and high-resolution insight into whole animal nervous systems

Ausgeführt zum Zwecke der Erlangung des akademischen Grades

des Doktors der Naturwissenschaften unter der Leitung von

Dipl.Phys. Univ.Prof. Dr. Dodt Hans-Ulrich

der Fakultät für Elektrotechnik und Informationstechnik

am Institut für Festkörperelektronik E362

der Technischen Universität Wien

von

Marko Pende M.Sc. M.Sc. B.Sc.

Matrikelnummer: 00706330

Wien, Juni 2020

„Deine Zukunft ist, wozu du sie machen willst. Zukunft heißt wollen.“

Dalai Lama

Acknowledgments

First of all, I wish to express my sincere gratitude to my supervisor Dipl.Phys. Univ.Prof. Dr. Hans-Ulrich Dodt for giving me the opportunity to work in his laboratory on my dissertation. He was very patient with me and he was there when I needed help, and I am very thankful for his support and for believing in me.

Especially I want to thank Dr. Klaus Becker and Dr. Saiedeh Saghafi. I am very grateful and lucky to have helping colleagues with whom I can work but also laugh a lot. They provided valuable insight into my topic and shared their knowledge openly.

Furthermore, I want to thank my colleagues: Dr. Christan Hahn, Massih Foroughipour, Meraaj Foroughipour, Julia Gaugeler, Anna Tröscher PhD, Dr. Monika Bradl, Dr. Jan Bauer, Dr. Petra Scholze, Maria Eleni Kastriti PhD, Prof. Igot Adameyko, Prof. Tibor Harkany, Prof. Thomas Klausberger, Prof. Hans Lassmann, Dr. Roni Hogri, Dr. Sigismund Huck, Gilbert Janeselli, Geisbichler Sabine, Mira Kronschläger PhD, Ulrike Köck, Marianne Leisser, Balint Lasztoczi PhD, Hugo Malagon-Vina PhD, Dr. Roman Romanov, Teuchmann Hannah, Prof. Johannes Berger, Regina Hirnschall, Hadschief Viktoria, Alexandra Tilscher, Ivan Lazarov Anov, Dr. Sonja Forss-Petter, Bahar Camurdanoglu PhD, Laura Geid, Prof. Thomas Hummel, Tobias Zrzavy PhD, Prof. Florian Raible, Akane Kawaguchi PhD, Pak Kin Lou (Willson) PhD, Wouter Masselink PhD, Pietro Tradivo, Dr. Elly Margaret Tanaka, Daniel Reumann PhD, Lijuan Zhang PhD, Ruwen Schulz, Dr. Eike Budinger, Oliver Kobler, Julia Henschke PhD, Dr. Oleg Simakov, Hannah Schmidbaur, Logan Hodgkiss, James Oakes PhD and Karin Aumayr for very interesting and inspiring talks, new ideas and occasional help.

My special gratitude belongs to Rashmid Kaur PhD, Karim Vadiwala, Prayag Murawala PhD, Marcus Dekens PhD, Pawel Pasierbek PhD and my student Alma Avdibasic who supported me during practical work and for vivid discussions.

I am very thankful to my non-work related friends Rares Bogdan, Andrada Man, Georg Schwarzecker, Michael Radner, Alexander Ursel, Veronika Plichta (Christina) PhD, Caro Wild PhD and Raphi Wild PhD, Mihaela Rasonja, Manfred Meisterl and Philipp Gal

I want to thank my girlfriend Sofia Christina Papadopoulos, who has always supported and helped me to manage my degree. Sometimes a smile of her was enough to let me forget my worries. Her dark humor and sarcasm are like a nice cold glass of water on a hot summer day. She calmed me down when I was hotheaded and gave me reason when I was unreasonable. I can consider myself happy to have her.

I am very thankful to Tomislav and Marina - you are the best parents one can wish for. You were always there in time of despair to build me up and motivate me to continue. Starting from primary school when I was too stupid to form nice little balls out of silk paper in order to glue them on a paper in a fish shape, to the moment where I failed a class in high school. You protected and supported me whenever needed. You were perfect traveling buddies on multiple diving and cultural trips all around the world. Mama, Tata you are my rocks in the stormy sea and I love you. I also want to thank my little sister Nika (aka Dr. Kätzchen) and her husband Olivier Carree (aka Maslinko), whom I regard as a brother. Nika, I enjoyed every minute when the two of us were studying till late at night for our exams. You corrected all my posters, presentations and written texts, helping me even when you did not have time for yourself. It meant a lot to me when you participated in my first paper and I am very happy to have your name on it. I share with you so much of my interests and respect you deeply as a person and successful scientist. I am still dreaming of somehow combing our scientific fields one day. Nika you are the best sister in the world.

Zusammenfassung

Einleitung: Das Ziel dieser Arbeit war es Klärungsmethoden zu entwickeln und bestehende Methoden zu verbessern, die eine hohe Transparenz bei Proben erzielen können, während sie die Morphologie des Gewebes nicht beeinträchtigen und kompatibel mit verschiedenen molekularen Markierungsmethoden sind, wie z.B. transgenes Fluoreszenzsignal, Immunohistochemie und RNA *in situ* Hybridisierung. Diese Klärungsmethoden sollten die 3D Systemuntersuchung (vom einzelnen Organ bis zum ganzen Tier) von verschiedenen Modellorganismen ermöglichen. Diese wären Maus (*mus musculus*), Zebrafisch (*danio rerio*), Fruchtfliege (*Drosophila melanogaster*), Axolotl (*Axolotl mexicanum*), Borstenwurm (*Platynereis dumerilii*), Hawaiianischer Bobtail-Tintenfisch (*Euprymna scolopes*) und der Langflossen-Küstenkalmar (*Doryteuthis pealeii*).

Methodologie: [1] Die wasserbasierende CLARITY und CUBIC, als auch die auf Dehydration basierende 3DISCO Klärungsmethode wurden an den Gehirnen von transgenen Thy1-GFP-M und Thy1-YFP-H Mäusen getestet und nach den folgenden Kriterien evaluiert: (i) Schwierigkeit der Implementierung, (ii) Toxizität, (iii) Klärungseigenschaften, (iv) Zeitaufwand, (v) Morphologieerhalt, (vi) Eigenschaften des Refraktionsindex (RI) angleichenden Mediums, (vii) Erhalt und Langzeitstabilität des Fluoreszenzsignals und (viii) die allgemeinen Kosten. Zum Schluss wurden neue Chemikalien getestet um die zuvor erwähnten Eigenschaften zu verbessern.

[2] Die auf Wasser basierenden Methoden ScaleS und CUBIC und die dehydrationsbasierende Klärungsmethode 3DISCO wurden an verschiedenen transgenen *Drosophila melanogaster* (Fruchtfliege) getestet und nach den folgenden Kriterien evaluiert: (i) Klärungseigenschaften, (ii) Morphologieerhalt, (iii) Eigenschaften des RI angleichenden Mediums, (iv) Depigmentierungsfähigkeit und (v) Erhalt und Langzeitstabilität des Fluoreszenzsignals.

[3] Das wasserbasierende FlyClear Protokoll wurde getestet an Wildtypen und in manchen Fällen auch an transgenen Mäusen, Axolotln, Zebrafischen, Borstenwürmern, Hawaiianischen Bobtail-Tintenfischen und Langflossen-Küstenkalmaren auf (i) Klärungseigenschaften, (ii) Morphologieerhalt, (iii) Eigenschaften des RI angleichenden Mediums, (iv) Depigmentierungsfähigkeit, (v) Erhalt und Langzeitstabilität des Fluoreszenzsignals und Kompatibilität mit molekularen Markierungsmethoden wie z.B Immunhistochemie und RNA *in situ* Hybridisierung.

[4] Gleichzeitig mit [1-3] wurden verschiedene auf asphärischen Linsen basierende Lichtblattgeneratoren von Dr. Saiedeh Saghafi und verschieden Bildbearbeitungsprogramme von Dr. Klaus Becker entwickelt und an den zuvor genannten geklärten Proben, in ihrer Fähigkeit die Bildqualität zu erhöhen, getestet.

Ergebnisse: [1] Mehrere Verbesserungen wurden beim Klären von transgenen Mäusegehirnen erzielt: (i) Die schon bestehende CLARITY Methode wurde verbessert indem die elektrophoretischen Gewebeklärkammer optimiert wurde, dies führte zu einer verkürzten Inkubationszeit und einer uniformen Delipidierung. Zusätzlich, wurde ein neues, kostengünstiges RI angleichendes Medium entwickelt welche eine niedrige Viskosität, eine langanhaltende Gewebetransparenz und Fluoreszenzstabilität bewirkt. (ii) Das 3DISCO Protokoll wurde in Bezug auf die Stabilität des Langzeit-Fluoreszenzerhaltes verbessert, welches im sDISCO Protokoll resultierte.

[2] Die CUBIC Methode wurde adaptiert indem ein Aminoalkohol mit stärkeren Depigmentierungseigenschaften hinzugefügt wurde. Dies führte zu dem ersten Klärungsprotokoll (FlyClear) welches das transgene Fluoreszenzsignal von *D. melanogaster,* während verschiedenen Entwicklungsstadien (drittes instar Larvenstadium, Pre-puppe, Puppe und adulte Fliege) erhält.

[3] Das Weiterentwickeln der FlyClear Methode resultierte in einen sehr vielseitigen Depigmentierungs- und Klärungsprotokoll (DEEP-Clear) für fünf, bis dahin noch nicht geklärte, wichtige Modellorganismen (Zebrafisch, Axolotl, Borstenwurm, Hawaiianischer Bobtail-Tintenfisch und der Langflossen-Küstenkalmar). Die Methode führte zu einer sehr guten Bewahrung der Morphologie der Proben und zu einer hohen Transparenz von heterogenem Gewebe. Zudem ist DEEP-Clear kompatibel mit wichtigen Markierungsmethoden wie fluoreszenten Reportersignalen, Immunhistochemie (für ganze Tiere bis zu 2.5 cm Länge), RNA *in situ* Hybridisierung und 5-Ethynyl-2'-deoxyuridine (EdU) Markierung.

[4] Die, für das FlyClear verwendeten Proben wurden mit dem von Dr. Saiedeh Saghafi entwickelten asphärischen Lichtblattgenerator mit eine Powellinse aufgenommen welcher mit einer Lochblende ausgestatte war. Manche Probenaufnahmen wurden mit einem von Dr. Klaus Becker geschriebenen „multiview combining" Algorithmus bearbeitet was zu einer isotropen Auflösung der 3D Bilder führte. Die, für das DEEP-Clear verwendeten Proben wurden mit einen asphärischen Lichtblattgenerator mit zwei Powellinsen aufgenommen und die Bilder wurden mit einem, von Dr. Klaus Becker, entwickelten Deconvolution Programes, welches eine theoretische Punktstreufunktion eines Lichtbandmikroskopes verwendet, bearbeitet. Dies führte zu isotropen Bildern von Proben, die bis zu 2.5 cm lang waren.

Schlussfolgerung: Mit der Verbesserung und Entwicklung verschiedener Klärungsmethoden, Lichtblattgeneratoren und bildbearbeitenden Computerprogramme für das Lichtblattmikroskope, konnte ein wichtiger Beitrag zur Erforschung von unterschiedlichen Modelorganismen und dabei zur Beantwortung verschiedenster biologische Fragestellungen geleistet werden wie z.B. die Beschreibung des verlustes der Kommisure-neurone in *D. melanogaster* Mutanten des Ahesionsmolekühls Neuroglian oder die Wachstumsdynamik im P. dumerili Auge in der Sepie oder in Axolotl. Das demonstrierte Spektrum an technischen Kompatibilitäten bietet neue und einzigartige Möglichkeiten, den Aufbau und Umbau innerer Gewebe in einem intakten Organismus bei Einzelzellauflösung umfassend zu analysieren.

Abstract

Introduction: The aim of this work was to develop and improve clearing methods that yield high sample transparency while preserving tissue morphology and, at the same time being compatible with various molecular labelling techniques e.g. transgenic fluorescent signal, immunohistochemistry and RNA *in situ* hybridisation. These clearing methods should facilitate the 3D system interrogation (from single organs to entire animals) of multiple model organisms, namely: mouse (*mus musculus*), zebrafish (*danio rerio*), fruit fly (*Drosophila melanogaster*), axolotl (*Axolotl mexicanum*), bristle worm (*Platynereis dumerilii*), Hawaiian bobtail squid (*Euprymna scolopes*) and longfin inshore squid (*Doryteuthis pealeii*).

Methodology: [1] The water-based CLARITY and CUBIC, as well as the dehydration based 3DISCO and uDISCO clearing methods were tested on adult transgenic Thy1-GFP-M and Thy1-YFP-H mice and evaluated according to the following criteria: (i) difficulty of implementation, (ii) toxicity, (iii) clearing properties, (iv) duration, (v) morphology preservation, (vi) refractive index (RI) matching media properties, (vii) fluorescent signal preservation and long term stability and (viii) overall cost. Finally, new chemicals were tested to improve the aforementioned properties.

[2] The water-based ScaleS and CUBIC, and the dehydration based 3DISCO clearing method were tested on different transgenic *Drosophila melanogaster* (fruit flies) and evaluated according to the following criteria (i) clearing properties, (ii) morphology preservation, (iii) RI matching media properties, (iv) depigmentation properties and (v) fluorescent signal preservation and long term stability. Finally, new chemicals were tested to improve the aforementioned properties.

[3] The water-based FlyClear protocol was tested on wild type and in some cases transgenic mouse, axolotl, zebrafish, bristl worm, Hawaiian bobtail squid and longfin inshore squid for its (i) clearing properties, (ii) morphology preservation, (iii) RI matching media properties, (iv) depigmentation properties and (v) fluorescent signal preservation and long term stability in cases of transgenic animals, as well as (vi) compatibility with molecular labelling methods (e.g. immunohistochemistry and RNA *in situ* hybridisation)

[4] Alongside [1-3], different aspherical lens-based light-sheet generators, developed by Dr. Saiedeh Saghafi, and image post-processing computer programs, developed by Dr. Klaus Becker, were tested on the aforementioned cleared specimens for their ability to improve image quality.

Results: [1] Several improvements were made in transgenic mouse brain clearing: (i) The existing CLARITY method was improved, including the optimisation of the electrophoretic tissue clearing chamber (ETC), leading to shortened incubation times and uniform tissue delipidation. Further, a new cost-effective RI matching medium which has low viscosity, results in excellent and lasting tissue transparency, and provides long term fluorescence stability was developed. (ii) The 3DISCO protocol was improved in respect of long-term fluorescent signal stability resulting in the new sDISCO protocol.

[2] The CUBIC method was adapted by adding an aminoalcohol with strong depigmentation properties resulting in the first protocol (FlyClear) which preserves transgenic fluorescent signals in *D. melanogaster* at different developmental stages (3rd instar larvae, prepupa, pupa and adult fly).

[3] The adaptation of the FlyClear method resulted in a highly versatile depigmentation and clearing protocol (DEEP-Clear) for five, so far never cleared, important model organisms (zebrafish, axolotl, Hawaiian bobtail squid, longfin inshore squid and bristle worm). This method showed excellent preservation of sample morphology and a high level of heterogeneous tissue transparency. Further, DEEP-Clear is compatible with key active labelling methods, namely transgenic fluorescent reporter signals, immunohistochemistry (whole-mount in animals up to 2.5 cm length), RNA *in situ* hybridization and 5-Ethynyl-2'-deoxyuridine (EdU) labelling.

[4] The samples used for the FlyClear protocol were imaged using an optical unit containing various meso-aspheric optical elements (e.g. one Powell lens and two acylinder lenses) equipped with a soft aperture to generate a thin light-sheet, designed by Dr. Saiedeh Saghafi. In addition, some of the samples were processed with a multiview combining algorithm, developed by Dr. Klaus Becker, resulting in isotropic 3D images. The samples used for the DEEP-Clear were imaged with an upgraded light-sheet system. The images were further processed with a deconvolution program, developed by Dr. Klaus Becker, using a theoretical point spread function resulting in isotropic images of samples up to 2.5 cm in length.

Conclusion: Different clearing methods, imaging tools and computational programs for the light-sheet microscope were improved and developed, that contribute to the research of diverse animal models, and thereby also to the exploration of different biological questions e.g. the loss of commissural projections for the adhesion molecule Neuroglian in *D. melanogaster* mutants or the growth dynamics in bristle worm eyes, axolotl and squid. The demonstrated spectrum of technical compatibilities provides novel and unique opportunities

to comprehensively analyse the assembly and remodelling of internal tissues in an intact organism at a single-cell resolution.

Contents

Outline of the Thesis

This Ph.D. thesis deals with the development and improvement of hydration and dehydration based clearing techniques. These techniques were used by Dr. Saiedeh Saghafi and Dr. Klaus Becker to test and develop imaging and computational tools. The methods outlined in the abstract resulted in seven peer-reviewed publications.

This thesis is structured as a cumulative work. It consists of an introductory chapter, the seven peer-reviewed publications (chapter 2-8) and a concluding chapter. Below, I will provide a short summary of each chapter of my dissertation:

Chapter 1 – Introduction

In the introduction, the challenges of imaging thick tissues are discussed, as well as possible approaches to overcome these challenges. Thereafter, the basic concepts of light, light propagation through thick tissue, absorption, and light scattering are introduced. Tissue clearing is presented as a solution for the problem of light scattering, and different tissue clearing approaches are discussed. Additionally, current imaging techniques are addressed and put in the context of thick tissue imaging. Different light-sheets and light-sheet formation are discussed. Finally, the image processing of light-sheet data is presented.

Chapter 2 – Ultramicroscopy: development and outlook

Outlook for the clearing field and light-sheet microscopy from the perspective of the year 2015. The development of ultramicroscopy, the visualisation of different tissues – mouse neuronal tissue, mouse embryos and fruit flies – and the development of adapted optics is discussed.

Chapter 3 – Outlook on optimizing ultramicroscopy imaging technique through optical characterization

Outlook for the clearing field and light-sheet microscopy from the perspective of the year 2016. The main focus is on the description of the new light sheet generators for the ultramicroscope. The new system, in contrast to conventional systems which use a slit aperture and a single cylindrical lens for generating a light-sheet, is very light efficient and minimizes typical unwanted patterns that occur due to diffraction phenomena. The presented recordings of cleared samples display an improved level of detail and resolution in comparison to previously reported images.

Chapter 4 – **Reshaping a multimode laser beam into a constructed Gaussian beam for generating a thin light sheet**

This chapter shows the reshaping of a multi-mode laser into a single-mode laser with a quasi-Gaussian distribution and the application of such a modulated laser beam to form a light-sheet. This newly developed approach showed that a multimode laser can generate a similar light-sheet as a single-mode laser. Different samples were imaged using such a light-sheet, resulting in image quality comparable to the one generated by the ultramicroscope system utilizing a single-mode laser.

Chapter 5 – **High-resolution ultramicroscopy of the developing and adult nervous system in optically cleared *Drosophila melanogaster***

Comprises my first publication as first-author and describes the development of the *FlyClear* method. This method is the first tissue clearing technique that was able to preserve the transgenic fluorescent signal in the fruit fly *D. melanogaster* at different developmental stages – 3rd instar larvae, pre-pupa, pupa and adult fly. Further, the method shows depigmentation properties in fruit fly eyes. Additionally, an improved light-sheet generator and a multi-view combining approach were presented.

Chapter 6 – **High-resolution imaging of fluorescent whole mouse brains using stabilised organic media (sDISCO)**

Presents the development of the sDISCO method, applied in Thy1 GFP-M and Thy1 YFP-H adult mouse brain. This paper demonstrates improved fluorescent signal preservation.

Chapter 7 – **Deconvolution of light sheet microscopy recordings**

Describes the deconvolution software developed by Dr. Klaus Becker and its application in improving the quality of images obtained using different types of light-sheets.

Chapter 8 – **A versatile depigmentation, clearing, and labelling method for exploring nervous system diversity**

Contains my second, first-authorship research article, which shows the development of the DEEP-Clear method. In this study, a clearing and depigmentation technique was developed for five model organisms - zebrafish, axolotl, Hawaiian bobtail squid, longfin inshore squid and bristle worm. Additionally, compatibility with key labelling methods was shown, namely fluorescent reporter signals, immunohistochemistry (whole-mount in animals up to 2.5cm length), RNA *in situ* hybridisation and EdU labelling. Using this approach, unprecedented system-wide- (light-sheet microscopy) and focal- analysis (confocal and two-photon microscopy) of different animal nervous systems, even in naturally pigmented species was achieved.

Chapter 9 – **Conclusion and outlook**

Selected features of clearing techniques are discussed and outlook on future research is given.

Chapter 1 - Introduction

1. Motivation

For centuries the analysis of biological samples relied on 2-dimensional (2D) information obtained from thin histological sections. However, the translation of these 2D data into a comprehensible, 3-dimensional (3D) reconstruction, is a fundamental challenge. In recent years there has been a shift in the field of life science to inquire about biological information in the context of the natural tissue environment thanks to the development of new analysis tools.

The development of optical sectioning microscopes such as light-sheet microscopes, as well as objectives with long working distances, high numerical apertures (NA) and adjustable refractive index (RI), provided a method to visualize large volumes of transparent living and non-living systems. In comparison to already established approaches like laser confocal scanning microscopy and two-photon microscopy (2Pi), these new imaging techniques offer a fast and precise alternative with a very low photo-toxicity, thereby reducing bleaching and tissue damage. However, if the samples are not transparent light is absorbed or scattered and sharp images from deep tissues (200µm - 500µm) are difficult to obtain. Improving image quality was partially addressed by harnessing computational algorithms such as multi-view combining approaches used for live early stage zebrafish larvae or fruit fly embryos, or by deconvolution approaches using a measured or theoretical point spread function (PSF). Nevertheless, image quality could only be improved up to the depth of 500µm.

In recent years, the rapidly evolving field of tissue clearing addressed the challenge of scattered light, resulting in highly sophisticated approaches that achieve tissue transparency through various chemical treatment strategies. The underlying goal of these techniques is to reduce the refractive index (RI) mismatch between different cellular compartments, facilitating a distortion-free propagation of light within the sample. However, these techniques were almost exclusively developed for a single organ, in most cases the rodent brain, thereby limiting their application. Further, many of these approaches suffer from tissue deformation, display varying degrees of sample transparency and/or are limited to one molecular labelling approach such as transgenic fluorescence reporter animal lines.

The aim of this work was to develop and improve clearing tools, which enable the examination of different model organisms regardless of their size and natural tissue opacity.

2. Theory and Basis

2.1 Challenges and approaches to image 3D volumes from tissue

For decades thin histological sections have been the gold standard for obtaining information about cellular composition and interactions in biological tissue. Indisputably, this approach deepened our insight into the processes of life and enabled major discoveries. However, the 2D nature of these slices (2-5µm thick) causes obvious limitations when describing 3D structures such as cells, organs or entire multicellular organisms and long-range connections. A complete understanding of biological mechanisms requires whole and unbiased investigation of entire systems, not just selected parts of the tissue. One important example, where the true nature cannot be ascertained by a thin section, is the nervous system, where individual neurons project in many directions and sometimes even span over different body compartments. When investigated locally, important biological information that is located elsewhere may be missed. Thus, the growing need to inquire about the 3D environment and cellular information led to the development of various methods.

One of the first attempts to gather volumetric information was by registering a series of thin sections, leading to the establishment of databases such as the PAXINOS or the Allen Brain Atlas. However, this approach is very challenging, laborious and in need of sufficient serial control sectioning due to distortion artefacts (compressing, folding, stretching and rupturing of sample tissue) which are introduced in the process of section generation (*1-3*). Other possibilities are the so-called "knife-edge" or "blockface" methods where the surface of a tissue block is imaged and sequentially shaved off (*4-8*). While these approaches reduce the loss and alignment issues of sections, they are also destructive in the sense that after a section is imaged it is cut away with a knife to reveal the next block surface, thus making reimaging impossible.

These limitations led to the development of optical sectioning techniques such as laser confocal scanning, spinning disk and 2Pi microscopy in which out of focus light is blocked out by a spatial pinhole. This enabled multidimensional imaging of volumes at different depths without physical sectioning, thereby avoiding the demanding alignment issues and providing the possibility for repetitive imaging (*9-11*). Such an optical sectioned stack can further be

reconstructed and in this way all 3D features of a biological sample can be ascertained. In combination with fluorescent tissue labelling methods such as DNA intercalating dyes, immunohistochemistry (IHC), fluorescent *in situ* hybridisation (FISH) and/or by using animals with a transgenic reporter signal, these imaging methods became an indispensable tool for 3D inquiry of live and fixed samples (*12, 13*). Although these laser scanning methods became a standard in the last decades, their applications, when facing thick tissue, remain limited for a couple of reasons:

- Biological tissue is usually not transparent, due to light scattering by the inhomogeneous parts (discussed below 3.2) or absorption through a variety of pigments such as haemoglobin, ommochrome, melanin, pterin or myoglobin. Scattering and absorption effects increase with imaging depth and undermine the sharpness of images and limit the excitation of a fluorophore and/or the emission returning to the detector.

- Biological tissue differs in its capability of autofluorescence induction, which is mainly responsible for the signal to noise ratio (SNR) – the level and specificity of the desired signal to the level of background noise. The SNR can be expressed using the following equation (Eq):

$$SNR = \frac{\mu_{sig}}{\sigma_{sig}} \qquad\qquad (Eq.1)$$

where μ_{sig} is the average signal value and σ_{sig} is the standard deviation.

Autofluorescence can originate from the tissue preparation process, as the interaction of glutaraldehyde or formalin with aldehydes leads to the formation of Schiff bases (*14*). Another source for autofluorescence can be the endogenous molecules in the tissue such as Nicotinamide adenine dinucleotide phosphate (NADPH), tyrosine, elastin, collagen or flavines.

- The above-mentioned tissue properties made light imaging possible to a certain depth, up to 200µm for confocal and up to 1mm for 2Pi (*15, 16*). Therefore, the development of microscopes and high numerical aperture (NA, the ability of an objective to collect light - a key determinant for resolution) objectives was focused on these working distances (WD, the distance between the front lens and the focus point in the sample). An in-depth discussion about objectives is provided later (section 3.4.1).

Despite these constraints, global phenotyping, although laborious, is in principle possible when these techniques are combined with histological sections of fixed tissue (*17-19*).

For some of the aforementioned problems, there are existing workarounds. Autofluorescence can be addressed by using sodium borohydrat to remove the Schiff bases (*20*) or by bleaching through high-intensity light (*21*). Blood, containing haemoglobin, from vertebrates can be removed by perfusion with phosphate-buffered saline (PBS) through the vascular system or decoloured with amino alcohols in a basic solution (*22-26*). Another possibility is bleaching the light-absorbing pigments with peroxide (*25, 26*) although this might have tissue-damaging effects and can cause fluorescence quenching (*27, 28*). Further, it is possible to prevent the formation of pigments during development through different experimental strategies which either rely on the induction of mutations in distinct pigment pathways, as exemplified by the fruit fly white mutant (*29*), or the golden or microphthalmia-associated transcription factor (mitfa) mutants in zebrafish (*30-32*). In turn, individual pigmentation mutants may cause unintended side effects (*33*), and typically do not achieve full transparency on their own. Further, the genetic engineering of completely unpigmented strains requires mutations in several independent pathways, involving significant genetic work and thus limiting the applicability of this approach except for a few very well established model species (*34*). Alternatively, inhibitors are employed that impact on the biogenesis of specific pigments, such as the widely used drug 1-phenyl-2-thiourea (PTU) that interferes with the tyrosinase enzyme involved in oxidizing 3,4-dihydroxyphenylalanine (L-DOPA) or dopamine (DA) to the respective melanin precursors L-DOPA quinone and DA quinone (*35-38*). Both approaches, however, have significant limitations: biochemical interference with tyrosinase during development is often incomplete and causes side effects, as demonstrated for catecholaminergic neurons (*39*) or for thyroid hormone signalling and eye development in fish. Finally, near-infrared fluorophores can be used, since wavelengths of 650-1350nm are weakly absorbed or scattered by tissue (*40*).

However, none of these techniques address the primary problem of deep tissue imaging, namely the low penetration of light caused by the inhomogeneities in the biological specimens and the consequent light scattering.

Different methods exist for imaging of large 3D volumes using wavelengths which can pass through intact tissue and have no need for WD-limited objectives. These include magnetic resonance imaging (MRI) (*41*) and computed tomography (CT) (*42*) which can achieve single-neuron resolution in mouse (*43*). Such systems are very potent when it comes to large scale analysis of system architecture and volumetric data in humans and various model and non-model organisms. The tracing of cells and the extraction of single cell properties in highly

heterogeneous populations, however, is still difficult due to the lack of whole-system high-contrast cell-labelling tools (*44, 45*).

Nevertheless, some proof of principle solutions were shown to address this shortage in specific tissue labelling, although they were initially invented for electron microscopy. By using x-ray detectable protein tags electron dense contrast could be generated as demonstrated in mouse (*46*) and the fruit fly (*47*).

Such strategies include genetic solutions where cells express probes containing photosensitiser proteins such as the mini singlet oxygen generator (miniSOG) (*48*), enzyme peroxidases such as horseradish peroxidase (HRP) (*49-51*), photosensitive dyes that associate with proteins (*52*) or short peptides such as ReASH (*53*). However, such labelling has a couple of limitations, which currently make whole system approaches or even thick tissue (>200µm) labelling very difficult. First, such labelling approaches either have limited targeting capabilities (e.g. HRP) (*49-51*), show the necessity of cell-toxic conditions for probe introduction (e.g. ReASH) (*53*), or lead to neurotoxicity over time (e.g. miniSOG) (*47*). Second, in the case of miniSOG, the reaction producing the contrast material for x-ray imaging is induced by fluorescent light which needs to transmit through the sample. If the genetically marked target area is in opaque deep tissue it is very difficult, due to light scattering, to start the labelling reaction. However, dissected brain sections could be labelled up to 100µm in this way (*47*). Third, since the light induced generation of the contrast materials has to be stopped at a certain point and various parameters such as probe expression level, localised targeting, labelling density, fixation conditions, diaminobenzidine (DAB) photo-oxidation and microscope settings play a role for the optimal reaction duration, it is very difficult to find the delicate balance between under- and overlabelling of the sample (*47*).

High-speed 3D reconstructions with subcellular resolution of Golgi stained undissected *D. melanogaster* brains (*54*) and whole mouse brains (*55*) could be achieved when combined with x-ray tomography. Nevertheless, there are certain limitations to this approach, since the heavy metal ions are taken up inside the cell body of the neurons in a random fashion and the reason why is not completely understood yet (*54*). Further, this approach comes with tissue distortion e.g. when looking at the thorax and abdomen of the flies (*54*). Finally, a synchrotron facility is very cost-intensive and not accessible to the broad majority of scientists.

An elegant solution to address the absorbing and light scattering properties of biological samples is provided by tissue clearing, where samples are chemically rendered transparent. The principle of these optical clearing methods is to create a more or less homogenous environment, with an average RI, facilitating the transmission of light. This is achieved by

replacing components such as the water-based cellular fluid, with a solution of high RI to match that of the cell, nuclear, and organelle membranes and in some cases by additionally removing strong scattering molecules such as lipids. This way tissue clearing can contribute to the imaging depth and contrast (*56, 57*). In combination with imaging methods such as optical projection tomography (OPT) (*58*) or light-sheet microscopy (*59*) they provide a powerful tool for 3D visualization. Clearing methods are the main focus of this dissertation and will be discussed in the following sections. In addition, a brief introduction to light-sheet microscopy, microscope objectives and deconvolution will be provided and put in context with the published data.

3.2 Physics behind transparent tissue

In most cases biological tissue does not appear transparent. This is due to absorption and different scattering effects of light. To understand these effects, light and its interaction with biological materials have to be discussed and characterised.

In physics, environmental variables are controlled where possible. The preferable experiments are conducted in "clean" and simple systems with one adjustable, isolated variable where the effect of changes on the rest of the system is monitored. In contrast, biological systems are usually composed of many molecules, thus have many degrees of freedom, leading to many variables that have to be considered. Therefore, the literature, from the perspective of physics, refers to biological samples as "wet, noisy and warm systems".

The following physical concepts are explained for ideal homogenous systems, which is at first counterintuitive when thinking about an application on biological samples. However, transparency per its definition can only occur, if an object has a uniform refractive index (RI) and is not strongly absorbing or diffracting light. Therefore, the chemical transformation from an opaque or translucent biological sample into a transparent one can be treated, with respect to light-matter interaction, as a transformation from a "noisy" to a "clean" system. Henceforth, the following equations and explanations provide a sufficient approximation when describing transparent tissue.

(*Note: Equations 3-33 are from the book "Photonics: An Introduction" by Georg A. Reider.*)

The physical rules applied by aforementioned visualisation methods such as MRI and electron microscopy, where magnetic fields or electrons are used for image generation are independent of tissue transparency and are not discussed. The following section is focused

on the spectral window of the so-called visible, coloured, or white light originating from electromagnetic (EM) radiation of wavelengths (λ) around 380-740nm with their corresponding frequencies (f) of about 4×10^{14}- 8×10^{14} Hz as shown **Fig.1.** The relationship between the wavelength (λ), velocity (v), and frequency (f) of light can be defined using Eq.2.

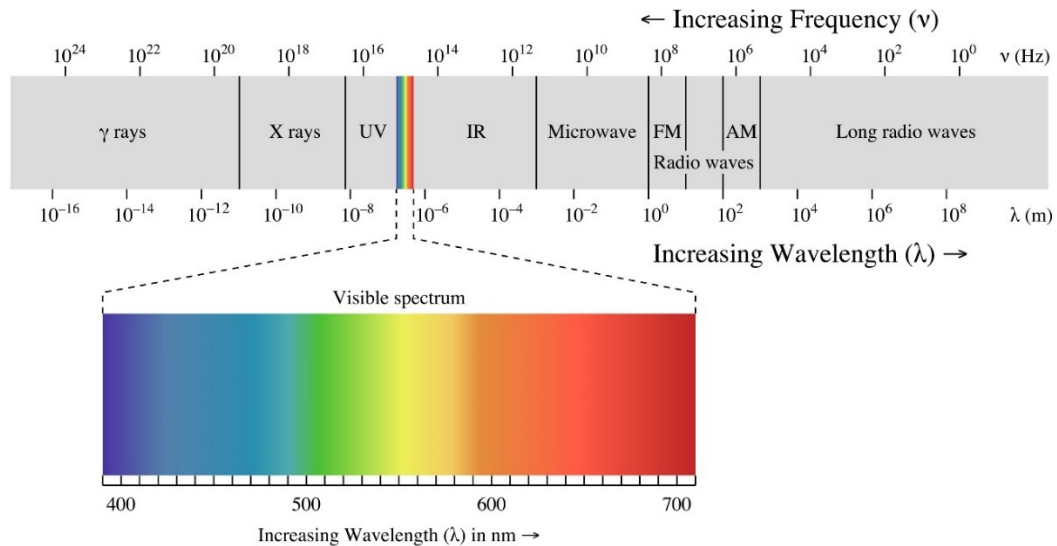$$\lambda = \frac{v}{f} \qquad \qquad \text{(Eq.2)}$$

Figure 1: Electromagnetic spectrum, with the visible portion highlighted.

Image source: https://en.wikipedia.org/wiki/Light#/media/File:EM_spectrum.svg

In this spectral range very few physical constants such as the mass ($m_e = 9.109 \times 10^{-31} kg$), charge of an electron ($e = 1.602 \times 10^{-19} C$), or the Planck's constant ($h = 6.626 \times 10^{-34} Js$) are responsible for the optical properties of matter. Outside this window, which is bordered by ultraviolet (UV) and infrared (IR) light, the matter is either strongly absorbing or does not interact with EM radiation (*60*).

3.2.1 Visible light

There are multiple attempts to describe light characteristics ranging from ray-optics, which is the easiest to understand, to photons and quantum-optics, which is probably the closest description to the true essence of light, and to light waves-optics, which is in our case the most helpful approach when trying to comprehend light scattering. Accordingly, these waves with a

particular wavelength, have a magnetic component and an electrical component (**Fig.2**) emitting an electromagnetic field.
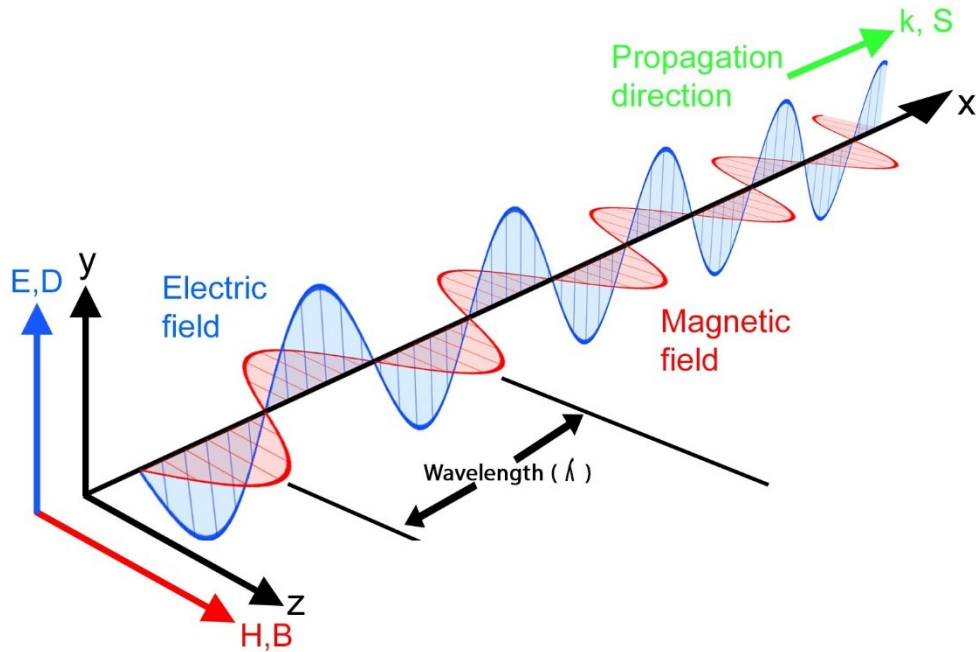

Figure 2: Scheme of an electromagnetic wave described as a self-propagating transverse oscillating wave of electric and magnetic fields. Modified, image source: https://commons.wikimedia.org/wiki/File:Electromagnetic_waves.png

The electric field $\mathbf{E}[Vm^{-1}]$ and the magnetic field $\mathbf{H}[Am^{-1}]$ in a medium with polarisation density $\mathbf{P}[Asm^{-3}]$, magnetisation density $\mathbf{M}[Am^{-1}]$, density of free charges $\rho[Vm^{-1}]$ and current density $\mathbf{j}[Am^{-2}]$ can be related by using Maxwell's equations (*60*);

$$\nabla \times \mathbf{E} = -\mu_0 \frac{\partial \mathbf{H}}{\partial t} - \mu_0 \frac{\partial \mathbf{M}}{\partial t} \tag{Eq.3}$$

$$\nabla \times \mathbf{H} = \varepsilon_0 \frac{\partial \mathbf{E}}{\partial t} + \frac{\partial \mathbf{P}}{\partial t} + \mathbf{j} \tag{Eq.4}$$

$$\nabla \cdot (\varepsilon_0 \mathbf{E}) = -\nabla \cdot \mathbf{P} + \rho \tag{Eq.5}$$

$$\nabla \cdot (\varepsilon_0 \mathbf{H}) = -\nabla \cdot (\mu_0 \mathbf{M}) \tag{Eq.6}$$

where $\mu_0 = 4\pi 10^{-7} VsA^{-1}m^{-1}$, $\varepsilon_0 = 8.854 \times 10^{-12} AsV^{-1}m^{-1}$ and t are vacuum permeability and time, respectively. In cartesian coordinates, the differential operator ∇ is given by;

$$\nabla = \begin{bmatrix} \partial/\partial x \\ \partial/\partial y \\ \partial/\partial z \end{bmatrix} \tag{Eq.7}$$

when **P** is the response of the medium to the electric field, **E** and they are related through the following equation;

$$\mathbf{P} = \varepsilon_0 \boldsymbol{\chi} \mathbf{E} \qquad \text{(Eq.8)}$$

where χ is the electric susceptibility and represents the dielectric properties of a medium in the presence of an electric field.

If the displacement density of the vacuum $\varepsilon_0 \mathbf{E}$ is combined with the polarization density **P** the electrical displacement density $\mathbf{D}\left[Asm^{-2}\right]$ can be obtained describing the time-varying of an electric field;

$$\mathbf{D} = \varepsilon_0 \mathbf{E} + \mathbf{P} \quad . \qquad \text{(Eq.9)}$$

To simplify the first two Maxwell's equations Eq.3 and Eq.4, we assume that the magnetic component **M** is negligible at optical frequencies, since the electronic component mainly interacts with the atoms in biological tissue. In the absence of a current and free charges ($\mathbf{j} = 0$, $\rho = 0$) this allows to describing the electric and magnetic field as following

$$\nabla \times \mathbf{E} = -\mu_0 \frac{\partial \mathbf{H}}{\partial t}, \qquad \text{(Eq.10)}$$

$$\nabla \times \mathbf{H} = \frac{\partial \mathbf{D}}{\partial t}, \qquad \text{(Eq.11)}$$

with

$$c_0 := \frac{1}{\sqrt{\varepsilon_0 \mu_0}}, \qquad \text{(Eq.12)}$$

Equations 10 and 11 can be further used to derive the general wave equation for the electric field in isotropic, linear and local media through;

$$\nabla^2 \mathbf{E}(\mathbf{x}, t) - \frac{\varepsilon}{c_0^2} \frac{\partial^2 \mathbf{E}(\mathbf{x}, t)}{\partial t^2} = 0 \qquad \text{(Eq.13)}$$

where ε is the electric polarizability of a dielectric called permittivity, $c_0 = 2.998x108 \ ms^{-1}$ and is called the vacuum speed of light.

By using the time-harmonic of Maxwell's equation the complete plane wave solution can be derived from (Eq.13)

$$\tilde{\mathbf{E}}(\mathbf{x}, t) = \tilde{\mathbf{E}}(\mathbf{k}, \omega) e^{-\mathrm{j}(\mathbf{k} \cdot \mathbf{x} - \omega t)} \qquad \text{(Eq.14)}$$

where **k** is a known wave vector giving the direction of field propagation and ω is the angular frequency. In this equation $\tilde{\mathbf{E}}(\mathbf{x}, t)$ is the complex wave function, $\tilde{\mathbf{E}}(\mathbf{k}, \omega)$ is the complex amplitude and $e^{-\mathrm{j}(\mathbf{k}\mathbf{x} - \omega t)}$ is the imaginary part of the equation representing the phase.

These waves (Eq.14) can be imagined as planes with surfaces of constant phase, $\mathbf{k} \cdot \mathbf{x} - \omega t = constant$, which are normal to the wave vector $\mathbf{k}$, propagating in a particular direction without converging or diverging (plane waves). The equidistant planes with the same phase are separated by the wavelength which can be expressed as follows

$$\lambda := \frac{2\pi}{|\mathbf{k}|} \qquad (Eq.15)$$

3.2.2 Propagation of EM waves

Inserting Eq.14 in the Helmholz equation leads toward:

$$\nabla^2 \bar{\mathbf{E}} + \omega^2 \mu_0 \varepsilon_0 \bar{\mathbf{E}} = 0 \qquad (Eq.16)$$

The fundamental dispersion relationship between the angular frequency ω, the wavenumber k and the wave velocity v can be established through:

$$k = \frac{\omega}{c_0} n \qquad (Eq.17)$$

where n is refractive index (RI) factor or propagation index factor, which is a dimensionless number describing how fast light travels through a medium in comparison to vacuum, c_0, and is given by:

$$n := \sqrt{\varepsilon} = \sqrt{1 + \chi} = \frac{c_0}{c} \qquad (Eq.18)$$

This slowdown of the light results from the tendency of atoms in a material to absorb energy and maintain the absorbed energy in the form of vibrating electrons before reemitting it as a new EM disturbance. The number of interactions, and therefore the slowdown of light per unit volume, is dependent on the density and the susceptibility of the molecules in the medium.

Each wavelength has a different RI and thus travels with different speed through a dispersing medium such as air or glass. Using Eq.17, an expression for the speed of each particular wavelength in a given transparent medium, the so called phase velocity v_{ph}, can be derived:

$$v_{ph} = \left| \frac{d\mathbf{x}}{dt} \right| = \frac{\omega}{k} = \frac{c_0}{n} \qquad (Eq.19)$$

In vacuum $n = \sqrt{\varepsilon} = 1$ and the resulting phase velocity is equal to the vacuum velocity of light, $v_{ph} = c_0$. The RI of transparent condensed media ranges between 1 and 3, meaning that the corresponding phase velocity ranges between c_0 and $\frac{c_0}{3}$. The importance of the RI for the

development of methods to artificially generate transparent biological tissue or in objective design will become apparent at later points in the introduction.

3.2.3 Energy transport and exchange of the EM field and matter

When a plane wave hits a biological tissue, its electrical energy is absorbed, reflected or transmitted by the atoms or molecules (depending on the wavelength) of the object. The energy transported by the wave can be described by Poynting's theorem (*60*).

$$\mathbf{E}(\nabla \times \mathbf{H}) = \mathbf{E} \cdot \frac{\partial}{\partial t}(\varepsilon_0 \boldsymbol{E} + \boldsymbol{P}) \tag{Eq.20}$$

For the interpretation of each term the divergence-theorem has to be used (*60*),

$$\int_V (\nabla \cdot \mathbf{u})\, \mathrm{d}V = \int_A \mathbf{u} \cdot \mathbf{n}\, \mathrm{d}A \tag{Eq.21}$$

where A is the surface of the volume V, $\mathbf{n}$ is the outward pointing unit normal vector of a surface element, and $\mathrm{d}V$ and $\mathrm{d}A$ are differential volume and surface elements respectively, to transform the differential form of Poynting's theorem into

$$\int_A [(\mathbf{E} \times \mathbf{H}) \cdot \mathbf{n}]\, \mathrm{d}A = -\int_V \left[\frac{\partial}{\partial t}\left(\varepsilon_0 \frac{\mathbf{E} \cdot \mathbf{E}}{2} + \mu_0 \frac{\mathbf{H} \cdot \mathbf{H}}{2} \right) + \mathbf{E} \cdot \frac{\partial \mathbf{P}}{\partial t} \right] \mathrm{d}V \tag{Eq.22}$$

The terms $\varepsilon_0 \mathbf{E} \cdot \mathbf{E}/2$ and $\mu_0 \mathbf{H} \cdot \mathbf{H}/2$ represent the electric and magnetic contribution to the vacuum-energy density of the field, while $\mathbf{E} \cdot (\partial \mathbf{P}/\partial t)$ is the power density that is exchanged between the field and the medium. Therefore, the right-hand side of (Eq.22) is equal to the temporal change of the stored energy in a volume V. Thus, the left-hand side is considered as the energy flux through the surface A, and $\mathbf{S}$ is the Poynting's vector representing directional energy flux of an EM field and is given by:

$$\mathbf{S} = \mathbf{E} \times \mathbf{H}. \tag{Eq.23}$$

In isotropic media, the intensity I of a plane wave can be expressed as

$$I = |\langle \mathbf{S} \rangle| = n\frac{\tilde{\mathbf{E}}(\omega) \cdot \tilde{\mathbf{E}}^*(\omega)}{2Z_0} = n\frac{\mathbf{E}_0^2}{2Z_0} \tag{Eq.24}$$

where $Z_0 \cong 377\varOmega$ is the vacuum impedance.

If the incident light is not normal to the surface then the intensity is given by

$$\mathbf{n} \cdot \langle \mathbf{S} \rangle = n\frac{\mathbf{E}_0^2}{2Z_0}\cos\theta \tag{Eq.25}$$

where θ is the angle of the incident light measured from the surface normal.

When discussing the energy exchange of field and matter the last term $\mathbf{E} \cdot \frac{\partial \mathbf{P}}{\partial t}$ of (Eq.22), representing the product of the electric field and the polarization current density, has to be considered, since the energy exchange in a polarized medium is not constant. Therefore, it is assumed that the susceptibility is complex, $\tilde{\chi} = \chi' + j\chi''$ and when taken into account in the polarization density $\widetilde{\mathbf{P}}(\omega) = \varepsilon_0 \tilde{\chi} \widetilde{\mathbf{E}}(\omega)$ the polarization current density is expressed as

$$\frac{\partial \widetilde{\mathbf{P}}(t)}{\partial t} = j\omega\varepsilon_0 \tilde{\chi} \widetilde{\mathbf{E}}(t) \qquad (\text{Eq.26})$$

Therefore, the power density that is transferred from the field to the medium can be expressed as following:

$$\langle \mathbf{E} \cdot \frac{\partial \mathbf{P}}{\partial t} \rangle = \frac{1}{2} \text{Re}[\widetilde{\mathbf{E}}(\omega) \cdot [j\omega\varepsilon_0 \tilde{\chi} \widetilde{\mathbf{E}}(\omega)]^*] = -\chi'' \frac{\omega\varepsilon_0 \widetilde{\mathbf{E}}(\omega) \cdot \widetilde{\mathbf{E}}^*(\omega)}{2} \qquad (\text{Eq.27})$$

3.2.4 EM wave propagation between the interface of two media

The incident light is usually coming from a single direction and the outgoing light is sent as a spherical wave in all directions. However, a defined area on the surface of such a spherical wave appears at a certain distance as a very close approximation to a plane (*60*). Therefore, for further calculation, plane waves (Eq.14) can be used to illustrate the elementary modes of light propagation. The polarization of EM waves at boundaries will not be discussed, since this property does not have a crucial impact on tissue transparency. For further simplicity, lossless and isotropic media with a planar boundary are assumed.

The incident (i) EM waves usually reflect (r) and transmit (t) between two dielectric media with RIs n_i and n_t. In the case of $n_t = n_i$ no change in the direction of the incident beam occurs. In the case of $n_t < n_i$ or $n_t > n_i$ the transmitted wave changes the propagation direction, which is known as refraction, if not normal to the boundary surface. The medium with lower RI is said to be optically thinner, the medium with the higher RI is said to be optically denser. Each wave vector can be separated into a component normal $k_{\perp}^{i,r,t}$ and component tangential $\mathbf{k}_{\parallel}^{i,r,t}$ to the interface (IF) of the media. At the IF, there is no contribution of the normal component to the wave function, therefore (Eq.14) can be written as following:

$$\mathbf{E}^{i,r,t}\big|_{\text{IF}} = \mathbf{E}_0^{i,r,t} e^{-j(\mathbf{k}_{\parallel}^{i,r,t} \cdot \mathbf{x} - \omega t)} \qquad (\text{Eq.28})$$

with the tangential components of the participating wave vectors being equal

$$\mathbf{k}_\|^i = \mathbf{k}_\|^t = \mathbf{k}_\|^r \tag{Eq.29}$$

The length of the respective vectors can be derived from the dispersion relation (Eq.17) with the condition $n_r = n_i$ resulting in

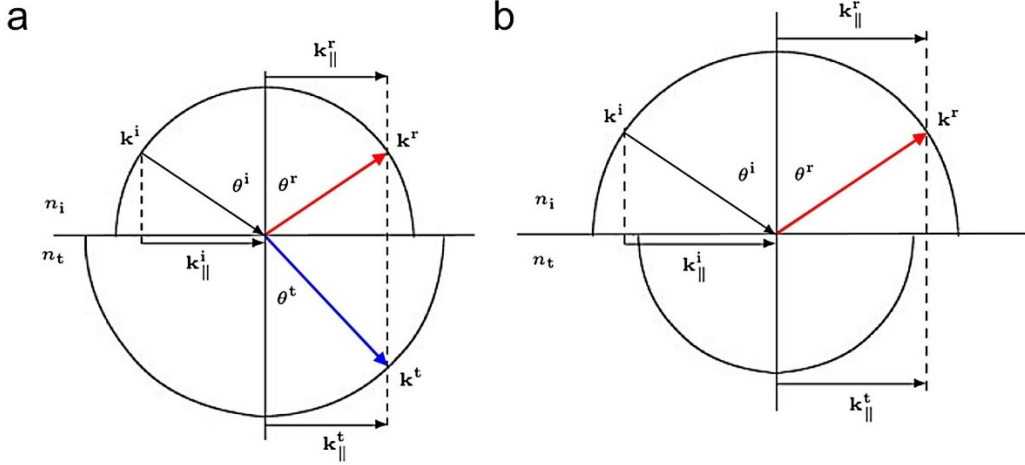$$\left|\mathbf{k}^{i,r,t}\right| = n_{i,r,t}k_0 \tag{Eq.30}$$

Figure 3: Wave vector propagation conditions at a planar invariant interface. (a) Incident beam $\mathbf{k}^i$ being partially reflection ($\mathbf{k}^r$, red) and transmission ($\mathbf{k}^t$, blue) with tangential conditions satisfying $\mathbf{k}_\|^i = \mathbf{k}_\|^t = \mathbf{k}_\|^r$, the length of the respective vectors is given by the dispersion relation $\left|\mathbf{k}^{i,r,t}\right| = n_{i,r,t}k_0$. **(b)** Incident beam $\mathbf{k}^i$ being totally reflected ($\mathbf{k}^r$, red) with conditions $\left|\mathbf{k}_\|^t\right| > \left|\mathbf{k}^t\right|$. Modified, image source: *Photonics: An Introduction* by Georg A. Reider

By introducing the angle $\theta^{i,r,t}$ between the surface normal and the respective wave vectors, we obtain following relation for the partial reflection of waves (**Fig.3a**),

$$\sin\theta^r = \sin\theta^i \tag{Eq.31}$$

with condition $\left|\mathbf{k}_\|^i\right| = n_i k_0 \sin\theta^i > n_t k_0$, total reflection of waves (**Fig.3b**)

$$\theta^i > \theta_{crit} = \arcsin\frac{n_t}{n_i} \tag{Eq.32}$$

where θ_{crit} is the critical angle for total reflection and according to Snell's law following relation for the transmission of waves (**Fig.3a**),

$$n_t \sin\theta^t = n_i \sin\theta^i \tag{Eq.33}$$

in which case a medium would appear transparent (**Fig.4 left picture**). As discussed above (3.2.2, phase velocity) each wavelength has a different propagation speed. The angles determined by Snell's law also depend on frequency or wavelength, so that a ray of mixed wavelengths will disperse. One of the most prominent examples showing the impact of this

effect is when a beam of white light is entering a glass prism at an angle resulting in a separation of the light rays into the visible spectral colours (rainbow colours).

If the boundary between two media has a variant shape, the argument $\mathbf{k}_{\parallel}^{i} = \mathbf{k}_{\parallel}^{t} = \mathbf{k}_{\parallel}^{r}$ is not valid. This results in diffraction, the diffused re-emission of light, and the object appears translucent (**Fig.4 middle and right picture**).

Figure 4: Impact of cleared tissue surface and thickness on light transmission All pictures are from the same cleared and RI-matched mouse brain. <u>Left:</u> Fully immersed in a liquid with matching RI having a uniform surface for incident light (transparent). <u>Middle:</u> Half immersed in a liquid with matching RI having some areas with a uniform surface (transparent) and some with a variant surface (translucent) for incident light. <u>Right:</u> Not immersed in RI matching liquid having a variant surface (translucent) with stronger light scattering in the thick middle of the brain.

3.2.5 Visible light propagation and interaction in biological tissue

In reality, it rarely happens that one single frequency of light hits an object. In the case of visible light many frequencies are incident upon the surface of objects. Under this condition, biological tissue, or any other matter, selectively absorbs, reflects or transmits light of certain frequencies depending on the nature of atoms in the object. To understand the mechanism behind these effects it is useful to think of electrons as attached to atoms by a spring. The electrons of each specific atom tend to vibrate more or less, depending on how close a specific frequency is to the natural frequency or frequencies of the atom (*14*). Light striking an object with atoms which have the same vibrational frequencies as the light wave, results in a vibrational motion with a large amplitude of the electrons of those atoms. These electrons interact thereby with neighbouring atoms in such a manner that the vibrational energy is entirely converted into thermal energy. This effect is called absorption (*14*). In contrast to absorption, reflection and transmission of light occur because the frequencies of light waves

do not match the natural frequencies of tissue, resulting in a short vibration of the electrons with small vibrational amplitudes. During reflection, the vibrational energy of atoms at the surface of an object is reemitted as a reflected wave, while during transmission the vibrational energy of the electron is passed on to neighbouring atoms through the entire material and is reemitted on the opposite side of the object (*14*). It is important to know, that in either case, the interaction with the electronic cloud (see also 3.2.2, RI and Eq.18) usually causes a delay of ½ λ of the new appearing wave.

The difference between the incoming light wave and the outgoing light wave emitted by the atom or molecule is that the incoming incident light derives from a single direction, while the outgoing light is sent as a spherical wave in all directions. This is known as light scattering (*14*). The whole process occurs without any energy loss of the electrons, as would be the case in ionization, and without a change in the wavelength, thus the light is said to be elastically scattered.

At this point, the wave concept of light is particularly useful, because it can explain how in-phase amplitudes of light can add up, causing brighter light (constructive interference). In the same way, it can describe how light can, depending on the amplitude of the waves, appear dimmer or be completely obliterated when a crest of one wave meets a trough of another wave (destructive interference). The concepts of interference and the reduced velocity of light in a medium (see also 3.2.2, RI and Eq.18 and Eq.19) can be used to understand why inhomogeneous media appear translucent or opaque and homogenous media, such as water or glass, appear clear even though the molecules in these substances scatter light.

While a spherical wave is propagating through a medium, it interacts with other molecules, re-emerging over and over and causing further spherical waves at different sites. In a transparent medium these molecules are homogeneously distributed, at a magnitude closer than the actual wave length (*61*); this means that each point of the lights propagation axis is simultaneously bombarded by waves in every phase. Thus, the resulting sum of amplitudes is zero and no light transmits perpendicular to the propagation plane. The reason why the wave-fronts are not cancelling each other out can be attributed, as discussed above, to constructive interference and the ½ λ retardation effect caused by the interactions of light with the electrons in the molecules. While the light is propagating, each molecule in front of the propagation plane is activated after the primary wave reaches them. The scattered light from these molecules reaches the subsequent molecules in the forward direction with an additional half-wavelength phase delay, thus the amplitudes sum up, causing a constructive interference and therefore light propagation.

In opaque cellular tissue, even if dense, the distances between the molecules vary and the individual components have different RIs e.g. membranes with an RI of 1.45 versus the cell lumen with an RI of about 1.33, resulting in complex boundary conditions. These inhomogeneities in the medium result in absorption or lateral scattering effects, such as reflection, and increase with the lights propagation depth. This relation of scattering and tissue thickness is the reason why a thin heterogeneous tissue transmits some amount of light and appears translucent while a thick tissue absorbs the light at a certain depth and appears opaque.

Absorption and scattering effects of frequencies in the spectral window, which the human eye can perceive as visible light, are responsible for the vision of colour. A yellow flower for example reflects most of the wavelengths with frequencies that a human experiences as yellow colour and absorbs the rest of the frequencies. However, it is important to note that the same flower may reflect waves with frequencies not visible to the human eye under normal conditions, but which are very visible to the visual systems of other animals (**Fig.5**).

Figure 5: Visual-system dependent color perception. The panel shows from left to right the same flower with human vision, only UV vision (bright = UV), simulated bee vision (UV+Green+Blue), simulated bird vision (tetrachromatic: UV+Red+Green+Blue). Image source: Dr. Klaus Schmitt, Weinheim, Germany, uvir.eu

Further, it has to be taken in account, that the definition of transparency, as the vision of colours, is closely related to the human visual system, since transparent objects like colored glass are non-transparent for animals which have a different visible spectrum e.g. lab mice and rats cannot see through red transparent objects.

3.2.6 Optical properties of biological tissue

Die approbierte gedruckte Originalversion dieser Dissertation ist an der TU Wien Bibliothek verfügbar.
The approved original version of this doctoral thesis is available in print at TU Wien Bibliothek.

TU Bibliothek
WIEN Your knowledge hub

Biological tissue can be categorised into two large groups. First, strongly scattering (opaque) tissue such as the brain, skin, blood, vascular walls and bones. Second, in weakly scattering (transparent) tissue such as the cornea and lens in the eye (*62-69*).

Models for light scattering can be separated, according to particle size, into three classes (**Fig.6**). These classes are based on a dimensionless parameter α

$$\alpha = \frac{\pi D_P}{\lambda} \qquad \text{(Eq. 34)}$$

where πD_P is the circumference of a particle.
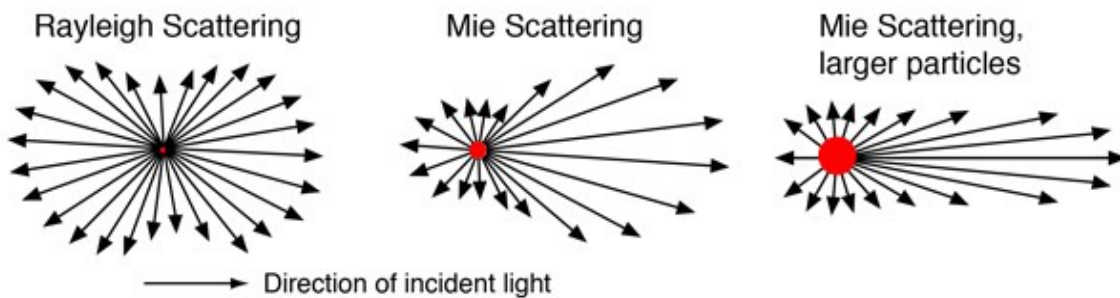
Figure 6: Scattering pattern related to particle size. Particle in red with arrows pointing in the direction of emitted light. Left: Small particles display a uniform pattern of emission. Middle and Right: Backscattering is reduced and forward scattering is increased with particle size.

$\alpha \ll 1$: Rayleigh scattering with the particle size of about 1/10 of λ (<50nm)

$\alpha \approx 1$: Mie scattering with particle size about the same as λ (50-500nm)

$\alpha \gg 1$: Large Particle Mie scattering or optical scattering with a particle size much bigger than λ (>1μm)

A general mathematical expression of opaque biological samples is rather difficult, since each tissue has a very complex individual surface. Such models are very complicated and require intensive computational time even for a rather small object like a small part of the surface of the human skin (*65, 66, 70*). A description of the scattering event would require multi scattering models for scalar wave propagation in randomly inhomogeneous absorption media, which would exceed the framework of this thesis.

However, laser beam intensity loses in opaque biological tissue can be described according to the exponential law (*63*)

$$I_{(l)} = (1 - R)I_0 e^{-\mu_t l} \qquad \text{(Eq.35)}$$

where R is the coefficient of Fresnel reflection at normal beam incidence, $R = [(n-1)/(n+1)]^2$, I_0 is the incident light intensity, $\mu_t = \mu_a + \mu_s$ is the extinction coefficient, μ_a

is the absorption coefficient, μ_s is the scattering coefficient, and l is the thickness of the sample.

According to this equation one can say that in general shorter wavelengths penetrate less deeply into opaque tissue. It has been shown that short-wave visible light penetration of non-transparent biological tissue is in the range of 0.5-2.5mm while long wavelengths of visible light (600nm<) penetrate depths of 8-10mm (*62, 63, 66, 70, 71*). Nevertheless, as discussed above, light penetration does not depend on the wavelength, but rather on the nature of the matter and whether the photon has the appropriate energy to excite a transition of a charged particle. As an example, water in a transparent glass transmits visible light (λ=400nm-700nm), whereas microwaves (λ=1mm-1m) penetrate glass very easily, but are strongly absorbed by water; ultraviolet light (λ=10nm-400nm) is stopped by glass but not so much by water, and infrared (λ=750nm-1mm) is strongly absorbed by both glass and water.

Mathematical models of samples with weak scattering properties, such as the cornea or lens of the human eye, can be used as a proof of principle to simulate scattering events occurring during light transmission in transparent tissue. Thereby it is assumed that the size of the scatterers are in the Rayleigh- to Mie-scattering range ($\alpha \ll 1$ to ≈ 1), see (**Fig.6**). Further, it is presumed that the particles are in very close proximity and that the RI is, although complex, almost homogeneous (*63*). Models for the eye are also dependent on the shapes occurring in the respective medium, such as long round dielectric cylinders for corneal collagenous fibres or spherical particles for lens protein structures. However, due to the generally small amount of scattering, it is possible to use a single model describing the scattering indicatrix for the symmetric scattering of particles with paired correlation by the following equation (*63, 69, 72-74*)

$$I(\theta) = I_0(\theta)\left\{1 + \rho_p \int_0^\infty [g(r) - 1]e^{j(\mathbf{S_1}-\mathbf{S_0})}\mathrm{d}^3r\right\} = I_0(\theta)F \qquad \text{(Eq.36)}$$

where $I_0(\theta)$ is the indicatrix of an isolated particle, ρ_p is the particle density, $g(r)$ is the distribution function of scattering centers (for non-scattering $g(r) \to 1$), $\mathbf{S_1}$ and $\mathbf{S_0}$ are unit vectors for the incident and scattered waves, r is the radius vector and d^3r is the volume of a scatterer, and F describes the interference effects.

The interface term F would be defined for long-cylinder systems such as the cornea by

$$F = 1 + \rho_{ms} \int_0^\infty J_0(\mathbf{S} \cdot \mathbf{r}) \cdot r[g(r) - 1]\mathrm{d}r \qquad \text{(Eq.37)}$$

and for systems with spherical particles such as the human lens by

$$F = 1 + 4\pi\rho_{ms} \int_0^\infty r^2[g(r) - 1]\left[\frac{\sin(\mathbf{S}\cdot\mathbf{r})}{(\mathbf{S}\cdot\mathbf{r})}\right]\mathrm{d}r \qquad \text{(Eq.38)}$$

where $|\mathbf{S}| = 2k\sin(\theta/2)$, $k = 2\pi n/\lambda_0$ and J_0 is the zero of the Bessel function. The intensity of the transmitted beam through a scattering tissue layer having a mean scattering density ρ_{ms} and thickness l is defined by the expression

$$I = I_0 e^{-\rho\sigma_s l} \qquad\qquad \text{(Eq.39)}$$

where I is the incident beam intensity and $\sigma_s = \frac{1}{\rho I_0}\int_{4\pi} I(\theta)\mathrm{d}\Omega$ is the scattering cross-section.

3.3 Tissue clearing

The aim of clearing techniques is to effectively modulate parameters responsible for tissue opacity to facilitate light transmission. This is achieved by reduction or removal of reflecting and absorbing components of the samples, and by homogenising the RI throughout the specimens, thereby effectively minimizing light scattering.

3.3.2 Short history of tissue clearing

The first ever clearing method was described in 1914 by Walter Spalteholz. He rendered human hearts transparent to study their vessel system (75). After a long-lasting dehydration process, RI matching reagents such as methyl salicylate or benzyl benzoate "Wintergrünöl" were used to achieve tissue transparency. With this method, he succeeded to visualize macrostructures of transparent human samples. However, without the investigation and analytical tools available nowadays, such as fluorescent labelling, light-sheet microscopy, electronic cameras, and 3D processing programs, it was not possible to quantify his findings. Without such tools, he could only deliver some qualitative insight into human anatomy. Due to this lack of technology, tissue clearing remained dormant for almost 90 years until Arno Voie published in 1993 the first modern version of a light-sheet microscope (OPFOS) equipped with a CCD camera. This setup was used for imaging of fluorescein-labelled cleared inner ear bone structures of guinea-pigs (76). However, this approach remained mainly unnoticed until 2007 when Hans-Ulrich Dodt showed the first application of a light sheet microscope, termed "Ultramicroscope", in combination with a cleared hippocampus of a GFP (green fluorescent protein) labelled transgenic mouse (59). Shortly after this reincarnation of the clearing technique, neuroscience became the main driving force for innovations, and the main three
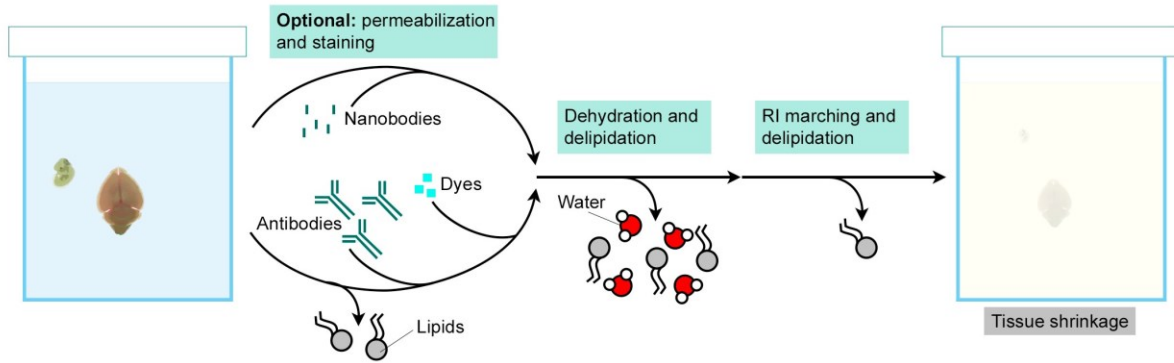
22

methods were developed on which all future approaches were built upon (**Table 1**). These methods, thereby, are dividing the tissue clearing field in three major categories: (i) in 2012 hydrophobic approaches deriving from the 3DISCO method (*77, 78*), (ii) in 2011 and 2014 hydrophilic approaches deriving from the Scale-CUBIC method (*23, 79*) and (iii) in 2013 hydrogel embedding based tissue clearing approaches deriving from the CLARITY method (*80*) (**Fig.7**).

Table1: Summary of chemicals used for different clearing methods

Chemical	Group	Role in tissue clearing	Cocktail or protocol
Methanol	Alcohol	Dehydration and permeabilization	iDISCO, iDISCO+
Ethanol	Alcohol	Dehydration	BABB, EyeCi
1-Propanol	Alcohol	Dehydration	FluoClearBABB, 2ECi
tert-Butanol	Alcohol	Dehydration	FluoClearBABB, uDISCO, PEGASOS
Tetrahydrofuran	Ether	Dehydration	3DISCO, iDISCO, vDISCO
hydrogen peroxide	Peroxide	Bleaching	DEEP-Clear, EyeCi, 2ECi
Benzyl alcohol	Aromatic alcohol	RI matching and delipidation (putative)	BABB, vDISCO
Benzyl benzoate	Aromatic ester	RI matching and delipidation (putative)	BABB, PEGASOS, vDISCO
Ethyl-3-phenylprop-2-enoate (ethyl cinnamate)	Aromatic ester	RI matching and delipidation	Ethyl cinnamate method, EyeCi, 2ECi
Dibenzyl ether	Aromatic ether	RI matching and delipidation (putative)	3DISCO, iDISCO, iDISCO+
Diphenyl ether	Aromatic ether	RI matching and delipidation (putative)	uDISCO
Hexane	Alkane	Dehydration and delipidation	BABB
Dichloromethane	Alkyl halide	Delipidation	BABB, vDISCO
Glycerol	Polyol	RI matching	Scale reagents, CLARITY, LUCID
Sucrose	Oligosaccharide	RI matching	ScaleCUBIC2, UbasM-2
d(−)-Fructose	Monosaccharide	RI matching	SeeDB, FRUIT
d(−)-Sorbitol	Monosaccharide	RI matching	sRIMS, ScaleS, STP tomography
Xylitol	Monosaccharide	Dehydration and RI matching	ClearSee
Methyl-β-cyclodextrin	Oligosaccharides	Delipidation (extracting cholesterol)	ScaleS, vDISCO
γ-Cyclodextrin	Oligosaccharides	Delipidation (extracting cholesterol)	ScaleS
Polyethylene glycol	Polyether	RI matching	ClearT2, PEGASOS
Dimethyl sulfoxide	Sulfoxide	RI matching	ScaleS, STP tomography
Urea	Urea	Hydration (putatively contributes to expansion and hence RI matching) and chemical penetration	Scale reagents, ScaleCUBIC reagents, UbasM, FRUIT, ClearSee, vDISCO
1,3-Dimethyl-2-imidazolidinone	Urea	Hydration (putatively contributes to expansion and hence RI matching) and chemical penetration	UbasM-1, UbasM-2
Formamide	Amide	Putatively similar mechanism to urea	ClearT, ClearT2, RTF

23

N- Methylacetamide	Amide	RI matching	Ce3D
Nicotinamide	Aromatic amide	RI matching	CUBIC- R , CUBIC- R+
N- Methylnicotinamide	Aromatic amide	RI matching	CUBIC- R , CUBIC- R+
Antipyrine	Phenyl pyrazolone	RI matching and expansion	CUBIC- X, CUBIC- R , CUBIC- R+
5-(N-2,3- Dihydroxypropylacetamido)- 2,4,6-triiodo- N,N'-bis(2,3-dihydroxypropyl) isophthalamide (iohexol)	Contrast reagent	RI matching	RIMS, SeeDB2, Ce3D
Diatrizoate acid	Contrast reagent	RI matching	RI matching reagent in SWITCH protocol, FocusClear
Iodixanol	Contrast reagent	RI matching	RI matching reagent in SWITCH protocol
N- Acetyl-l- hydroxyproline (trans-1-acetyl-4-hydroxy l-proline)	Amino acid	Relaxing collagen structure	ScaleS, vDISCO
N,N,N',N'-Tetrakis (2-hydroxypropyl) ethylenediamine (Quadrol)	Amino alcohol	Delipidation, decolorization, RI matching and pH adjustment	ScaleCUBIC-1, PACT- deCAL– Bone CLARITY, PEGASOS, vDISCO
THEED	Amino alcohol	Delipidation, decolorization and RI matching	FlyClear, DEEP-Clear
Triethanolamine	Amino alcohol	Delipidation, decolorization and RI matching	ScaleCUBIC-2, RTF
N- Butyldiethanolamine	Amino alcohol	Delipidation, decolorization and pH adjustment	CUBIC- L , CUBIC- R+
Meglumine or N- methyl-d-glucamine	Amino alcohol	Delipidation and RI matching	UbasM-1, RI matching reagent in SWITCH protocol
1,3-Bis(aminomethyl) cyclohexane	Aliphatic amine	Delipidation, decolorization and pH adjustment	CUBIC- HL
Imidazole	Imidazole	Expansion and decalcification (with EDTA)	CUBIC- X, CUBIC- B
1-Methylimidazole	Imidazole	Decolorization	CUBIC- P
Sodium dodecyl sulfate (SDS)	Ionic detergent	Delipidation	CL ARITY and related protocols (PACT, PARS, ACT, FACT, FASTClear and simplified CLARITY), SWITCH
Sodium dodecylbenzenesulfonate	Ionic detergent	Delipidation	CUBIC- HL
Sodium deoxycholate	Ionic detergent	Delipidation	ClearSee
Triton X-100	Non- ionic detergent	Delipidation	Scale reagents, ScaleCUBIC-1, UbasM-1 (0.2%), Ce3D (0.1%), SUT, CUBIC- L , CUBIC- HL , vDISCO
Tween 20	Non- ionic detergent	Delipidation	FocusClear
CHAPS	zwitterionic detregent	Delipidation	SHANEL
EDTA	EDTA	Decalcification	PACT- deCal, Bone CL ARITY, CUBIC- B, PEGASOS, vDISCO

Hydrophobic methods

Optional: permeabilization and staining

Nanobodies

Dyes

Antibodies

Dehydration and delipidation

RI marching and delipidation

Water

Lipids

Tissue shrinkage

Hydrophilic methods

Optional: Permeabilization

Optional: bleaching

Pigment: melanin

Optional: staining

RNA probes

Delipidation and depigmentation

Other pigments

Optional: staining

RI marching

Original size

Expansion and RI matching

Mild expansion of size

Hydrogel embedding based methods

Synthetic gel

Monomer

Initiator

Polypepoxid

Reinforced tissue gel

Delipidation: active or passive

Optional: staining

Optional: synthetic gel

RI marching

Original size

Expansion

Expansion of size
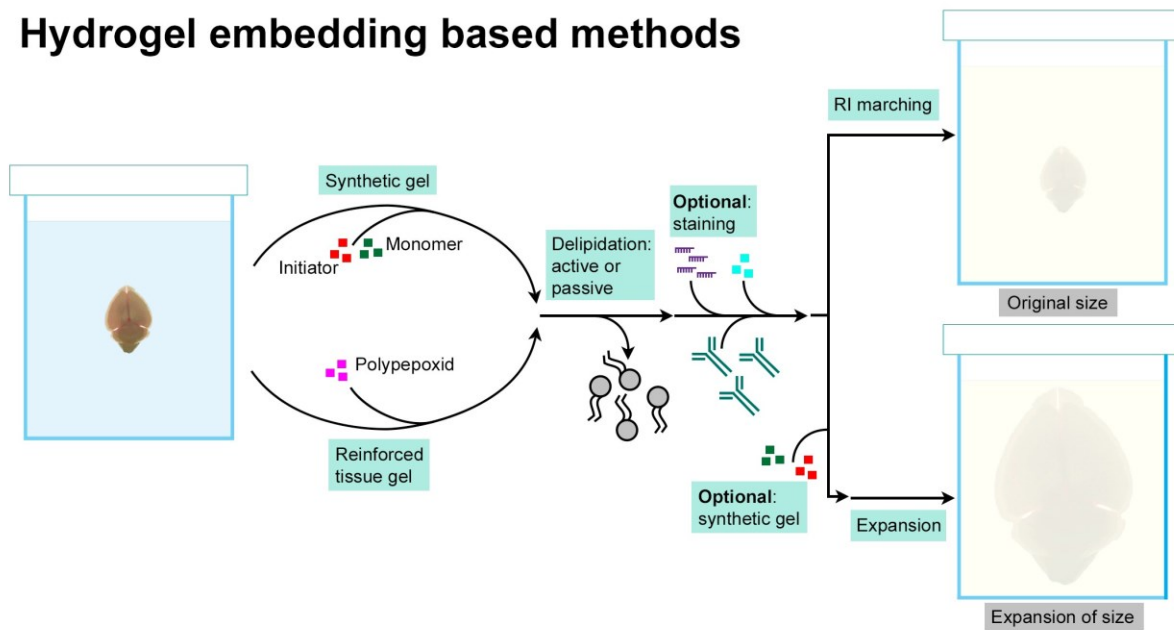
Figure 7: Principles of major clearing strategies

25

Some approaches such as the DEEP-Clear method, presented in **chapter 8** (*81*), or one iDISCO application (*82*), use steps from both hydrophobic and hydrophilic tissue clearing and are categorized according to their final RI matching solution.

3.3.2 Hydrophobic tissue clearing

Hydrophobic tissue clearing is most commonly a two-step process: (1) Dehydration with an alcohol or ether removes water (RI: 1.33) and lipids (RI: 1.5), two of the major scattering components, from the tissue (RI: 1.44-1.56). If bone is the tissue of interest a decalcification step is sometimes included prior to dehydration. (2) Further lipid solvation and tissue clearing. The final RI matching medium is usually an organic solvent (*59, 77, 78, 82-93*) (**Table 1**) ideally having a very high index of refraction to match the RI of dehydrated protein (RI: ~1.56) (*94*).

Because of the general simplicity and the high resulting transparency, hydrophobic tissue clearing found many applications ranging from neuroscience and developmental biology to stem cell- and cancer research (*78, 95-99*).

The timeframe of the whole clearing process is very much dependent on tissue properties, agent, and sample size. If taking the rodent model, mouse, the main target of most clearing protocols, as an example, the size-related clearing times become apparent. An E13.5 mouse embryo needs 1-2 days (*82, 100*) to be cleared with most protocols, an adult mouse brain 2-7 days (*77, 78, 83-86, 91*), and for a whole adult mouse, the shortest protocols take several weeks (*81-83*). Hydrophobic tissue clearing causes shrinkage of organs. This is due to the fact that tissue is usually composed of 70-80% water, forming a hydrogen bond network with the remaining tissue components (*101, 102*). A dehydration substance replacing the space occupied by water has a much lower hydrogen bonding ability, thus the tissue shrinks and hardens (*44*). The amount of shrinkage can be substantial, up to one-third of the original size depending on the ability of the utilised dehydration agent to donate hydrogen (*85*). This can be considered both as an advantage and disadvantage. On the one hand, sample size reduction reduces the field of view and depth needed for whole-organ imaging, on the other hand, shrinkage is per definition a tissue deformation. While in single organs the shrinkage is reported to be isotropic, in the context of a whole-body, the differences between soft and hard tissue can lead to anisotropic deformation of the general morphology (*85-87*). Additionally, whole mouse approaches have so far never achieved full-body transparency, as can be immediately seen when inspecting the figures in the respective publications (*85-87*). In contrast, mouse embryos and brains can be rendered highly transparent.

Despite other applications, the majority of the clearing field was and is still partially driven by the goal to improve methods for transgenic fluorescent-reporter signal preservation in the adult mouse brain. **Chapter 6** contains a publication describing such an approach (sDISCO) (*84*).

The utilised RI medium should ideally have five properties: (i) low light scattering and light absorbance, (ii) a high lipid solving capacity, (iii) an RI of at least 1.5, (vi) very good fluorescent signal preservation and (v) the sample should be storable in the liquid for long time periods. The 3DISCO approach (*77, 78*) reached very high transparency, thereby fulfilling point (i), (ii) and (iii); however, the transgenic fluorescent signal diminished sometimes even after one day. This could be attributed to the presence of peroxides and aldehydes in the utilised RI media, either dibenzylether (DBE) or a 1:2 mixture of benzyl alcohol with benzyl benzoate (BABB or Murray's clear). Even after initial purifications with activated aluminum oxide by column-absorption chromatography, peroxides and aldehydes would gradually return as degradation products of DBE or BABB.

The sDISCO approach succeeded in hindering the reappearance of these signal quenching by-products by stabilizing the RI medium with a radical-scavenging chemical called propyl gallate (*103, 104*); thereby preserving the fluorescence for more than a year (*84*). Other approaches such as uDISCO utilized a similar strategy by using Vitamin-E (*85*). Another fluorescence preserving approach is to use chemicals which stabilize the protein conformation, such as polyethylene glycol (PEG) (*105*) or polyethylene glycol methacrylate (PEGMMA) as shown in the PEGASOS method (*86*). With the development of these modern RI matching media, signal preservation and sample storage no longer represent a limitation, thereby enabling multiple imaging sessions and long-term reanalysis of specimens. However, fluorescent signal bleaching properties under laser light conditions could still be improved. A way to address this issue is embedding of the cleared tissue in resin with the same RI as the respective clearing medium (*106*). The sample can be illuminated for extended periods without any significant signal loss. Even after the occurrence of bleaching, signal regeneration could be observed after a certain amount of time. The drawback of this approach – and probably the reason for the lack of appreciation by the scientific community - is that the solving properties of RI matching media interact with the resin, thereby rendering it opaque after an unpredictable amount of time.

When looking at the protocols separately it is noticeable that mouse embryos display a small variance, in comparison to mouse brains, regarding the total processing time. To understand the reason for this difference five factors need to be considered:

(1) Lipids are one of the major scattering substances in tissue due to their high RI and ability to granulate, (*70, 107-110*) and due to their strong integration in the tissue they are much harder to remove than water. (2) An embryo basically consists of water in comparison to a lipid-rich mouse brain. (3) Myelination, and thus lipidation, of the brain increases with the age of the mice. Four week old mice have approximately the same brain size as eight week old mice. However, if processed for the same amount of time, with any of the published protocols, the younger mouse brains appear more transparent. (4) The lipid removing properties of organic solvents are considered to be the main mechanism behind delipidation. However, the final RI matching stage represents in any dehydration-based method by far the shortest incubation step. If a brain remains partially not transparent or opaque after one day of RI medium incubation, it will remain so independent of further incubation length. (5) If for such a brain the whole dehydration or a part of the dehydration procedure is repeated, the newly achieved result is in most of the cases complete transparency after subsequent RI matching.

By excluding the RI matching medium as the main source of delipidation and by taking the tissue composition into account, it can be concluded that the utilised dehydration agent is the key component for a complete delipidation and thus tissue transparency. Although tissue transparency is very important, fluorescent signal preservation should also be considered.

Very early clearing methods used ethanol or methanol as dehydration agents. These media have a negative effect on fluorescent signal, thus allowing only short incubation times when fluorescent signal preservation was of importance. The clearing was therefore limited to small specimens in such cases (*59, 100*). 3DISCO, using tetrahydrofuran (THF) as a dehydration chemical and DBE or BABB as a RI matching medium, was the first method enabling the generation of highly transparent whole adult mouse brains while preserving endogenous GFP or YFP (yellow fluorescent protein) signal for at least one day. The removal of peroxides and aldehydes from the THF (sDISCO) (*84*) and further temperature and pH condition adjustments (FDISCO) (*88*) resulted in better fluorescent signal preservation during dehydration. Nevertheless, every developed clearing method for mouse brain, regardless of being dehydration-based or not, used the very strong Thy1-GFP-H or Thy1-YFP-M reporter line, with a high yield of fluorescent signal, as a reference for method establishment (*111*). When THF is used for extended dehydration periods (e.g. for the whole mouse), or on transgenic models with weak expression patterns, no detectable signal remains. The necessity for better signal preservation during dehydration led to methods like FluroClearBABB (*83*), uDISCO (*85*) or PEGASOS (*86*), which utilise 1-propanol or the even more effective tert-butanol as a dehydration agent. The advantage was the possibility for longer tissue processing times and better fluorescence preservation, but at the cost of sample transparency.

The general two reasons for fluorescence loss are either denaturation of the protein or protonation of the chromophore. Fluorescence loss caused by protonation can be reverted by a simple pH change (*8*) or rehydration (*83*), thereby putting fluorophores back in their deprotonated state (*112*). Signal loss through denaturation is however irreversible. One of the main reasons for protein denaturation can be related to the length of the carbon chain and the branch number of the hydrocarbon portion of the dehydration agent (*113, 114*). Alcohols with shorter carbon chains diffuse better inside a fluorophore, causing increased protein denaturation. Therefore, long-chain alcohols are preferable for dehydration. However, the solubility of alcohols in water decreases with carboxyl chain length, hence limiting the range of alcohol-based dehydration agents to alcohols with not more than five carbon atoms (**Fig.8**).
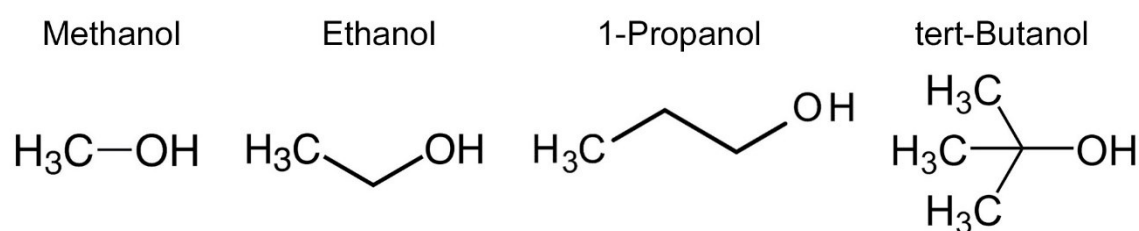
Figure 8: Carbon chain length of different dehydration agents

Further, it has been shown that GFP is thermal-sensitive (*115, 116*). This can be attributed to the higher unfolding rates of the chromophore at increased temperature, and the thermally induced enhancement of collisions. However, these effects vary depending on the utilised dehydration medium, as with THF and ethanol fluorescence is preserved the best at 4°C (*88*) while with 1-propanol and tert-butanol incubation temperatures can be up to 30°C - 35°C (*83, 85*). In addition, the concentration of the utilised alcohol can have a strong impact on fluorescence preservation as GFP denaturation occurs in 70% and 95% methanol and 70% ethanol while almost no loss is visible at 50% methanol and 50% and 95% ethanol. Further 70% 1-propanol causes a partial chromophore denaturation while 50% and 95% 1-propanol and 50%, 70% and 95% of tert-butanol cause no signal loss (*113*). Finally, pH represents another important factor for chromophore preservation. Ethanol adjusted with phosphate-buffered saline (PBS) to neutral pH was reported to reduce the GFP loss occurring during dehydration (*117*). Nevertheless, PBS tends to precipitate in higher concentrated hydrophobic agents (*118*). Other approaches used triethylamine or quadrol, which are completely soluble in pure ether or alcohol, to adjust the pH of THF (FDISCO) or tert-butanol (FluoClearBABB, PEGASOS) to pH 9-9.5 resulting in improved signal preservation (*83, 86, 88*). However, pH

adjustment with triethylamine is not applicable to every alcohol, as methanol with a pH of 9 shows only minor preservation (10% of the original signal) of fluorescence (*83*).

The latest dehydration-based approaches show very good results with transgenic GFP, YFP or DsRed (*119*). However, they have difficulties with the preservation of fluorescent reporter signals from the mFruit family such as mCherry or TdTomato. The reason for the loss is not completely understood but can be partially attributed to the structure of the fluorophores (*119*).

The tight packing of the amino acid residues of the Aequorea derived monomeric β-barrel structure of EGFP or EYFP provides a high level of stability to the protein against changes in pH, temperature, formalin fixation and the disruption of common denaturing agents. Further, the lack of gaps and clefts inhibit the entry of small ligands, and the position of the chromophore in the center of the β-barrel structure provides high photostability (**Fig.9a**) (*120*).
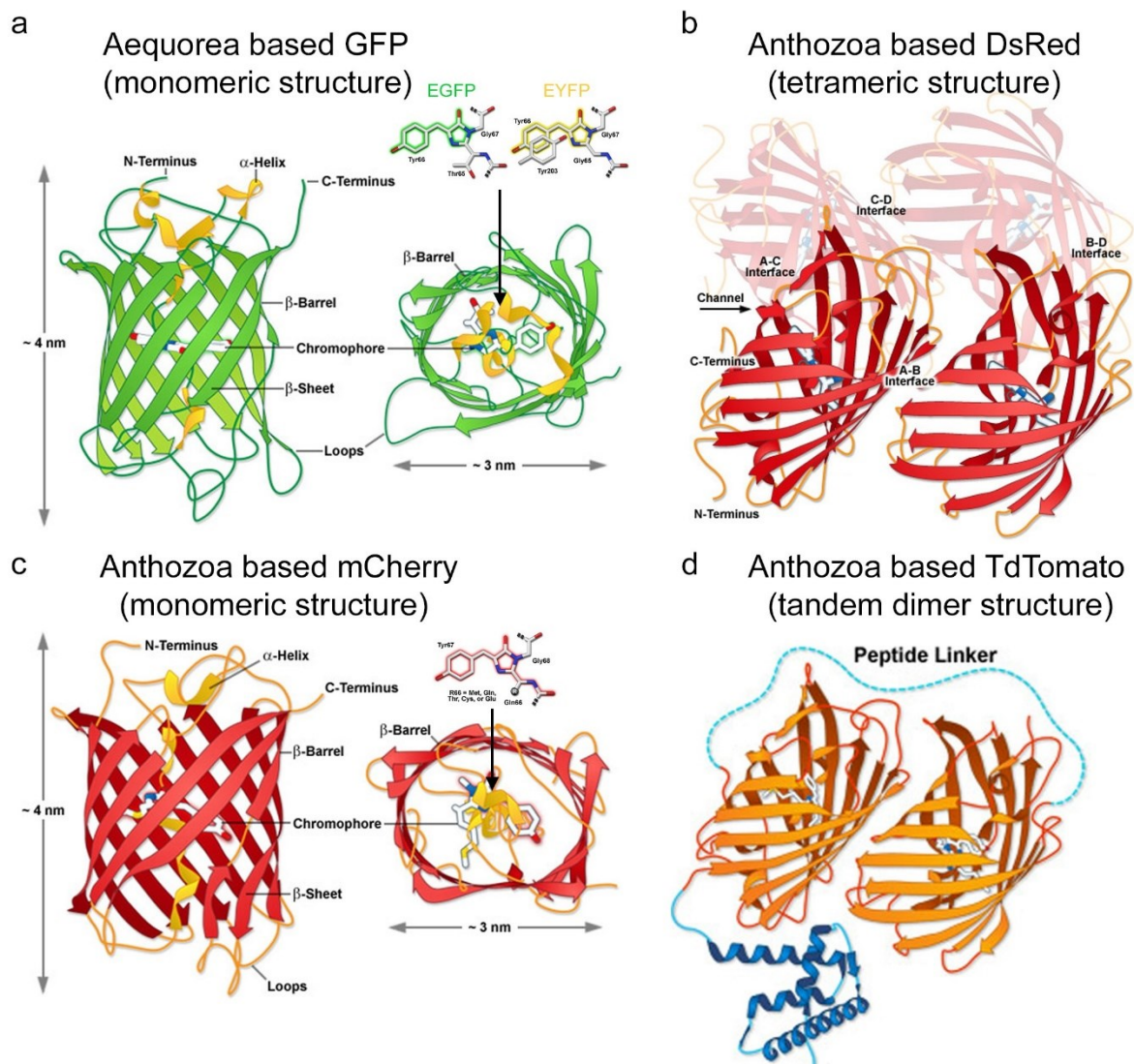
Figure 9: 3D structure of different fluorophores. (**a**) Monomer β-barrel structure of EGFP and EYFP with the chromophore localized in the center (arrow). (**b**) Tetramer structure of DsRed composed of two dimers each having two β-barrels. (**c**) Monomer β-barrel structure of mCherry - derived from DsRed. The arrow indicates the position of the chromophore. (**d**) Tandem dimer structure of TdTomato composed of two β-barrels – derived from DsRed. Top view of the protein in (**a**) and (**c**) show the difference in shape and packing of the two beta-barrels. Modified, image source: doi:10.1039/b901966a used with the permission of the publisher Royal Society of Chemistry. License ID 1039428-1

The tetrameric structure of the Anthozoa derived DsRed consists of four very tightly packed protomer β-barrels each with a chromophore located in the center (**Fig.9b**). Despite the low correlation in the amino acid homology (23%) with the Aequorea derived GFP, the individual β-barrels, although more elliptical, show very similar features. The center of the tetramer is coated with amino acid residues and salt bridges allowing for water molecule incorporation between each unit. The good photostability and tolerance to pH, temperature, and denaturation can be attributed to the compact tetramer. Both, mCherry (**Fig.9c**) and TdTomato (**Fig.9d**) are derived through extensive mutagenesis from DsRed. Where mCherry has the molecular architecture of one beta-barrel (monomer), TdTomato consists of two β-barrels (tandem dimer) (*120*). The sensitivity of these two fluorescent proteins to dehydration-based approaches could be due to a couple of reasons. The most obvious is the absence of the strongly stabilizing tetramer structure. Further, although similar in shape to the β-barrel structure of the Aequorea-derived EGFP, the more elliptical geometry and slightly looser packing of the amino acid residues (**Fig.9a and c** top view) probably allow for better diffusion of alcohols to the chromophore causing denaturation.

This reduced compatibility with some fluorophores represents a limitation in animals with multiple colour coded reporter genes, or in brainbow approaches (*121*). A way to address this signal loss was shown with the vDISCO approach. In this method nano-bodies, consisting of the variable domain of the heavy chain from an antibody (*122*) directed against fluorophores, were circulated through the blood vessel system in the body of an entire mouse. This approach, although difficult, laborious, and expensive, could increase the signal up to 100 times. Further, by using fluorescent dyes in the far-red spectrum it was possible to improve the signal to noise ratio by overcoming the tissue autofluorescence, thus allowing reliable detection of subcellular details (*87*).

The preservation of fluorescence is undoubtedly important, but not essential, since visualization of such proteins can be achieved independently by immunolabelling them. In addition, transgenic mouse models are not always available. This led to the development of the iDISCO approaches (*82, 91*). iDISCO involves tissue pre-treatment with hydrogen peroxide (H_2O_2) for depigmentation, and methanol to permeabilize the mouse brain, thereby already destroying most of the fluorescent signal, if present. Further, the pre-treatment process may also purge a large fraction of the epitopes for the antibodies (*91*). In addition, the incubation steps with the antibodies usually take weeks to months for a whole brain. Despite its limitations, iDISCO based approaches have been widely used to study rodent (*82, 90*) and human embryos (*99*), adult mouse brains (*91*), and cancer biopsy tissue (*123, 124*). Another labelling approach using a H_2O_2 bleaching step is called EyeCi (*26*). This method focuses specifically on antibody labelling of structures in the mouse eyes and the removal of the insoluble pigment melanin using dehydration-based clearing methods. However, further development of new deep-tissue labelling strategies with full epitope preservation will be crucial to broaden the applications of dehydration-based tissue clearing.

Despite the successes in rodent models, human cancer and embryo analysis, dehydration-based methods, with very few exceptions (*93*), found little application in other organisms. This is mostly due to dehydration-based shrinkage artefacts and the difficulty of preserving transgenic fluorescent signals when present in non-mammalian tissue. For example, many attempts were made to develop a clearing technique for *D. melanogaster* with transgenic reporter signals, since immunolabeling through the cuticle is not possible in adult flies so far, and is very difficult in larval stages (*125*). However, the signal is usually lost (*59, 126-128*) or extremely week (*93*), even when a strong reporter with high fluorescent expression yields is used. Nevertheless, high-resolution images of autofluorescent structures could be obtained. Although not dedicated to the development of clearing techniques, **chapters 2-4** show publications including examples of 3DISCO processed adult *D. melanogaster* displaying highly detailed 3D reconstructions of autofluorescent structures. The fruit fly samples were used among others in these publications to show the resolution achievable with laser beam shaping and light sheet microscopy.

3.3.3 Hydrophilic tissue clearing

Hydrophilic tissue clearing is based on the use of water-soluble reagents to facilitate tissue transparency. The used reagents thereby form hydrogen bonds with various tissue

components such as proteins and surrounding water molecules. The clearing performance of hydrophilic approaches is usually inferior to hydrophobic methods. However, this approach has obvious advantages, such as preservation of 3D structure, protein function and protein fluorescence, when compared to dehydration-based methods. Water-based approaches can be divided into two groups, (i) simple immersion in high RI media and (ii) delipidation with hyper-hydration and RI matching.

3.3.3.1 Simple immersion in high RI medium

In simple immersion approaches, the sample is placed in an aqueous solution with a dissolved, high RI chemical. Most commercially available microscopy mounting media are based on glycerol which already has a clearing effect, although this is not very efficient. One of the first applications of water-based tissue clearing in neuroscience was on a whole cockroach brain with a RI matching medium containing diatrizoate acid (contrast agent) and Tween 20 (detergent) called FocusClear (*129, 130*). Further RI matching media are highly saturated sugar solutions like sucrose (*131*) and fructose, as used in methods like FRUIT (*132*) and SeeDB (*133*), water-miscible polar solvents such as 2,2'-thiodiethanol (TDE) (*134, 135*) or formamide, used in the Clear^T (*136*) and RTF (*137*) methods, and iohexol solved in ethylenediaminetetraacetic acid (EDTA) and Tris(hydroxymethyl)aminomethan (Tris) buffer, as used in the SeeDB2 approach (*138*).

These approaches, specialized for neuronal tissue, are very simple and fast to implement, and have a good clearing performance at small sample sizes. However, a problem of highly concentrated sugar and glycerol solutions is that they have high viscosity and thus are difficult to work with. The FRUIT approach uses urea in combination with fructose to reduce the overall viscosity. Diatrizoate- and iohexol- based media consist of molecules with an aromatic ring structure and three iodine atoms, thus these media can achieve high RIs (1.45) while still having a low viscosity (*14*). However, these contrast reagents have a large molecular size and thus would need a strong removal of plasma membranes to fully capitalize on their RI matching capacities. A general problem of all these RI matching media is that they tend to evaporate and precipitate at room temperature (*14*). TDE has a lower viscosity while having a maximum RI of 1.52, and does not form any precipitants at room temperature. However, it quenches fluorescent proteins at concentrations required for a high RI. Another general problem of these approaches is air bubbles which can be easily introduced and the difficult mounting of the samples as they are soft and usually have a lower density than the used RI solution (*14*).

Some of these approaches use different detergents like Tween 20 and Triton X-100 in low concentrations or chemicals with various degrees of lipid solving abilities such as urea, EDTA and formamide. Nevertheless, many lipids remain and thus larger samples like whole mouse brains are not sufficiently cleared.

Although, these approaches produce samples with the lowest transparency from all clearing techniques discussed in this thesis, they have some benefits and valid applications as they are compatible with a wide range of proteins and fluorescent dyes, such as DiI for lipid targeting, not compatible with other methods (*119*).

3.3.3.2 Delipidation, hyperhydration and RI matching

Most of the aforementioned hydration methods show very weak lipid removal capabilities or do not remove lipids at all. They simply try to match an average RI in the sample by exchanging the liquid in and around the tissue with a high RI medium. An alternative approach was introduced with the *Scale* method by removing the lipids with extensive Triton X-100 incubation, to lower the average RI and further to perform an increased influx of chemicals into the tissue by the strong hydration agent urea (*79*). The underlying mechanism of urea induced tissue swelling is probably due to the increased osmotic pressure inside the tissue and by relaxation and solvation of highly dense fiber proteins (*44*). To avoid excessive tissue swelling glycerol was used, with partial success, as a counter-balancer and RI matching medium (*79*). This method has, however, some limitations, including slow sample clearing speed and tissue fragility and expansion. The tissue swelling was addressed in the *ScaleS* method using a mixture of sorbitol and glycerol to counter-balance the urea induced sample expansion (*139*). Despite the stronger delipidation, both approaches still had a low clearing capacity. The CUBIC method used the hyperhydration effect of urea (25 wt%) as well as a very high concentration of detergent (15wt % Triton X-100). Further, a group of aminoalcohols that have both depigmentation and delipidation properties were tested (*23*). Thereby, Quadrol (25 wt%) showed the best ability for removal of the blood pigment heme. This is probably due to the property of Quadrol to bind the porphyrin of heme, resulting in its release. The general basic condition of the whole solution may help with its decolourizing effect. The whole mixture also has a very strong delipidation capacity as Quadrol solubilizes phospholipids by electrostatic interactions, Triton-X 100 forms micelles around the lipids, and urea increases the permeation and distribution of the chemicals. However, with increasing incubation time this solution leads to excessive swelling, tissue damage and fluorescent signal loss. Therefore,

a second solution consisting of 50 wt% sucrose, 25 wt% urea, 0.1 wt% Triton X-100 and another aminoalcohol, triethanolamine, was used for final RI matching and storage, resulting in satisfactory mouse brain transparency (*23*). To reduce the swelling and for better morphology preservation an updated version of the protocol uses 5 wt% Quadrol, 10 wt% Triton X-100 and 10 wt% urea for initial delipidation and depigmentation.

Another CUBIC approach (CUBIC-X) capitalized on the idea of expansion microscopy (discussed in 3.3.4) and focused on tissue swelling to enable super-resolution in all spatial directions of the mouse brain by physically enlarging the sample size (*140*). The delipidation/depigmentation solution from the CUBIC approach was used followed by subsequent immersion of the brain in a 20% imidazole solution for maximum expansion. To achieve full tissue transparency an RI matching medium of 55 wt% antipyrine, another tissue swelling reagent with high water solubility and molar refractivity, and 5 wt% imidazole was used (RI 1.467). For physical stability, the cleared samples were embedded in 2 wt% agarose mixed with the RI medium.

In a further CUBIC approach, 1600 chemicals were profiled and rated according to their delipidation, decolouring, and RI matching abilities (*44*). The study reported that, hydrophobic uncharged aliphatic amines, at basic conditions, have a higher delipidation capacity, due to their high lipophilic logP values (octanol-water partition coefficient; measures the amount of a solute that dissolves in the water portion versus an organic portion) as calculated by Hansen's solubility parameters (*141*) than anionic and non-ionic detergents which generally show high lipid solubility. This can be explained by the slower tissue penetration of detergents, due to their tendency to form large aggregates of surfactant molecules (micelles), resulting in a lower delipidation efficiency. Further, it was reported that the depigmentation and lipid solubility are stronger at higher pH. Another finding was that polar groups, as $-NH_2$ or $-OH$, and longer chain length between these polar groups ($\geq$ 3C atoms) were related to strong depigmentation properties. Finally, chemicals with amide groups generate clearing solutions with high RI values. According to the chemical screening 1-methylimidazole, N-butyldiethanolamine, and 1,3-bis(aminomethyl)cyclohexane showed both high lipid solubility and depigmentation scores. With these results, chemical cocktails were produced - depending on the nature of the sample to be cleared, e.g. lipid content, muscle tissue, level of pigmentation, bone and transgenic signal. For whole mouse clearing (CUBIC-P) a combination of 5 wt% 1-methylimidazole, 10 wt% N-butyldiethanolamine and 5 wt% Triton X-100 was used. For mouse brain and other single organs, with focus on transgenic fluorescent signal preservation (CUBIC-L), 10 wt% N-butyldiethanolamine, 10 wt% Triton X-100 performed the best. For very fast delipidation and clearing of human brain tissue (CUBIC-HL) a 10 wt% 1,3-

bis(aminomethyl)cyclohexane, 10 wt% sodium dodecylbenzenesulfonate with a pH of 12 adjusted by p-toluenesulfonic acid was most applicable. If bone tissue was to be examined, addition of an intermediate step between the two CUBIC-L incubation steps comprising a 10 wt% EDTA, 15 wt% imidazole solution showed the best results. For final RI matching, the highest transparency was achieved with 45 wt% antipyrine, 30 wt% N-methylnicotinamide, optionally pH 8-9 adjusted by N-butyldiethanolamine (CUBIC-RA).

A CUBIC approach focusing on antibody labelling (CUBIC-HV) demonstrated that a formalin-fixed and delipidated cleared brain can be characterized as a charged cross-linked polypeptide gel (*142*). Further, they described essential conditions for efficient thick tissue staining such as (i) the modulation of the interaction between dye and antibody with the tissue by chemical substances such as Quadrol or urea, (ii) usage of directly conjugated antibodies and (iii) incubation temperature, ionic strength, detergent and antibody concentration and limited tissue digestion (optional).

CUBIC based protocols achieve high tissue transparency of single organs - especially mouse brain tissue. However, clearing of human tissue and whole mouse and marmoset bodies is time-intensive (weeks to months), and still needs some improvement. Further, CUBIC based solutions are reported to damage the pre- and post-synaptic fabric and are not compatible with RNA labelling due to their high pH. Additionally, CUBIC approaches can remove porphyrin-related pigments, however, they have little to no effect on other pigment types such as drosopterins and melanin. Finally, CUBIC approaches have been used for many applications in mammalian systems, such as drug administration studies (*143*), analysis of mouse brain cancer metastasis (*144*), different mouse brain connectome studies (*145-150*), observation of haematopoietic stem cells in bone marrow (*151*), studies of lung carcinoma (*152*), single-cell lineage tracing in the mammary gland, (*153*) and development studies of the heart (*154*). However, with one exception in crustacean where auto-fluorescence was imaged (*25*), no model systems other than mammalian were investigated.

The main publications in this thesis, found in **chapters 5** and **8**, are the CUBIC based approaches called *FlyClear* (Pende *et al.* 2018) and DEEP-Clear (Pende *et al.* 2020). These publications focus on a variety of model organisms outside the mammalian system (Fruit fly, bristle worm, Hawaiian bobtail squid, longfin inshore squid, zebrafish and axolotl). Both methods use the urea-based hyperhydration mechanism and Triton X-100 for delipidation, with the main active depigmentation chemical being the aminoalcohol THEED. Depending on the concentrations of the components used, the solutions are termed *Solution-1* or *Solution-*

1.1. Further, in both publications the focus is on decolouring strategies for a variety of pigments which cannot be removed with previously published methods from all clearing categories (**Fig.10a-g**). DEEP-Clear additionally uses an acetone treatment step, prior to *Solution-1* or *Solution-1.1* incubation, causing a synergistic effect for depigmentation speed and removing pigments of different nature. Further, the overall clearing time ranges from a couple of hours (bristle worm, squid hatchlings, juvenile zebra fish) to one day for specimens measuring several centimetre (juvenile axolotl and adult zebrafish). These short incubation times preserve tissue RNA content and morphology, and at the same time reduce clearing induced tissue damage to a minimum. In contrast, FlyClear needs 3-5 days for depigmentation of adult fruit fly eyes. The difference in clearing speed can be attributed to the chitinous exoskeleton of the fruit flies. As mentioned earlier, porphyrin-related pigments such as the red coloured heme from blood can be removed with already existing approaches, however, most methods have not been optimized for the removal of other body pigments. Representatives of these methods can be found in (**Fig.11**). However, hydrogel-based approaches were excluded since they require transcardial administration of the gel into the body. Without the tissue stabilizing properties of this gel matrix the harsh chemical treatment with SDS leads to strong tissue damage and thus this data is not shown. FlyClear and DEEP-Clear focused on whole-body clearing and depigmentation, however, they differed in their emphasis on further applications. The main goal of FlyClear was the preservation of transgenic fluorescent reporter signal from fruit flies at different developmental stages, i.e. 3rd instar laverve, pre-pupa, pupa and adult flies. Whereas, DEEP-Clear focused on the versatility and compatibility with different molecular labelling tools like transgenic reporter lines, IHC, FISH, EdU and picolyl azide-based click chemistry and dyes like DAPI.

Both methods are unique in their achievements as *FlyClear* was the first clearing method reported to preserve transgenic signals in *D. melanogaster* while DEEP-Clear provided a depigmentation, clearing and labelling approach for established and emerging model organisms.
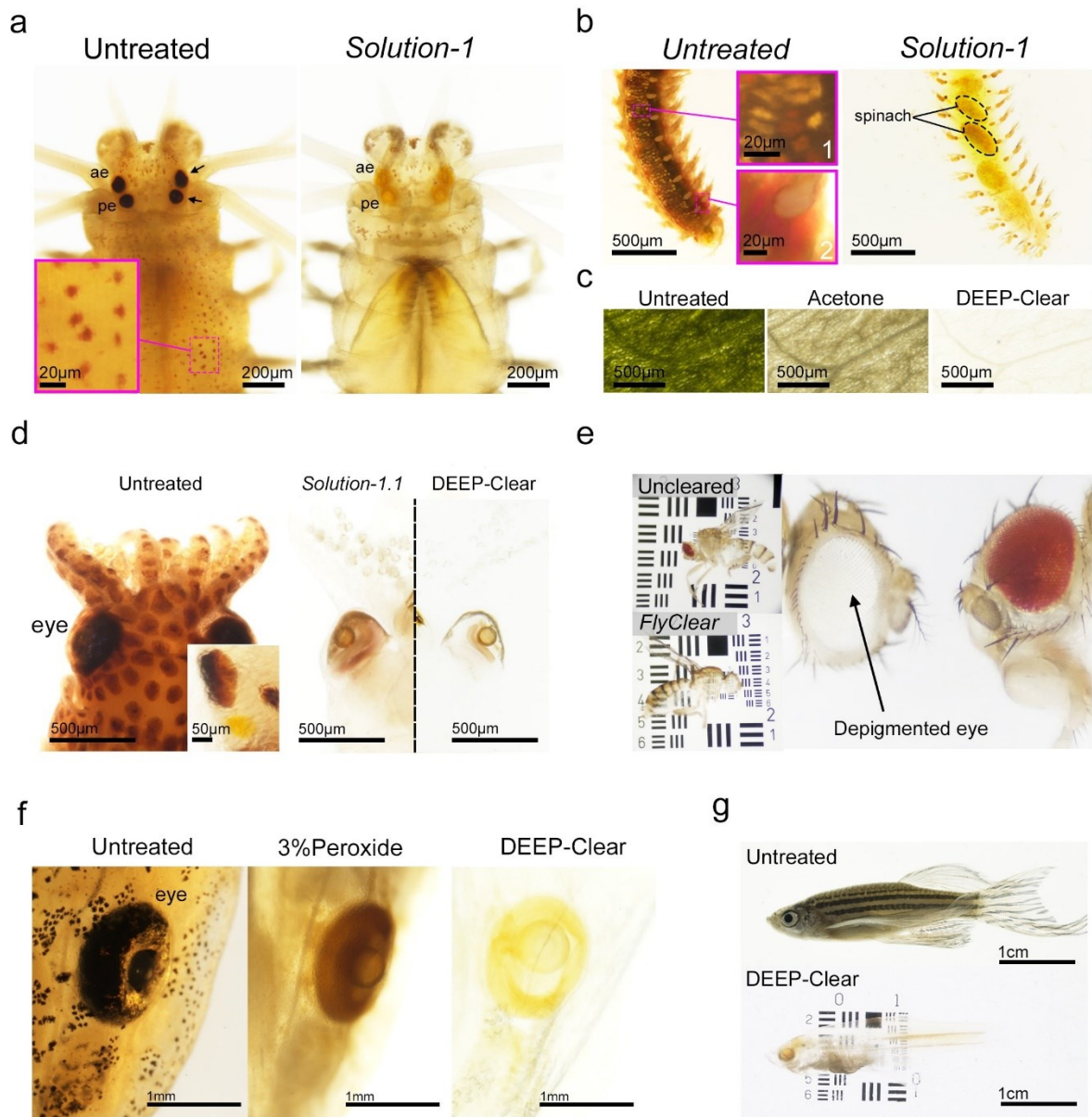
Figure 10: The FlyClear and DEEP-Clear methods promote the efficient removal of pterin-, heme-, ommochrome-, carotenoid-, chlorophyll- and melanin-based pigments. (**a**) Comparison of control (left) and Solution-1-treated (right) bristle worm specimens. In control specimens, arrows point at pterine-containing eyes and the inset shows a larger view of the indicated area displaying erythrophores in the trunk. (**b**) Comparison of control (left) and Solution-1 treated (right) worm trunks. Insets: larger view of the indicated area displaying erythrophores (1) and heme-based blood pigments (2). (**c**) Clearing by acetone (middle) and full DEEP-Clear processing (right) of chlorophyll-based pigments in spinach leaves. (**d**) Comparison of control (left), Solution-1.1 and DEEP-Clear-processed (right) hatchlings of Hawaiian bobtail squid. Control panels show eye pigments and ommochrome-based body pigments (enlarged in insert). (**e**) Uncleared (upper picture) adult fly in PBS and corresponding *FlyClear* processed (lower picture) side of the same fly. Magnification shows the removal of drosopterins and ommochrome pigment from fruit fly eyes. (**f**) Comparison of control (left), peroxide- (middle) and DEEP-Clear-processed axolotl specimens, focusing on the melanin-based eye and body pigments. (**g**) Comparison of untreated (upper picture) and DEEP-Clear treated (lower picture) adult zebrafish specimens. ae, anterior eye; posterior eye. Images adapted from DOI: 10.1038/s41467-018-07192-z and DOI: 10.1126/sciadv.aba0365

38
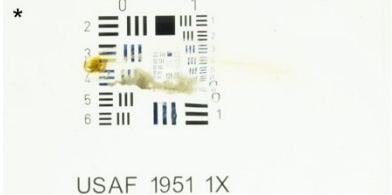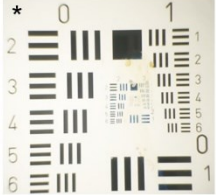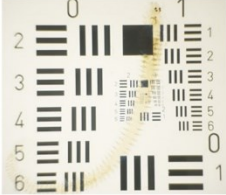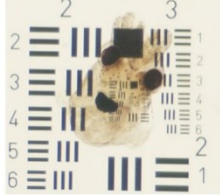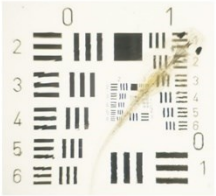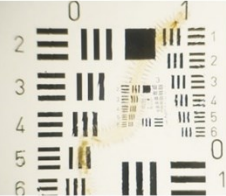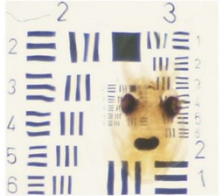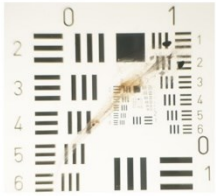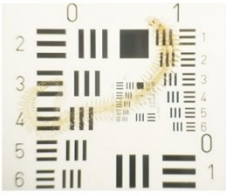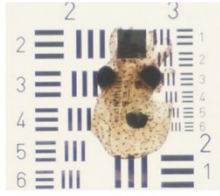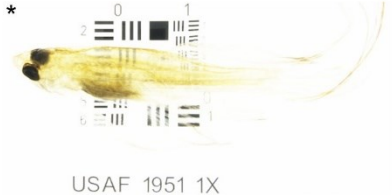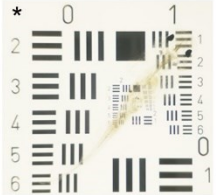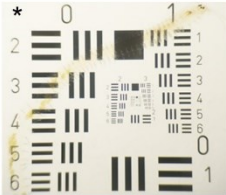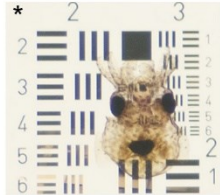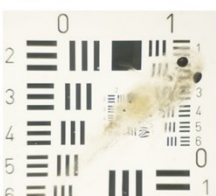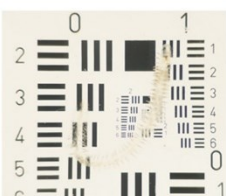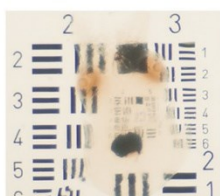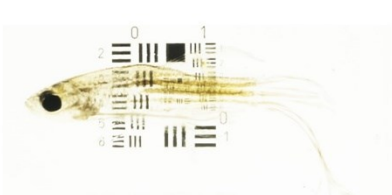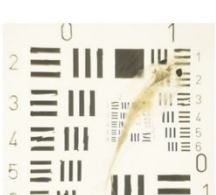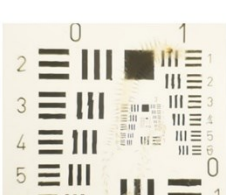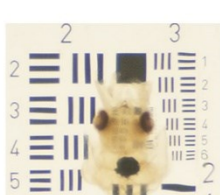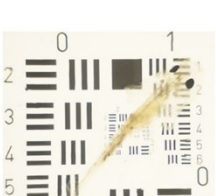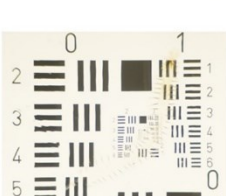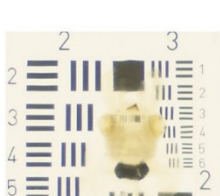
Figure 11: Synopsis of the impact of existing clearing techniques for tissue depigmentation and transparency of zebrafish, axolotl, bristle worm and squid specimens. Effects of different dehydration based (ECi, PEGASOS, 3DISCO and iDISCO) and hyperhydration based (CUBIC, CUBIC-L and CUBIC-HL) methods on eye and body pigments, tissue integrity and transparency. Where applicable, a bleaching step was performed as detailed in the respective protocol (indicated by asterisks). Images from DOI: 10.1126/sciadv.aba0365

3.3.4 Hydrogel embedding based tissue clearing

There are two major ways to perform tissue fixation. First, simple immersion in the fixative, where chemicals diffuse passively into the brain tissue. Second, and most commonly used in rodent models, perfusion with fixative-containing fluid through the vascular system, where it then diffuses out of circulation into the tissue (*155*).

Formalin is a fixative that enables tissue clearing under relatively mild conditions. Due to its small size and high tissue permeability – 1mm per hour in soft tissue – it is in general one of the most widely used fixatives for biological samples (*156, 157*). The initial step for tissue fixation is to dissolve the polymerized crystalline solid form of formaldehyde (formalin), paraformaldehyde (PFA), in water or PBS. Formalin reacts by linking the N-terminal amino groups and the basic amino groups of endogenous fluorescent proteins to form methylol adducts (*158, 159*). This is easily reversible by simple PBS washes (*156*). These methylol adducts are further conjugated through strong bonds with adjacent histidine, arginine, tyrosine, glutamine, tryptophan, asparagine and N-terminal amino groups of proteins. Although not well understood, it is assumed that in the Mannich reaction, induced by several antigen retrieval conditions such as heat or microwaves, the crosslinking between different amino acids can be dissolved (*160, 161*). Because formalin does not bind to lipids, they are effectively washed out with all lipid removing clearing strategies. A major drawback of this type of fixation is that formalin molecules only form networks of physically linked neighbouring proteins, but it fails to link spatially isolated proteins (*155*). Further, it is not optimal for binding relatively small molecules such as dopamine or serotonin which may lead to loss of important biological information. The amount of protein loss is also dependent on the subsequent tissue processing; for example, in standard histology about 24% of protein is lost, approximately 41% when treated with 4M urea, and about 65% when treating with 4% sodium dodecyl sulfate (SDS) solution (*80*). Stronger fixation strategies include picric acid (*162*), glutaraldehyde (*163, 164*) or a combination of all the aforementioned fixatives called Bouin's solution (*155, 165, 166*). The drawback of picric acid is that it is highly explosive (*167*) and glutaraldehyde can

cause very strong autofluorescence and has a low permeability making uniform fixation difficult (*168*). However, the SWITCH clearing method (4% formalin and 1% glutaraldehyde) demonstrated that glutaraldehyde in an acidic buffer (pH 3) (SWITCH-OFF) can penetrate through large tissue and that the crosslinking reaction can be initiated throughout the tissue by replacing the acidic buffer with a neutral pH buffer (SWITCH-ON) (*169*). Subsequently, delipidation occurs through boiling the sample at 80°C in an aqueous clearing solution containing 200mM SDS, and the final RI matching stage is performed with a 23.5% (w/v) n-methyl-d-glucamine, 29.4% (w/v) diatrizoic acid, and 32.4% (w/v) iodixanol solution. This protocol is physically and chemically very stable and despite harsh clearing conditions as in such harsh clearing conditions no tissue deformation occurs and only 3-5% of protein loss was reported. However, the whole procedure is relatively time consuming, lasting at least two weeks for an adult mouse brain.

Another clearing approach providing excellent protein preservation – only 8% loss – and high tissue transparency while having a total processing time of 5-7 days is CLARITY (*80*). In this method rodents are initially perfused with a polymer gel (hydrogel) consisting of formalin, acrylamide, N,N'-methylene bisacrylamide and the thermal polymerization initiator VA-044. After one day of incubation at 4°C, methylol adducts are formed between the amino groups of the proteins and the aldehyde group of formalin. Polymerization is initiated with incubation at 37°C and the biomolecules are covalently linked to the amide group of the solidified hydrogel matrix. Unlike formalin fixation, where molecules are linked to each other, in CLARITY they are embedded in the matrix, thereby preserving spatially isolated proteins. The hydrogel additionally provides physical and chemical stability. Subsequently, lipid removal is either passive by simple immersion in an SDS/Boric acid buffer (pH 8.5) at 37°C for 3-4 weeks (*170*) or by active removal with the same buffer in an electrophoretic tissue clearing chamber (ETC) for 3-5 days (*80*) (**Fig.12a**). Mouse brains are usually swollen after this step, however, they shrink back to normal size after RI matching (**Fig.12b**). The RI matching medium used in the CLARITY method is called FocusClear™ and has a RI of 1.45. Mouse brains in FocusClear™ are rendered very transparent, nevertheless, the medium is very expensive (50ml cost 1200€) and the sample turns opaque after a couple of days of incubation in the solution. **Chapter 2** and Figures 6 and 7b of the publication present an adapted version of the CLARITY method with a meglumindiatrizoate solution adjusted to a final RI of 1.45 as a RI matching medium.

a
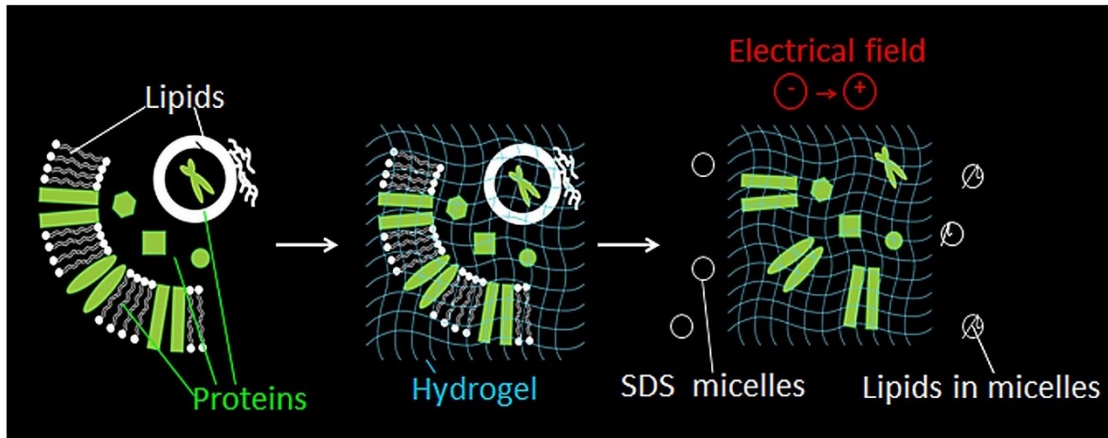
b
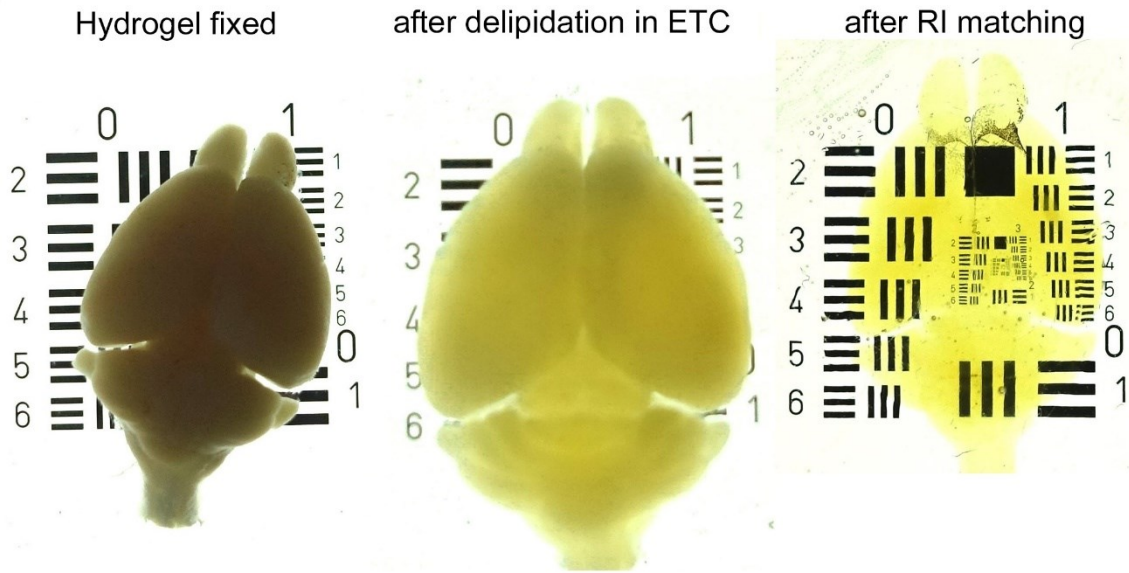
Figure 12: Principle and different clearing steps of CLARITY procedure. (**a**) Unlike lipids, proteins are bound in the hydrogel meshwork. Lipids are trapped in SDS micelles and are transported in an electric field out of the tissue while the proteins remain. (**b**) Left: Mouse brain fixed in the hydrogel. Middle: Mouse brain after delipidation in electrophoretic tissue clearing chamber (ETC). Right: Mouse brain RI matched to 1.45 with meglumindiatrizoat solution.

With the CLARITY approach, small samples can be labelled using IHC, however the staining of large tissue requires very long incubation times and the staining is not uniform. Adaptations of CLARITY (*170-173*) increased the pore size and reduced the crosslinking of the hydrogel by removing the N,N'-methylene bisacrylamide component to facilitate better probe penetration. Another approach termed stochastic electrotransport uses electric fields to increase the diffusion of antibodies and dyes inside the tissue, enabling the labelling of whole

organs in 2-3 days (*174*). The expansion microscopy method uses sodium acrylate, a strong water-absorbent, to engineer the physiochemical properties of the polymer-gel for linear expansion. The tissue-gel hybrids (mouse brain slices) are fluorescently labelled with probes that bind the epitopes on the sample and are at the same time linked to the gel. After digestion of the biomolecules with proteinase, only the probes remain and the hydrogel can be isotopically expanded 4.5-fold for super-resolution imaging with a conventional confocal microscope (*175*). Another approach termed ePACT uses collagenase to disrupt the collagen matrix and SDS for delipidation of the samples, avoiding the complicated labelling and tissue digestion of expansion microscopy. Although distortion of cellular architecture can occur, this method allows for the expansion of mouse brain slices up to four-fold and visualization of transgenic Thy1-YFP signals (*176*). A similar method called MAP also eliminates the proteinase digestion step to preserve the proteome of intact tissue while still facilitating isotropic expansion (*177*). Further, MAP was the first expansion approach which was not limited to tissue slices enabling whole organ expansion. In MAP, a highly dense polymer network is created inside the tissue and, after denaturation with SDS, protein complexes are expanded isotopically for super-resolution imaging. To improve RNA detection 1-ethyl-3-(3-dimethylaminopropyl) carbodiimide chemistry can be used to anchor the RNAs to the hydrogel (*178*). However, MAP is not able to preserve transgenic fluorescence signals as tissue denaturation at high temperatures is required. Furthermore, imaging with subcellular resolution of whole organs could not be accomplished due to the lack of RI matching media that can maintain the tissue expansion, and the lack of suitable high-resolution objectives with WD that can cover an entire expanded organ such as a brain.

Another way to form a matrix is by using an epoxide. Such a method, called SHIELD, was specifically designed to preserve fluorescence, protein antigenicity, RNA, and tissue architecture, even under very harsh clearing conditions by using polyepoxy chemicals which form inter- and intramolecular crosslinks (*179*). The uniform distribution of cross-linkers is facilitated by employing the SWITCH method system.

Taken together, hydrogel-based methods preserve proteins and achieve high tissue transparency in the mouse brain. However, when applied to whole mouse body (PARS) (*170, 173*), bone tissue (Bone CLARITY) (*180*) or tumor tissue (*181*) the results are never as transparent as with organic solvent-based approaches (*85-87*) or hyperhydration based approaches (*142, 144*).

3.4 Light-sheet microscopy

In order to take full advantage of the clearing methods discussed above, microscopes that are capable of fast and high-resolution imaging of large volumes are needed. Some efforts focused on pushing the performance limits of well-established raster scanning approaches such as confocal- or two-photon microscopy. In a standard setup, scanning of an entire mouse brain with a volume of estimated 1000mm³ using a 20x objective with an assumed 500x500µm field of view and an axial step size of 1µm would require more than 4,200,000 images. At a fast scanning speed of 1 Hz this would take almost 50 days (*14*). To increase the acquisition speed of two-photon microscopy the use of a resonant scanning galvanometer, a piezoelectric motor-mounted objective for fast Z-scanning, and high laser excitation power, in combination with a vibratome for sectioning was designed (*145*). In this way, whole-brain imaging with high spatial resolution (0.45µm lateral and 1.33µm axial) in 7 days was achieved. However, the very long acquisition time for large samples represents a major limitation of raster scanning methods.

The rising need for fast throughput at high spatial resolution was addressed with light-sheet microscopy. The central idea behind light-sheet microscopy is that, through multiple different approaches, a laser beam is formed into a laser light-sheet which illuminates a transparent sample from the side. The illuminated plane is then recorded by a camera (CCD or CMOS sensor). In most applications the light-sheet generating unit is orientated at a 90° angle to the detecting objective. Compared with raster scanning microscopy, this approach offers two major advantages. First, the image acquisition rates are only limited by the recording speed of the camera, which can be several hundred million voxels with state-of-the-art detectors. Second, phototoxicity and photobleaching are reduced to a minimum, since only the focused detection plane is illuminated with the laser. In contrast, in confocal and two photon-microscopes the same objective is used for illumination and detection, thus the laser illuminates the regions below and above the focus plane during the entire recording time. As a result of this, light exposure in the imaging pathway increases linearly with sample size and can lead to complete bleaching of the fluorescent signal before the volume of interest is imaged. In 2007 Dodt and colleagues imaged the first cleared transgenic brain sample from a Thy1-GFP-M mouse brain with a light-sheet system they termed ultramicroscope (UM) (*59, 128*). This light-sheet was generated by a Gaussian-shaped laser beam passing through a rectangular slit aperture placed in front of a cylindrical lens (**Fig.13a**). By increasing the slit size, a very thin light-sheet could be generated. However, it diverges rapidly with distance from the focal point, it is therefore said to have a short Rayleigh range. The Rayleigh range is

the distance, along the propagation axis, between the beam waist and the point at which the beam thickness is equal to $\sqrt{2}$ times the value of the waist size (w_0) (*182*). A smaller slit aperture would increase this range, but the light-sheet would become thicker and a substantial amount of laser light would be lost (**Fig.13b**).
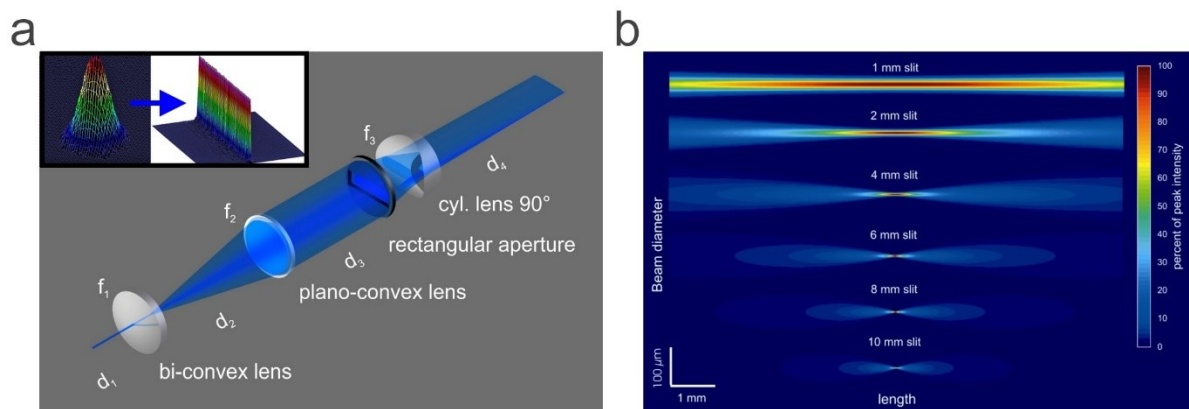

Figure 13: Principle of light-sheet generation with a slit aperture. (**a**) UM consisting of a beam expander, a slit aperture and a cylindrical lens. Inset shows transformation of Gaussian shaped laser beam into a light-sheet. (**b**) Correlation of slit aperture size with Rayleigh range and light-sheet thickness. Images adapted from doi: 10.1002/jbio.201000047 used with the permission of the publisher John Wiley and Sons. License ID 4841561217537

Various other Gaussian beam based custom- (*183-189*) and commercially available light-sheets like the LaVision BioTec UM (*23, 78, 85, 90, 99, 190, 191*) have been built and are used for large sample analysis. All these microscopes use similar optics and types of scanned (*192*) or static (*193*) light-sheets, achieving very similar results regarding imaging quality. Since image quality relies mainly on the light sheet - uniformity of power density, Rayleigh range and beam width – optimizing the light-sheet generating system is a crucial task. In the publication in **chapter 5** such an improved light-sheet generator is demonstrated. The presented light-sheet unit consists of a meso-aspheric element (i.e. Powell lens) which was placed between two aspheric lenses facing each other, producing an elliptical beam with a uniform intensity profile. This beam is further propagated through an elliptical anodizing soft-aperture and two identical acylidrical lenses (**Fig.14**). This way a thin light-sheet with a full width half maximum (FWHM) of 3µm and a Rayleigh range of 600µm could be generated (*22*). The light-sheet images from **chapters 5**, **6** and **8** were generated with such a system.
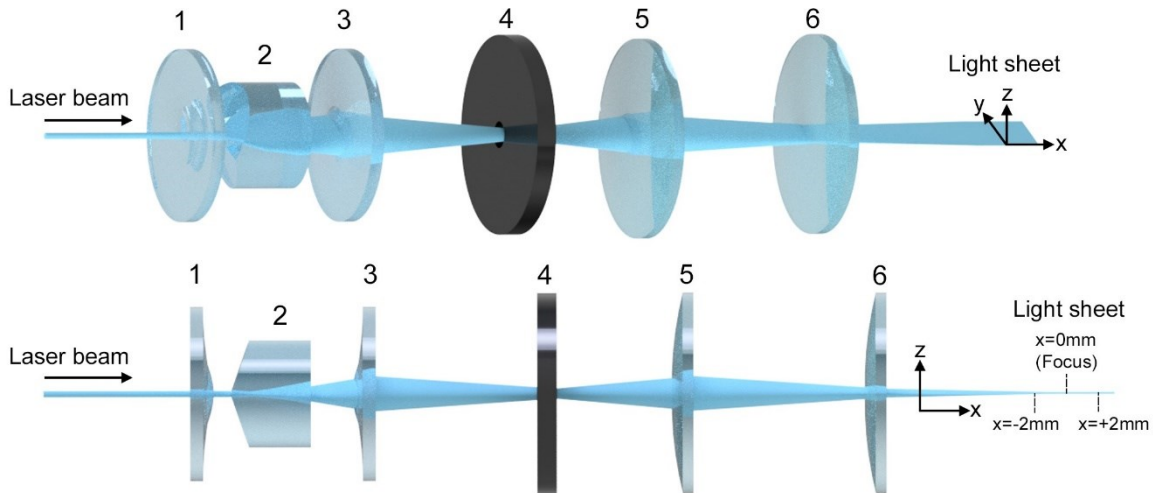
Figure 14: Characterisation of the aspheric ultramicroscope system. Illustration of the laser beam to light-sheet transformation achieved by an optical unit containing two plano-convex aspheric cylinder lenses (1, 3), a Powell lens (2), an elliptical soft-aperture (4) and two acylinder lenses (5, 6). Image adapted from DOI: 10.1038/s41467-018-07192-z

However, other light-sheet approaches designed for live-cell imaging like Bessel beams (*194*) or lattice light-sheet (*195*) can achieve, although with a short Rayleigh range, spatially isotropic resolution of a few hundred nanometers.

Light-sheet approaches using multi-view imaging were also able to achieve an isotropic resolution of 300-400nm (*196-198*). The idea behind this approach is that the sample is imaged from multiple directions. The imaged stacks are then combined, thereby removing the low resolving axial plane. Most commonly, two stacks are generated perpendicular to each other and the z-direction of each stack is replaced by the higher resolving lateral direction (**Fig.15**). In the research article in **chapter 5**, such an approach was used on cleared adult *D. melanogaster*. Although cleared tissue is very transparent, small differences in the RI within the specimen or outside the specimen and the RI medium remain. These differences deviate light in light-sheet illumination and fluorescence detection directions. Therefore, the multi-view combined pictures displayed in **chapter 5** are not perfectly aligned, causing some artefacts. Other, more sophisticated approaches, address this problem by adjusting the microscope to the optical properties of the samples. To facilitate optimal overlap between the different recordings, adaptive imaging using benchmark structures like the vasculature and autofocus techniques have been developed (*184, 199, 200*).
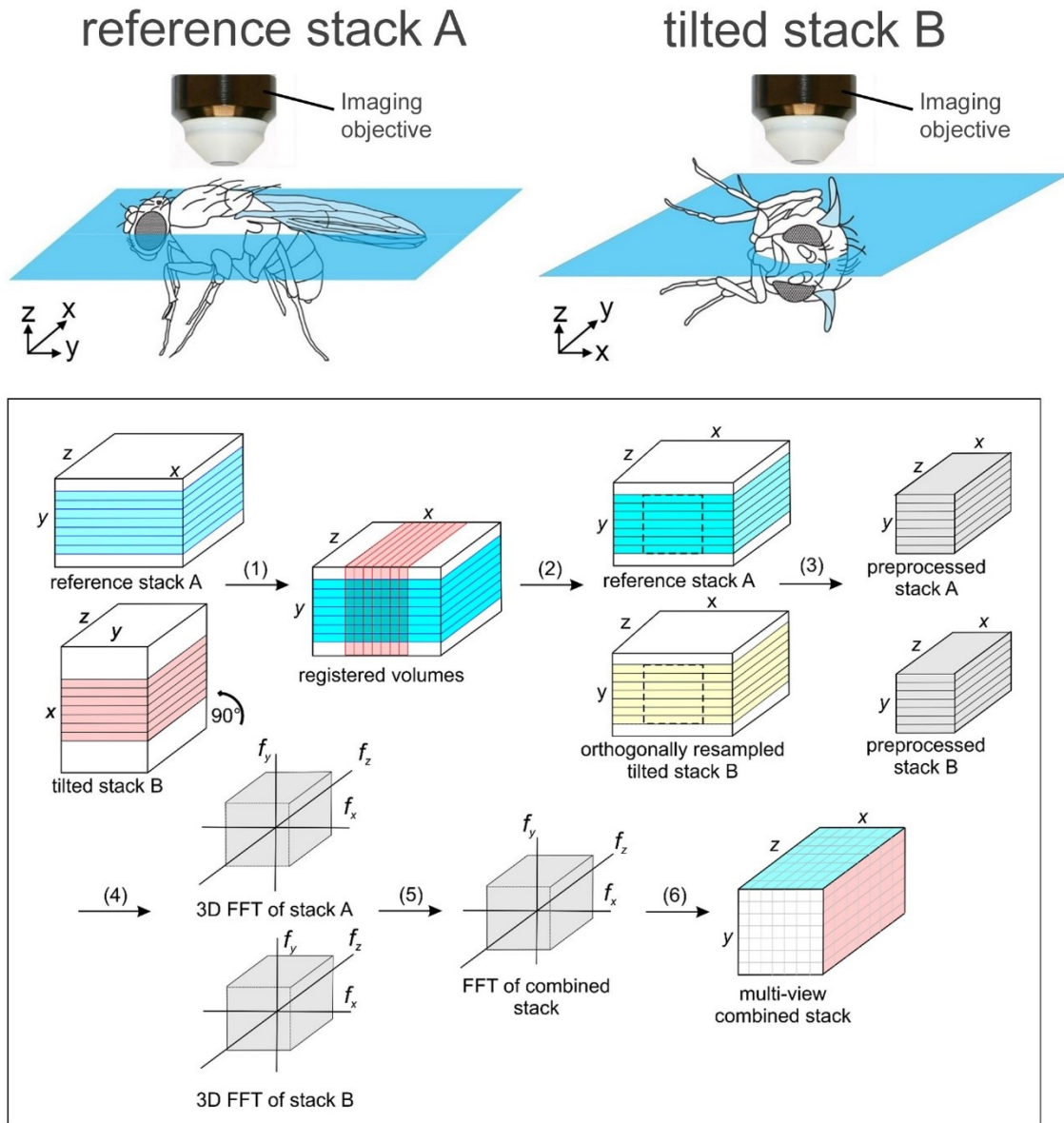
Figure 15: Principle of multi-view combining. (1) Two orthogonally recorded image stacks, A (reference stack) and B (tilted stack) are spatially registered. (2) After registration, stack B is virtually resliced to generate computed section planes that are coplanar with respect to stack A. (3) Non-overlapping regions are removed from stacks A and B by using a binary masking operation. The remaining parts are scaled to approximately the same average brightness. (4) A 3D Fast Fourier Transformation is applied to both stacks and the calculated magnitudes and phases are recombined. (5) The multi-view combined stack, comprising the sharper components of A and B, is further obtained by applying the inverse Fourier transformation. (6) Finished multi-view combined stack. Image adapted from DOI: 10.1038/s41467-018-07192-z

Nevertheless, imaging of large samples remains still very challenging, and improvements in light-sheet thickness and Rayleigh range are needed. Further, it is important to note that

immersion objectives are required for imaging of cleared tissue in the respective RI matching medium. When imaging very large samples in the range of millimeters or centimeters, the commercially available immersion objectives usually have a high resolution but a small field of view, resulting in specimen that cannot be imaged entirely without using tiling strategies and a substantial amount of data generation. Therefore, the development of multi immersion, large-field-of-view objectives with long working distances is required (discussed in the next section).

3.4.1 Objectives (WD, NA and RI correction)

The distance at which two closely spaced points are still resolvable by an objective is termed resolution and is defined by three main characteristics; the wavelength of light used to illuminate the sample, the angular aperture, and the RI in the object space between the objective front lens and the specimen.

The angular aperture of a lens defines the light gathering power of the objective (**Fig.16**). It gives a value for the largest angle of light, measured from the focus point (depicted as the sample in figure 16) passing through the lens and thus can have a theoretical maximum of 180°. It can be expressed through the angle α, which is one half of the angular aperture, and thus can have a maximum of 90°. Further, α can be calculated through the relationship between the diameter of the lens aperture D and the focal length f, and is given as following:

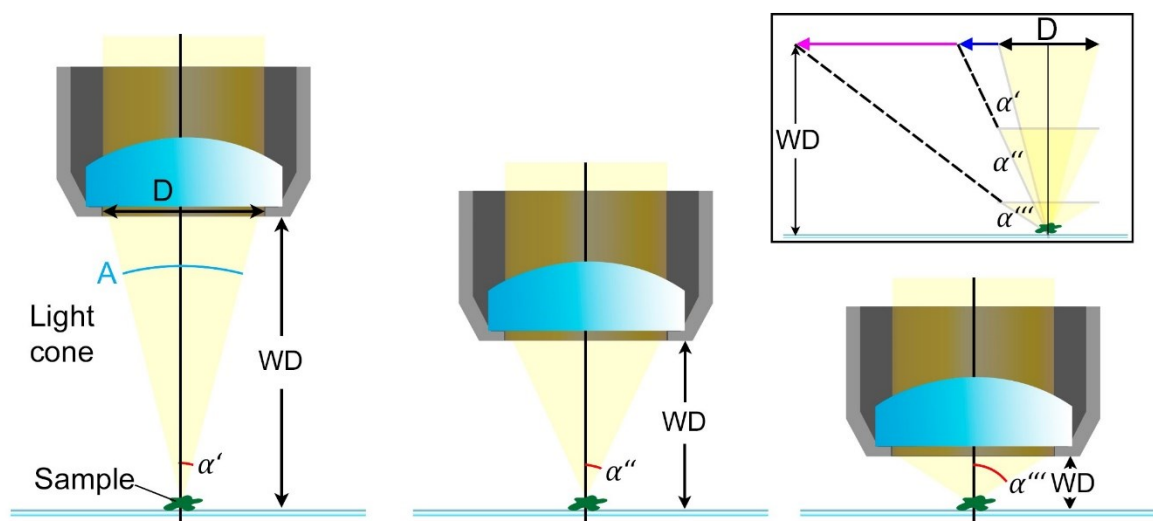$$\alpha = 2\arctan\left(\frac{D}{2f}\right) \qquad\qquad (Eq.40)$$

Figure 16: Relationship between objective parameters. Illustration of hypothetical objectives with

the same lens diameter aperture (D). From left to right: The increase in angular aperture (A) and the angle (α') to (α'') and (α''') is related to an increase of the NA and a decrease in working distance (WD). Dashed line in inset indicate the hypothetical required diameter aperture of a lens for (α'') and (α''') if the same WD is to be achieved as for (α').

The angle α is also related to the NA, which is, as mentioned above, an indicator of the resolving power of an objective and can be expressed as following

$$NA = n \times \sin\alpha \qquad \text{(Eq.41)}$$

where n is the RI (defined in Eq.18) of the medium.

The brightness of an image is not defined only by the NA as discussed above. Another factor defining the light sensitivity of an objective is the magnification F_{trans}

$$F_{trans} = 10^4 \cdot \frac{NA^2}{M} \qquad \text{(Eq.42)}$$

where M is the lateral magnification of the objective.

The most common media used for microscopy are air $n = 1$, water $n = 1.33$, glycerol $n = 1.45$ and oil $n = 1.52$. From (Eq.41) it is obvious that the NA increases with the RI. An air objective can have a theoretical maximum NA of 1.0 since $NA = 1 \times \sin 90° = 1$ while other high-performance objectives utilizing specialized immersion oils can have a NA of up to 1.6. However, in practice these theoretical values are very difficult to achieve as the maximum reachable NA for air is approximately 0.95 and for oil approximately 1.4. The NA is not solely dependent on the imaging medium but also on the quality of the objective and the amount of correction of optical (spherical and chromatic) aberration. This can be exemplified in a series of flat-field corrected plan 10x objectives from Olympus - plan achromat, NA = 0.25; plan fluorite, NA = 0.30; and plan apochromat, NA = 0.45.

As is apparent from **Fig. 16 inset**, in order to achieve a high WD and NA, the lens diameter aperture has to be adapted accordingly. In practice, the WD decreases as the magnification and the NA increase, especially in the case of immersion objectives. This is related to the standard way of sample mounting between a slide and a cover slip. A long WD objective would not be practical in such a case as the space between the coverslip and the objective front lens would need to be filled with a RI medium. If the WD is too large, the confluent network between the lens and the specimen would not be maintained, leading to unwanted light aberration with consequent image deterioration. Further, the design of long WD high NA objectives is extremely difficult as large lens diameters require high quality lenses and a substantial amount

of correction. Therefore, the general design of immersion objectives was focused on WD of up to 200µm. However, volumetric imaging of thick transparent samples requires high resolution images from deep tissue, leading to the development of immersion objectives such as the 25x Olympus, XLPlanN, 1.0 NA, with an 8mm WD, and the 20x Nikon, CFI90 20XC Glyc 1.0 NA with a WD of 8.2mm, both in the price range of 30k €. Low magnification objectives have usually a small NA but a large field of view. So far, due to missing applications, they are designed for usage in air. A severe problem for the imaging of large cleared samples is the lack of commercially available large field of view objectives, such as 2x or 4x, designed for imaging in solutions with high RI (1.45-1:56). In **Fig.17** and the publication in **chapter 2,** such RI corrected objectives designed by Dr. Saiedeh Saghafi are described. The images from the publications in **chapter 2-8** were partially or exclusively recorded with these objectives.
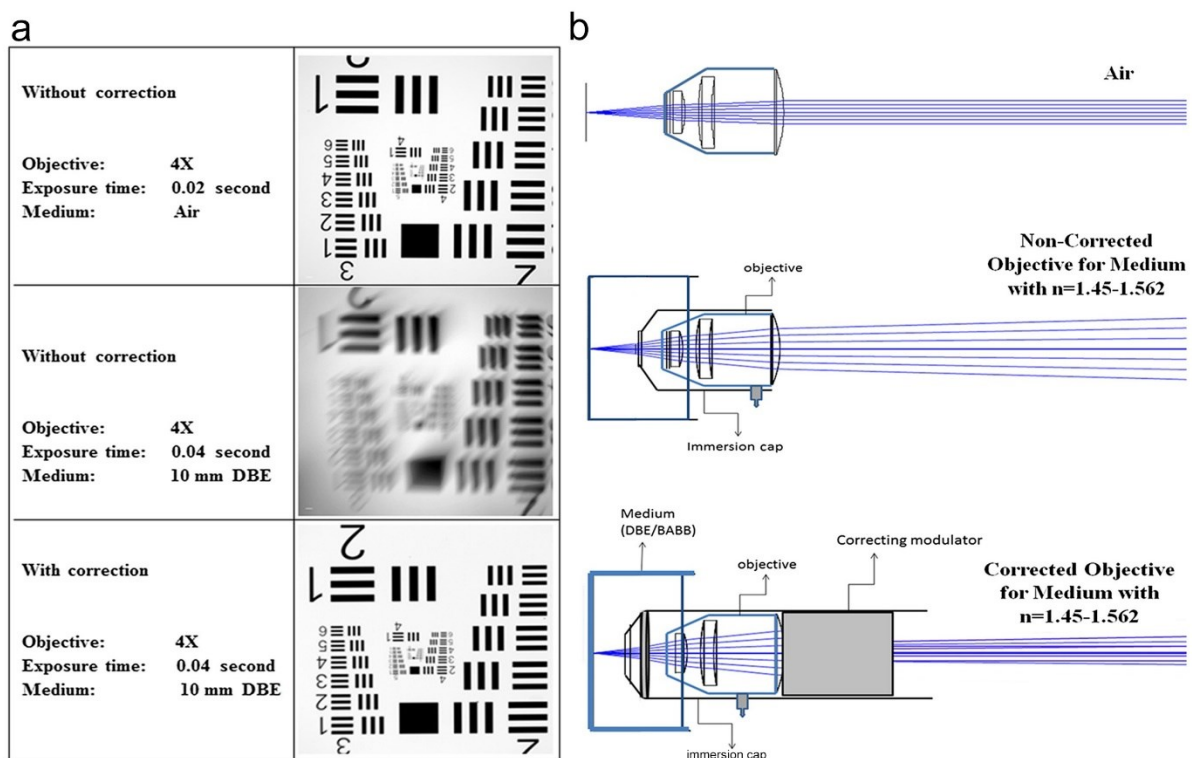
Figure 17: Correction of objectives for multiple RI imaging. (**a**) Images of an USAF 1951 chart in air (top) DBE without correction (middle) and DBE with correction (bottom). (**b**) Principle of the objectives correction. Left: Air objective focusing on sample in air. Middle: Shifted focus point through insertion of a correction optics for media with high RI in front of an air objective. Right: Water immersion objectives with correction optics for media with high RI behind the objective. Images are taken from doi: 10.1117/1.NPh.2.4.041407

The resolution of an objective, d_{min}, as already mentioned, is defined as the smallest distance at which two points of a sample can be distinguished as separate entities. The NA and the wavelength are the two determinates defining the resolving power, as postulated by the Rayleigh criterion.

$$d_{min} = \frac{0.61\lambda}{NA}$$

(Eq.43)

Two objects that are not further away than this distance cannot be resolved as two separate objects. As the NA of an objective has a maximum value (depending on the medium), the resolution, according to the Rayleigh criterion, is limited, also limiting the useful magnification factor. Objectives usually have a maximum magnification factor of 100. Everything beyond this factor would be magnified but not sufficiently resolved. This effect is called empty magnification.

Another important factor is the axial range through which an object can be moved without any detectable change in image sharpness, while the position of the image plane and objective are maintained. This is called the depth of field d_{depth} and is defined by wave optics and geometrical optical dominates. It can be calculated by the following equation

$$d_{depth} = \frac{\lambda n}{NA^2} + (\frac{n}{M \times NA})e$$

(Eq.44)

where e is the smallest distance that can be resolved by a detector, in the case of a camera this would be the pixel size.

As it is apparent from this equation, the field of depth is strongly affected by the NA. This is due to the fact that the diffraction-limited depth of the field shrinks inversely-proportional with the square of the NA. Therefore, small NA objectives have a very large field of depth, making it easy to find a focus point in a sample, but also a very low resolving power in the z-axis of a 3D stack.

As discussed previously (3.2.5), light is diffracted and scattered while traveling through a specimen, and further through the objective, causing small patterns on the image (**Fig.18a**). This so-called Airy pattern is broadened while it propagates, becoming larger than the emitting object itself and masking subtle details of it. The central maximum of these patterns is called the Airy disk and is defined as the region enclosed by the first minimum of the Airy pattern containing 84% of the light's energy (**Fig.18b**). This intensity of the light decreases from the central peak in concentric circles of 1st, 2nd, 3rd etc. order maxima representing a higher order of diffractions (**Fig.18a**). It is important to understand that only if an objective can capture these higher order diffractions an image can be created in the intermediate image plane of the

objective through interference effects. If only the central peaks or the central peak and first order light rays would be captured, the image would be very coherent but would lack a sufficient amount of detail, not being able to represent the true biological architecture. However, according to Rayleigh, two central peaks are only seen as separate if the distance between them is larger than the resolution limit (**Fig.18c**). If the minimum distance of two light peaks doesn't fulfil the Rayleigh criterion two objects are seen as one (**Fig.18d**).

The Airy disk pattern of concentric bright and dark rings in the x and y plane emitted from a point source, propagates in cone shape in axial direction above and below the center of this light source. This distortion of light can be described in a theoretical mathematical function called the point spread function (PSF), being a measure for the quality of an imaging system (**Fig.18e**).
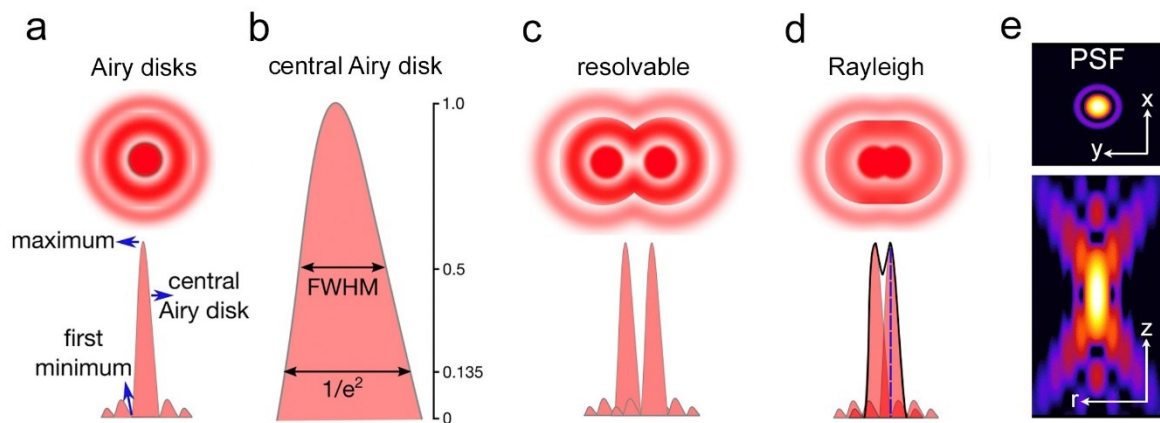
Figure 18: Illustration of Airy pattern and point spread function. (**a**) Description of hypothetical Airy disc. (**b**) Magnification of the central Airy disk giving additional ways to express the resolution by using the full width at half maximum (FWHM) or the width at 1/e of the point spread function (PSF). (**c**) Two Airy disks exceeding the Rayleigh criterion and being two resolvable points. (**d**) Two Airy disks where the center to center distance of the central disks is less than the width of their maxima. The points are not resolvable from one another according to the Rayleigh criterion. (**e**) Propagation of the Airy pattern in orthogonal (x and y) and axial z and r) direction from a point source of light - PSF. Image adapted from doi: 10.1088/1361-648X/aa7185 and doi: 10.1186/1475-925X-5-36

Objectives with higher correction and NA are able to produce smaller Airy disk projections, hence resolving more details from the recorded samples and thereby generating high-resolution images (**Fig.19**).

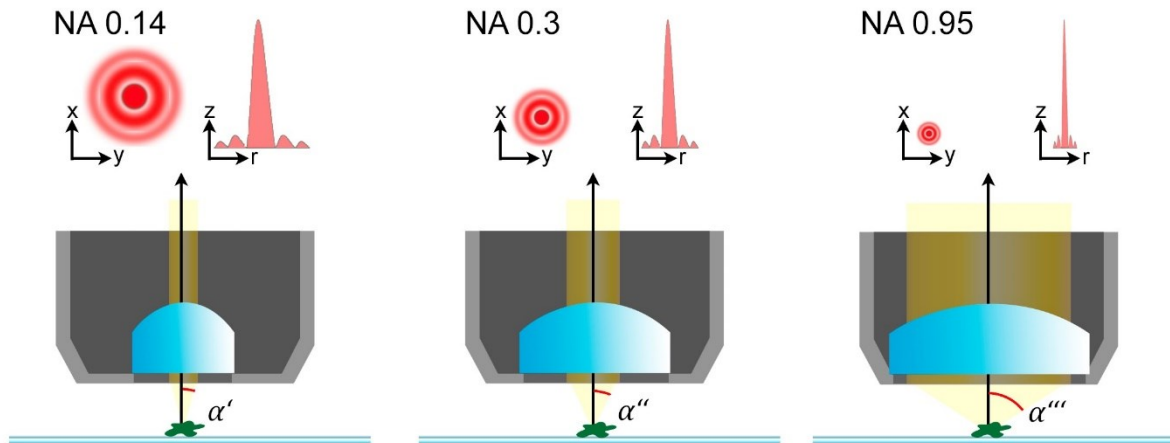**Figure 19: Correlation of NA and Airy disk size.** Illustration of hypothetical objectives with same focal length but different NA showing the decrease in Airy disk radii with increasing NA. Image adapted from doi: 10.1088/1361-648X/aa7185

3.5 Deconvolution

As discussed above, light microscopy provides a finite resolution and the light from a point source is deviated while propagating. Therefore, it becomes apparent that every picture generated with a light microscope is at best a very close approximation of the true nature of a specimen. Imaging systems vary in their quality of image generation and, as mentioned above, the PSF is a measure for this quality. By measuring the PSF with fluorescent beads, which have a standardized diameter of e.g. 100nm, 200nm or 500nm, the error of the system can be shown when comparing the original bead size to the realized picture. If the PSF can be accurately determined, the complementary function is computed, and the acquired images are convolved with that. Deconvolution approaches provide iterative algorithms for the correction of these light deviation errors, thereby restoring the original signal and improving the image quality. Some commercially available deconvolution software packages such as Huygens and Auto Quant, as well as some public domains like Deconvolution LAB2 (*201*), exist, making 3D deconvolution accessible for non-specialists.

Deconvolution is widely used with confocal and 2Pi microscopy. This is due to a couple of reasons. Both approaches need higher laser powers with increasing imaging depth, causing substantial out-of-focus background fluorescence, resulting in a lower SNR (*16, 202*). Further, both approaches have a generally low efficiency of light collection, especially confocal microscopy, which requires a pinhole that blocks most of the photons before they reach the

detector. Therefore, photon amplification is required. However, the photomultipliers used for this purpose are very sensitive and are known to cause background noise. This is also the reason why objectives with high NA (<0,5) are used in confocal and two-photon microscopy, since large-field-of-view, low magnification objectives have a high capability for collecting scattering photons which would increase background noise even further during image acquisition (*203, 204*).

The general drawback of deconvolution is the amplification of background noise, therefore, low magnification objectives are avoided in combination with raster scanning microscopy. In contrast, light-sheet microscopes detect fluorescent light an order of magnitude more efficiently than the aforementioned methods, allowing the use of standard CCD or CMOS cameras. Therefore, images are generated with very low background and excellent axial resolution. This allows the use of low magnification objectives and high field numbers (FN22) for deep tissue and large sample interrogation. Although commercially available add-on modules from Huygens and Auto Quant for light-sheet image deconvolution exist, they perform badly with low NA light-sheet image data and the results sometimes look worse than the initial pictures. The reason for this is that accurate PSF measurements, that are resolved enough to be applicable for deconvolution, are very difficult to acquire through recordings of fluorescent beads. This is mainly related to the resolution limits of the used microscope cameras. According to the Rayleigh criterion (Eq.43) and the Nyquist's theorem (Eq.45), the camera sampling frequency should be up to three times higher of the highest spatial frequency resolved in the image.

The resolution (in megapixels) of a detector required to make full use of an objective can be calculated according to the Rayleigh criterion.

$$\frac{2s_{x,y}}{V \cdot n_{x,y}} = \frac{0.61\lambda}{NA}, P = n_x n_y \approx 10.75 \cdot s_x s_y \left(\frac{NA}{V\lambda}\right)^2 \qquad \text{(Eq.45)}$$

P is the required number of megapixels, V is the total magnification of the microscope, $n_x n_y$ is the number of pixels in x and y direction and $s_x s_y$ is the camera chip size in the x and y directions.

When using a 4x NA 0.28 objective and assuming a standard chip size of 15 x 15mm², according to Nyquist's theorem (Eq.45), a camera resolution of at least 50 megapixels would be required to resolve the acquired image. However, such cameras do not currently exist for microscopy. Therefore, beads in the range of 100-250nm used as standard are very poorly resolved with such objectives. These images have a restricted lateral resolution of the measured PSF caused by an insufficient number of pixels, making the measurement not

suitable for deconvolution (*202*). Further factors abstracting the PSF are scattering effects introduced by the imaging medium (especially high viscous liquids), and the RI mismatch between the fluorescent beads and the embedding medium (*205*). Although, there are some workarounds to these problems the overall acquisition of an accurate PSF is quite difficult. An alternative to PSF measurement was developed by Boniface *et al*. (*205*), this proposes a theoretically calculated PSF in a complex light scattering medium. An approach deriving a computed PSF from an optical model of image formation in a light sheet microscope was developed by Dr. Klaus Becker and the resulting publication is presented in **chapter 8**. Further, the light-sheet images in **chapter 7** are all processed with this theoretical PSF.

Chapter 2 – Ultramicroscopy: development and outlook

Authors: Hans-Ulrich Dodt*, Saiedeh Saghafi, Klaus Becker, Nina Jährling, Christian Hahn, Marko Pende, Martina Wanis, Axel Niendorf

*Correspondence

Detailed description of the contribution of Marko Pende:

a. Performed the CLARITY method on Thy1-EGFP-M mice
b. Performed light-sheet imaging and computer processing of the images in depicted figure 6 and 7
c. Prepared figure 6 and 7
d. Wrote parts of the manuscript, edited and approved the manuscript

Chapter 3 – Outlook on optimizing ultramicroscopy imaging technique through optical characterization

Authors: Saiedeh Saghafi*, Klaus Becker, Christian Hahn, Marko Pende, Nina Jährling, Martina Wanis, Inna Sabdyusheva-Litschauer, Massih Foroughipour, Axel Niendorf, Hans-Ulrich Dodt

*Correspondence

Detailed description of the contribution of Marko Pende:

   a. Performed the 3DISCO method on Fruit Flies
   b. Performed light-sheet imaging and computer processing of the images in figure 2 and parts of figure 6
   c. Wrote parts of the manuscript, edited and approved the manuscript

Chapter 4 – Reshaping a multimode laser beam into a constructed Gaussian beam for generating a thin light sheet

Authors: Saiedeh Saghafi*, Nikoo Haghi-Danaloo1, Klaus Becker, Inna Sabdyusheva, Massih Foroughipour, Christian Hahn, Marko Pende, Martina Wanis, Michael Bergmann, Judith Stift, Balazs Hegedus, Balazs Dome, Hans-Ulrich Dodt

Detailed description of the contribution of Marko Pende:

a. Performed the 3DISCO method on Fruit Flies
b. Performed light-sheet imaging and computer processing of the images in figure 2 and parts of figure 6
c. Wrote parts of the manuscript, edited and approved the manuscript

Chapter 5 – High-resolution ultramicroscopy of the developing and adult nervous system in optically cleared Drosophila melanogaster

Authors: Marko Pende*[+], Klaus Becker[+], Martina Wanis, Saiedeh Saghafi, Rashmit Kaur, Christian Hahn, Nika Pende, Massih Foroughipour, Thomas Hummel & Hans-Ulrich Dodt*

*Correspondence

+ These authors contributed as equals

Detailed description of the contribution of Marko Pende:

a. Designed the study
b. Developed the FlyClear method
c. Performed most of the experiments
d. Prepared all the figures
e. Wrote majority of the manuscript
f. Edited and approved the manuscript

Chapter 6 – High-resolution imaging of fluorescent whole mouse brains using stabilised organic media (sDISCO)

Authors: Christian Hahn*, Klaus Becker, Saiedeh Saghafi, Marko Pende, Alma Avdibašić, Massih Foroughipour, Daniel E. Heinz, Carsten T. Wotjak, Hans-Ulrich Dodt*

*Correspondence

Detailed description of the contribution of Marko Pende:

a. Partially established the sDISCO method
b. Partially participated with the super-resolution recordings
c. Performed the revision of the manuscript-comparison of differen clearing methods and statistical evaluation
d. Helped with the preparation of the figures
e. Edited and approved the manuscript

Chapter 7 – Deconvolution of light sheet microscopy recordings

Authors: Klaus Becker*, Saiedeh Saghafi, Marko Pende, Inna Sabdyusheva-Litschauer, Christian M. Hahn, Massih Foroughipour, Nina Jährling & Hans-Ulrich Dodt

*Correspondence

Detailed description of the contribution of Marko Pende:

    a. Tested and helped with the usability of the deconvolutions program
    b. Performed light-sheet imaging of FlyClear process adult *D.melanogaster*
    c. Contributed to figure 3a
    d. Edited and approved the manuscript

Chapter 8 – A versatile depigmentation, clearing and labelling method for exploring nervous system diversity

Authors: Marko Pende*+, Karim Vadiwala+, Hannah Schmidbaur, Alexander Stockinger, Prayag Murawala, Saiedeh Saghafi, Marcus P.S. Dekens, Klaus Becker, Roger Revilla-i-Domingo, Sofia-Christina Papadopoulos, Martin Zurl, Pawel Pasierbek, Oleg Simakov, Elly M. Tanaka, Florian Raible*, and Hans-Ulrich Dodt

*Correspondence

+ These authors contributed as equals

Detailed description of the contribution of Marko Pende:

    a. Designed parts of the study
    b. Developed the DEEP-Clear method
    c. Performed the light-sheet imaging and parts of the confocal imaging
    d. Prepared all the figures
    e. Wrote parts of the manuscript
    f. Edited and approved the manuscript

Chapter 9 – Conclusion and outlook

Studies using tissue clearing have already deepened our understanding of various basic biological processes and improved the analysis of 3D pathology. The need for large system interrogation tools further stimulated the advancement of other techniques such as light-sheet microscopy, microscope objective design, and computational image processing programs such as multi-view approaches or applications of different deconvolution algorithms.

Since the modern introduction of tissue clearing, the number of methods has increased rapidly and the efficacy regarding tissue transparency, signal stability, and compatibility with molecular tools has improved considerably. However, there is still a gap in the understanding of the underlying chemical and physical principles involved in clearing processes. For example, the concept of RI matching does not fully explain the theory of light scattering. It was demonstrated that cryopreserved human skin treated with clearing chemicals such as organic solvents and organic acids show no correlation between RI and optical clearing potential (*206*). Another study showed that the clearing ability of alcohols is rather related to the number of hydroxyl groups than to the RI (*207*). Further, RI matching with inorganic ions, such as in a zinc iodide solution, had despite the high RI and liquid homogeneity, insufficient clearing properties in brain tissue (*133*). Possible explanations for these discrepancies between the concept of RI matching and the aforementioned observations can be the change in structure and size of scattering molecules during tissue clearing. Sugars and sugar alcohols for example, which are part of many clearing protocols, destabilize and dissociate collagen structures leading to tissue transparency. Further, after dehydration, the tissue components are more dense, leading to a more ordered structure and a decrease of particle size, which can reduce light scattering (*208-211*). This is also supported by a theoretical study concluding that light scattering is, in addition to the RI, dependent on the shape and size of particles (*212*).

Other aspects of tissue clearing, such as the challenge of pigment removal, were already successfully addressed by the CUBIC, FlyClear and DEEP-Clear approaches. However, a chemical treatment removing melanin without a peroxide bleaching step is needed to improve the compatibility with transgenic fluorescent reporter lines (*22, 23, 81*).

Further, fast and uniform labelling approaches for large cleared tissue samples are needed. Methods like SWITCH (*169*), ACT-PRESTO (*213*) or stochastic electrotransport (*174*) improved the labelling speed, however these methods are rather difficult to implement. An interesting approach was recently published by Susaki *et al*. 2020 defining the parameters for optimum probe penetration (*142*). However, the validity and applicability of this study still has to be evaluated by other groups. In addition, more robust labelling methods are needed

allowing for a variety of biomolecules to be labelled. The DEEP-Clear method presented herein, (*81*) and some other approaches (*80, 178, 179*), already made a step in the right direction regarding compatibility of molecular labelling tools for easily degraded biomolecules like RNA, or very small molecules like dopamine. However, high transparency in combination with the labeling of membranes is so far very challenging due to the necessity of removing lipids.

Another, major challenge is the use of tissue clearing in live samples, since clearing methods rely on very harsh mounting conditions and/or toxic chemicals (**Table 1**). So far there has been just one study *in vivo*, using the water tunable RI matching chemical Iodixanol (*214*). This study reported applications in cell culture, planarians, zebrafish and human cerebral organoids, thereby significantly improving the image quality. However, it is important to stress that the RI within the samples was not changed, meaning that opaque living animals cannot be rendered transparent so far.

In conclusion, although there are a lot of methods showing high tissue transparency, a deeper understanding of the principles underlying tissue clearing is needed to fully comprehend all the previously reported empirical observations. With such knowledge the optimal clearing strategy can be found for multiple tissues, if the composition of the biological content is known, thus providing researchers with a tailored analysis tool. In this way tissue clearing would not be restricted to a handful of well-established model organisms or human tissue, allowing for analysis of samples directly from nature. Thereby, important morphological and developmental questions could be addressed in entire organisms, even at later stages of life, from a multitude of different species of animals and plants. In combination with other methods, such as single-cell RNA sequencing and mass spectroscopy, spatial and temporal information on the quantity and quality of RNA and proteins throughout whole organs or organisms could be obtained, giving insight into global system regulation. With further advancements in microscopy and image post-processing strategies, tissue clearing can significantly scale up our understanding of the processes of life.

References

1. H. Hillman, Limitations of clinical and biological histology. *Medical Hypotheses* **54**, 553-564 (2000).
2. S. A. Taqi, S. A. Sami, L. B. Sami, S. A. Zaki, A review of artifacts in histopathology. *J Oral Maxillofac Pathol* **22**, 279-279 (2018).
3. V. Rastogi *et al.*, Artefacts: a diagnostic dilemma - a review. *J Clin Diagn Res* **7**, 2408-2413 (2013).
4. A. W. Toga, K. L. Ambach, S. Schluender, High-Resolution Anatomy from in Situ Human Brain. *NeuroImage* **1**, 334-344 (1994).
5. W. Denk, H. Horstmann, Serial Block-Face Scanning Electron Microscopy to Reconstruct Three-Dimensional Tissue Nanostructure. *PLoS biology* **2**, e329 (2004).
6. K. Ichimura *et al.*, Three-dimensional architecture of podocytes revealed by block-face scanning electron microscopy. *Sci Rep* **5**, 8993 (2015).
7. D. Mayerich, L. Abbott, B. McCormick, Knife-edge scanning microscopy for imaging and reconstruction of three-dimensional anatomical structures of the mouse brain. *Journal of microscopy* **231**, 134-143 (2008).
8. H. Xiong *et al.*, Chemical reactivation of quenched fluorescent protein molecules enables resin-embedded fluorescence microimaging. *Nature communications* **5**, 3992 (2014).
9. M. Minsky, Memoir on inventing the confocal scanning microscope. *Scanning* **10**, 128-138 (1988).
10. J. A. Conchello, J. W. Lichtman, Optical sectioning microscopy. *Nature methods* **2**, 920-931 (2005).
11. J. Mertz, Optical sectioning microscopy with planar or structured illumination. *Nature methods* **8**, 811-819 (2011).
12. D. M. SHOTTON, Confocal scanning optical microscopy and its applications for biological specimens. *Journal of Cell Science* **94**, 175-206 (1989).
13. J. W. Lichtman, J. A. Conchello, Fluorescence microscopy. *Nature methods* **2**, 910-919 (2005).
14. D. S. Richardson, J. W. Lichtman, Clarifying Tissue Clearing. *Cell* **162**, 246-257 (2015).
15. P. Theer, M. T. Hasan, W. Denk, Two-photon imaging to a depth of 1000 microm in living brains by use of a Ti:Al2O3 regenerative amplifier. *Optics letters* **28**, 1022-1024 (2003).
16. P. Theer, W. Denk, On the fundamental imaging-depth limit in two-photon microscopy. *Journal of the Optical Society of America. A, Optics, image science, and vision* **23**, 3139-3149 (2006).
17. T. Ragan *et al.*, Serial two-photon tomography for automated ex vivo mouse brain imaging. *Nature methods* **9**, 255-258 (2012).
18. S. W. Oh *et al.*, A mesoscale connectome of the mouse brain. *Nature* **508**, 207-214 (2014).
19. T. Isosaka *et al.*, Htr2a-Expressing Cells in the Central Amygdala Control the Hierarchy between Innate and Learned Fear. *Cell* **163**, 1153-1164 (2015).
20. B. Clancy, L. J. Cauller, Reduction of background autofluorescence in brain sections following immersion in sodium borohydride. *Journal of neuroscience methods* **83**, 97-102 (1998).
21. H. Duong, M. Han, A multispectral LED array for the reduction of background autofluorescence in brain tissue. *Journal of neuroscience methods* **220**, 46-54 (2013).
22. M. Pende *et al.*, High-resolution ultramicroscopy of the developing and adult nervous system in optically cleared Drosophila melanogaster. *Nature communications* **9**, 4731 (2018).
23. E. A. Susaki *et al.*, Whole-brain imaging with single-cell resolution using chemical cocktails and computational analysis. *Cell* **157**, 726-739 (2014).

24. K. Tainaka *et al.*, Chemical Landscape for Tissue Clearing Based on Hydrophilic Reagents. *Cell reports* **24**, 2196-2210.e2199 (2018).

25. A. Konno, S. Okazaki, Aqueous-based tissue clearing in crustaceans. *Zoological letters* **4**, 13 (2018).

26. Y. Henning, C. Osadnik, E. P. Malkemper, EyeCi: Optical clearing and imaging of immunolabeled mouse eyes using light-sheet fluorescence microscopy. *Experimental eye research* **180**, 137-145 (2019).

27. A. A. Alnuami, B. Zeedi, S. M. Qadri, S. S. Ashraf, Oxyradical-induced GFP damage and loss of fluorescence. *International Journal of Biological Macromolecules* **43**, 182-186 (2008).

28. H. Steinke, W. Wolff, A modified Spalteholz technique with preservation of the histology. *Annals of Anatomy - Anatomischer Anzeiger* **183**, 91-95 (2001).

29. T. H. Morgan, SEX LIMITED INHERITANCE IN DROSOPHILA. *Science (New York, N.Y.)* **32**, 120-122 (1910).

30. J. A. Lister, C. P. Robertson, T. Lepage, S. L. Johnson, D. W. Raible, nacre encodes a zebrafish microphthalmia-related protein that regulates neural-crest-derived pigment cell fate. *Development (Cambridge, England)* **126**, 3757-3767 (1999).

31. G. Streisinger, C. Walker, N. Dower, D. Knauber, F. Singer, Production of clones of homozygous diploid zebra fish (Brachydanio rerio). *Nature* **291**, 293-296 (1981).

32. Z. Li *et al.*, Phenylthiourea specifically reduces zebrafish eye size. *PloS one* **7**, e40132 (2012).

33. J. R. Stowers *et al.*, Virtual reality for freely moving animals. *Nature methods* **14**, 995-1002 (2017).

34. P. Antinucci, R. Hindges, A crystal-clear zebrafish for in vivo imaging. *Sci Rep* **6**, 29490 (2016).

35. R. M. White *et al.*, Transparent adult zebrafish as a tool for in vivo transplantation analysis. *Cell stem cell* **2**, 183-189 (2008).

36. J. Karlsson, J. von Hofsten, P. E. Olsson, Generating transparent zebrafish: a refined method to improve detection of gene expression during embryonic development. *Marine biotechnology (New York, N.Y.)* **3**, 522-527 (2001).

37. A. B. Lerner, T. B. Fitzpatrick, Biochemistry of melanin formation. *Physiological reviews* **30**, 91-126 (1950).

38. J. R. Whittaker, An analysis of melanogenesis in differentiating pigment cells of ascidian embryos. *Developmental biology* **14**, 1-39 (1966).

39. Y. Higashi, M. Asanuma, I. Miyazaki, N. Ogawa, Inhibition of tyrosinase reduces cell viability in catecholaminergic neuronal cells. *Journal of neurochemistry* **75**, 1771-1774 (2000).

40. F. Leblond, S. C. Davis, P. A. Valdes, B. W. Pogue, Pre-clinical whole-body fluorescence imaging: Review of instruments, methods and applications. *Journal of photochemistry and photobiology. B, Biology* **98**, 77-94 (2010).

41. S. Ogawa, T. M. Lee, A. S. Nayak, P. Glynn, Oxygenation-sensitive contrast in magnetic resonance image of rodent brain at high magnetic fields. *Magnetic resonance in medicine* **14**, 68-78 (1990).

42. M. L. Bouxsein *et al.*, Guidelines for assessment of bone microstructure in rodents using micro-computed tomography. *Journal of bone and mineral research : the official journal of the American Society for Bone and Mineral Research* **25**, 1468-1486 (2010).

43. H. Mizutani, Y. Takeda, A. Momose, A. Takeuchi, T. Takagi, X-ray microscopy for neural circuit reconstruction. *Journal of Physics: Conference Series* **186**, 012092 (2009).

44. K. Tainaka, A. Kuno, S. I. Kubota, T. Murakami, H. R. Ueda, Chemical Principles in Tissue Clearing and Staining Protocols for Whole-Body Cell Profiling. *Annual review of cell and developmental biology* **32**, 713-741 (2016).

45. J. W. Lichtman, W. Denk, The big and the small: challenges of imaging the brain's circuits. *Science (New York, N.Y.)* **334**, 618-623 (2011).

46. E. A. Bushong *et al.*, X-ray microscopy as an approach to increasing accuracy and efficiency of serial block-face imaging for correlated light and electron microscopy of biological

specimens. *Microscopy and microanalysis : the official journal of Microscopy Society of America, Microbeam Analysis Society, Microscopical Society of Canada* **21**, 231-238 (2015).

47. J. Ng *et al.*, Genetically targeted 3D visualisation of Drosophila neurons under Electron Microscopy and X-Ray Microscopy using miniSOG. *Sci Rep* **6**, 38863 (2016).

48. X. Shu *et al.*, A genetically encoded tag for correlated light and electron microscopy of intact cells, tissues, and organisms. *PLoS biology* **9**, e1001041 (2011).

49. R. J. Watts, O. Schuldiner, J. Perrino, C. Larsen, L. Luo, Glia engulf degenerating axons during developmental axon pruning. *Current biology : CB* **14**, 678-684 (2004).

50. J. Li, Y. Wang, S. L. Chiu, H. T. Cline, Membrane targeted horseradish peroxidase as a marker for correlative fluorescence and electron microscopy studies. *Frontiers in neural circuits* **4**, 6 (2010).

51. D. Atasoy *et al.*, A genetically specified connectomics approach applied to long-range feeding regulatory circuits. *Nature neuroscience* **17**, 1830-1839 (2014).

52. V. Liss, B. Barlag, M. Nietschke, M. Hensel, Self-labelling enzymes as universal tags for fluorescence microscopy, super-resolution microscopy and electron microscopy. *Sci Rep* **5**, 17740 (2015).

53. D. Boassa *et al.*, Mapping the subcellular distribution of alpha-synuclein in neurons using genetically encoded probes for correlated light and electron microscopy: implications for Parkinson's disease pathogenesis. *The Journal of neuroscience : the official journal of the Society for Neuroscience* **33**, 2605-2615 (2013).

54. Y. Hwu, G. Margaritondo, A. S. Chiang, Q&A: Why use synchrotron x-ray tomography for multi-scale connectome mapping? *BMC biology* **15**, 122 (2017).

55. M. d. C. Fonseca *et al.*, High-resolution synchrotron-based X-ray microtomography as a tool to unveil the three-dimensional neuronal architecture of the brain. *Scientific Reports* **8**, 12074 (2018).

56. R. Cicchi, F. S. Pavone, D. Massi, D. D. Sampson, Contrast and depth enhancement in two-photon microscopy of human skin ex vivo by use of optical clearing agents. *Optics express* **13**, 2337-2344 (2005).

57. G. Vargas, K. F. Chan, S. L. Thomsen, A. J. Welch, Use of osmotically active agents to alter optical properties of tissue: Effects on the detected fluorescence signal measured through skin. *Lasers in Surgery and Medicine* **29**, 213-220 (2001).

58. V. Ntziachristos, Going deeper than microscopy: the optical imaging frontier in biology. *Nature methods* **7**, 603-614 (2010).

59. H. U. Dodt *et al.*, Ultramicroscopy: three-dimensional visualization of neuronal networks in the whole mouse brain. *Nature methods* **4**, 331-336 (2007).

60. G. A. Reider, *Photonics: An Introduction*. (Springer, 2013).

61. E. Hecht, *Optics, Fourth Edition*. (Addison-Wesley, 2001).

62. V. V. Tuchin, Laser light scattering in biomedical diagnostics and therapy. *Journal of laser applications* **5**, 43-60 (1993).

63. V. V. Tuchin, Light scattering study of tissues. *Physics-Uspekhi* **40**, 495-515 (1997).

64. J. Dillon, The photophysics and photobiology of the eye. *Journal of photochemistry and photobiology. B, Biology* **10**, 23-40 (1991).

65. R. R. Anderson, J. A. Parrish, in *The Science of Photomedicine,* J. D. Regan, J. A. Parrish, Eds. (Springer US, Boston, MA, 1982), pp. 147-194.

66. A. N. Bashkatov, E. A. Genina, V. V. Tuchin, OPTICAL PROPERTIES OF SKIN, SUBCUTANEOUS, AND MUSCLE TISSUES: A REVIEW. *Journal of Innovative Optical Health Sciences* **04**, 9-38 (2011).

67. R. Alfano, A. Doukas, Introduction to the special issue on lasers in biology and medicine. *IEEE Journal of Quantum Electronics* **20**, 1342-1342 (1984).

68. T. B. Smith, Multiple Scattering in the Cornea. *Journal of Modern Optics* **35**, 93-101 (1988).

69. D. E. Freund, R. L. McCally, R. A. Farrell, Effects of fibril orientations on light scattering in the cornea. *Journal of the Optical Society of America. A, Optics and image science* **3**, 1970-1982 (1986).

70. V. V. Tuchin, Tissue Optics and Photonics: Biological Tissue Structures. *Journal of Biomedical Photonics & Engineering; Vol 1, No 1 (2015)DO - 10.18287/jbpe-2015-1-1-3*, (2015).

71. L. E. Preuss, A. E. Profio, Optical properties of mammalian tissue: introduction by the feature editors. *Appl. Opt.* **28**, 2207-2209 (1989).

72. R. A. Farrell, Freund, David E.,McCally, Russell L., Research on corneal structure. *Johns Hopkins APL Technical Digest (Applied Physics Laboratory)* **Vol. 11**, p. 191-119 (1990/1/1).

73. R. A. Farrell, D. E. Freund, R. L. McCally, Hierarchical Structure and Light Scattering in the Cornea. *MRS Proceedings* **255**, 233 (2011).

74. I. L. Maksimova, S. V. Romanov, V. F. Izotova, The effect of multiple scattering in disperse media on polarization characteristics of scattered light. *Optics and Spectroscopy* **92**, 915-923 (2002).

75. W. Spalteholz, *Über das Durchsichtigmachen von menschlichen und tierischen Präparaten und seine theoretischen Bedingungen, nebst Anhang: Über Knochenfärbung*. (S. Hirzel, Leipzig, 1914).

76. A. H. Voie, D. H. Burns, F. A. Spelman, Orthogonal-plane fluorescence optical sectioning: three-dimensional imaging of macroscopic biological specimens. *Journal of microscopy* **170**, 229-236 (1993).

77. K. Becker, N. Jahrling, S. Saghafi, R. Weiler, H. U. Dodt, Chemical clearing and dehydration of GFP expressing mouse brains. *PloS one* **7**, e33916 (2012).

78. A. Erturk *et al.*, Three-dimensional imaging of solvent-cleared organs using 3DISCO. *Nature protocols* **7**, 1983-1995 (2012).

79. H. Hama *et al.*, Scale: a chemical approach for fluorescence imaging and reconstruction of transparent mouse brain. *Nature neuroscience* **14**, 1481-1488 (2011).

80. K. Chung *et al.*, Structural and molecular interrogation of intact biological systems. *Nature* **497**, 332-337 (2013).

81. M. Pende *et al.*, A versatile depigmentation, clearing, and labeling method for exploring nervous system diversity. *Science Advances* **6**, eaba0365 (2020).

82. N. Renier *et al.*, iDISCO: a simple, rapid method to immunolabel large tissue samples for volume imaging. *Cell* **159**, 896-910 (2014).

83. M. K. Schwarz *et al.*, Fluorescent-Protein Stabilization and High-Resolution Imaging of Cleared, Intact Mouse Brains. *PloS one* **10**, e0124650 (2015).

84. C. Hahn *et al.*, High-resolution imaging of fluorescent whole mouse brains using stabilised organic media (sDISCO). *Journal of biophotonics* **12**, e201800368 (2019).

85. C. Pan *et al.*, Shrinkage-mediated imaging of entire organs and organisms using uDISCO. *Nature methods* **13**, 859-867 (2016).

86. D. Jing *et al.*, Tissue clearing of both hard and soft tissue organs with the PEGASOS method. *Cell research* **28**, 803-818 (2018).

87. R. Cai *et al.*, Panoptic imaging of transparent mice reveals whole-body neuronal projections and skull–meninges connections. *Nature neuroscience* **22**, 317-327 (2019).

88. Y. Qi *et al.*, FDISCO: Advanced solvent-based clearing method for imaging whole organs. *Science Advances* **5**, eaau8355 (2019).

89. S. Zhao *et al.*, Cellular and Molecular Probing of Intact Human Organs. *Cell* **180**, 796-812.e719 (2020).

90. M. Belle *et al.*, A simple method for 3D analysis of immunolabeled axonal tracts in a transparent nervous system. *Cell reports* **9**, 1191-1201 (2014).

91. N. Renier *et al.*, Mapping of Brain Activity by Automated Volume Analysis of Immediate Early Genes. *Cell* **165**, 1789-1802 (2016).

92. A. Klingberg *et al.*, Fully Automated Evaluation of Total Glomerular Number and Capillary Tuft Size in Nephritic Kidneys Using Lightsheet Microscopy. *Journal of the American Society of Nephrology : JASN* **28**, 452-459 (2017).

93. W. Masselink *et al.*, Broad applicability of a streamlined ethyl cinnamate-based clearing procedure. *Development (Cambridge, England)* **146**, (2019).

94. E. A. Susaki, H. R. Ueda, Whole-body and Whole-Organ Clearing and Imaging Techniques with Single-Cell Resolution: Toward Organism-Level Systems Biology in Mammals. *Cell chemical biology* **23**, 137-157 (2016).

95. A. Erturk *et al.*, Three-dimensional imaging of the unsectioned adult spinal cord to assess axon regeneration and glial responses after injury. *Nature medicine* **18**, 166-171 (2011).

96. M. Acar *et al.*, Deep imaging of bone marrow shows non-dividing stem cells are mainly perisinusoidal. *Nature* **526**, 126-130 (2015).

97. I. Espinosa-Medina *et al.*, Neurodevelopment. Parasympathetic ganglia derive from Schwann cell precursors. *Science (New York, N.Y.)* **345**, 87-90 (2014).

98. N. Oshimori, D. Oristian, E. Fuchs, TGF-beta promotes heterogeneity and drug resistance in squamous cell carcinoma. *Cell* **160**, 963-976 (2015).

99. M. Belle *et al.*, Tridimensional Visualization and Analysis of Early Human Development. *Cell* **169**, 161-173.e112 (2017).

100. K. Becker, N. Jahrling, E. R. Kramer, F. Schnorrer, H. U. Dodt, Ultramicroscopy: 3D reconstruction of large microscopical specimens. *Journal of biophotonics* **1**, 36-42 (2008).

101. S. K. Pal, J. Peon, A. H. Zewail, Biological water at the protein surface: dynamical solvation probed directly with femtosecond resolution. *Proceedings of the National Academy of Sciences of the United States of America* **99**, 1763-1768 (2002).

102. S. B. Zimmerman, A. P. Minton, Macromolecular crowding: biochemical, biophysical, and physiological consequences. *Annual review of biophysics and biomolecular structure* **22**, 27-65 (1993).

103. H. Giloh, J. W. Sedat, Fluorescence microscopy: reduced photobleaching of rhodamine and fluorescein protein conjugates by n-propyl gallate. *Science (New York, N.Y.)* **217**, 1252-1255 (1982).

104. M. E. Medina, C. Iuga, J. R. Alvarez-Idaboy, Antioxidant activity of propyl gallate in aqueous and lipid media: a theoretical study. *Physical chemistry chemical physics : PCCP* **15**, 13137-13146 (2013).

105. S. Rawat, C. Raman Suri, D. K. Sahoo, Molecular mechanism of polyethylene glycol mediated stabilization of protein. *Biochemical and biophysical research communications* **392**, 561-566 (2010).

106. K. Becker *et al.*, Reduction of Photo Bleaching and Long Term Archiving of Chemically Cleared GFP-Expressing Mouse Brains. *PloS one* **9**, e114149 (2014).

107. J. Beuthan, O. Minet, J. Helfmann, M. Herrig, G. Muller, The spatial variation of the refractive index in biological cells. *Physics in medicine and biology* **41**, 369-382 (1996).

108. B. Chance, H. L. Liu, T. Kitai, Y. T. Zhang, Effects of Solutes on Optical Properties of Biological Materials: Models, Cells, and Tissues. *Analytical Biochemistry* **227**, 351-362 (1995).

109. R. A. Meyer, Light scattering from biological cells: dependence of backscatter radiation on membrane thickness and refractive index. *Appl. Opt.* **18**, 585-588 (1979).

110. H. J. van Staveren, C. J. M. Moes, J. van Marie, S. A. Prahl, M. J. C. van Gemert, Light scattering in Intralipid-10% in the wavelength range of 400–1100 nm. *Appl. Opt.* **30**, 4507-4514 (1991).

111. G. Feng *et al.*, Imaging Neuronal Subsets in Transgenic Mice Expressing Multiple Spectral Variants of GFP. *Neuron* **28**, 41-51 (2000).

112. M. Ormo *et al.*, Crystal structure of the Aequorea victoria green fluorescent protein. *Science (New York, N.Y.)* **273**, 1392-1395 (1996).

113. O. Zhanmu *et al.*, Maintenance of Fluorescence During Paraffin Embedding of Fluorescent Protein-Labeled Specimens. *Frontiers in Neuroscience* **13**, (2019).

114. V. A. Sirotkin, M. D. Borisover, B. N. Solomonov, Effect of chain length on interactions of aliphatic alcohols with suspended human serum albumin. *Biophysical chemistry* **69**, 239-248 (1997).

115. A. M. dos Santos, Thermal effect on Aequorea green fluorescent protein anionic and neutral chromophore forms fluorescence. *Journal of fluorescence* **22**, 151-154 (2012).

116. C. Zhang, M. S. Liu, X. H. Xing, Temperature influence on fluorescence intensity and enzyme activity of the fusion protein of GFP and hyperthermophilic xylanase. *Applied microbiology and biotechnology* **84**, 511-517 (2009).

117. J. Mertz, J. Kim, Scanning light-sheet microscopy in the whole mouse brain with HiLo background rejection. *Journal of biomedical optics* **15**, 016027 (2010).

118. C. P. W. Schellinger Adam P., Solubility of buffers in aqueous-organic eluents for reversed-phase liquid chromatography. *Liquid Chromatography, Gas Chromatography* **22**, (2004).

119. H. R. Ueda *et al.*, Tissue clearing and its applications in neuroscience. *Nature reviews. Neuroscience* **21**, 61-79 (2020).

120. R. N. Day, M. W. Davidson, The fluorescent protein palette: tools for cellular imaging. *Chemical Society Reviews* **38**, 2887-2921 (2009).

121. J. Livet *et al.*, Transgenic strategies for combinatorial expression of fluorescent proteins in the nervous system. *Nature* **450**, 56-62 (2007).

122. S. Muyldermans, Nanobodies: natural single-domain antibodies. *Annual review of biochemistry* **82**, 775-797 (2013).

123. N. Tanaka *et al.*, Whole-tissue biopsy phenotyping of three-dimensional tumours reveals patterns of cancer heterogeneity. *Nature biomedical engineering* **1**, 796-806 (2017).

124. B. K. Garvalov, A. Erturk, Seeing whole-tumour heterogeneity. *Nature biomedical engineering* **1**, 772-774 (2017).

125. L. Manning, C. Q. Doe, Immunofluorescent antibody staining of intact Drosophila larvae. *Nature protocols* **12**, 1-14 (2017).

126. L. McGurk, H. Morrison, L. P. Keegan, J. Sharpe, M. A. O'Connell, Three-dimensional imaging of Drosophila melanogaster. *PloS one* **2**, e834 (2007).

127. S. Saghafi, K. Becker, C. Hahn, H. U. Dodt, 3D-ultramicroscopy utilizing aspheric optics. *Journal of biophotonics* **7**, 117-125 (2014).

128. S. Saghafi *et al.*, Image enhancement in ultramicroscopy by improved laser light sheets. *Journal of biophotonics* **3**, 686-695 (2010).

129. A. S. Chiang *et al.*, Three-dimensional mapping of brain neuropils in the cockroach, Diploptera punctata. *The Journal of comparative neurology* **440**, 1-11 (2001).

130. Y. C. Liu, A. S. Chiang, High-resolution confocal imaging and three-dimensional rendering. *Methods* **30**, 86-93 (2003).

131. P. S. Tsai *et al.*, Correlations of Neuronal and Microvascular Densities in Murine Cortex Revealed by Direct Counting and Colocalization of Nuclei and Vessels. *The Journal of Neuroscience* **29**, 14553-14570 (2009).

132. B. Hou *et al.*, Scalable and DiI-compatible optical clearance of the mammalian brain. *Frontiers in neuroanatomy* **9**, 19 (2015).

133. M. T. Ke, S. Fujimoto, T. Imai, SeeDB: a simple and morphology-preserving optical clearing agent for neuronal circuit reconstruction. *Nature neuroscience* **16**, 1154-1161 (2013).

134. T. Staudt, M. C. Lang, R. Medda, J. Engelhardt, S. W. Hell, 2,2'-thiodiethanol: a new water soluble mounting medium for high resolution optical microscopy. *Microscopy research and technique* **70**, 1-9 (2007).

135. I. Costantini *et al.*, A versatile clearing agent for multi-modal brain imaging. *Scientific Reports* **5**, 9808 (2015).

136. T. Kuwajima *et al.*, ClearT: a detergent- and solvent-free clearing method for neuronal and non-neuronal tissue. *Development (Cambridge, England)* **140**, 1364-1368 (2013).

137. T. Yu *et al.*, RTF: a rapid and versatile tissue optical clearing method. *Sci Rep* **8**, 1964 (2018).

138. M. T. Ke *et al.*, Super-Resolution Mapping of Neuronal Circuitry With an Index-Optimized Clearing Agent. *Cell reports* **14**, 2718-2732 (2016).

139. H. Hama *et al.*, ScaleS: an optical clearing palette for biological imaging. *Nature neuroscience* **18**, 1518-1529 (2015).

140. T. C. Murakami *et al.*, A three-dimensional single-cell-resolution whole-brain atlas using CUBIC-X expansion microscopy and tissue clearing. *Nature neuroscience* **21**, 625-637 (2018).

141. C. M. Hansen, *Hansen Solubility Parameters: A User's Handbook*. (CRC Press, 2007).

142. E. A. Susaki *et al.*, Versatile whole-organ/body staining and imaging based on electrolyte-gel properties of biological tissues. *Nature communications* **11**, 1982 (2020).

143. F. Tatsuki *et al.*, Involvement of Ca(2+)-Dependent Hyperpolarization in Sleep Duration in Mammals. *Neuron* **90**, 70-85 (2016).

144. S. I. Kubota *et al.*, Whole-Body Profiling of Cancer Metastasis with Single-Cell Resolution. *Cell reports* **20**, 236-250 (2017).

145. M. N. Economo *et al.*, A platform for brain-wide imaging and reconstruction of individual neurons. *eLife* **5**, e10566 (2016).

146. L. Wang *et al.*, The coding of valence and identity in the mammalian taste system. *Nature* **558**, 127-131 (2018).

147. D. Justus *et al.*, Glutamatergic synaptic integration of locomotion speed via septoentorhinal projections. *Nature neuroscience* **20**, 16-19 (2017).

148. R. A. Romanov *et al.*, Molecular interrogation of hypothalamic organization reveals distinct dopamine neuronal subtypes. *Nature neuroscience* **20**, 176-188 (2017).

149. D. Lanjakornsiripan *et al.*, Layer-specific morphological and molecular differences in neocortical astrocytes and their dependence on neuronal layers. *Nature communications* **9**, 1623 (2018).

150. D. L. Rousso *et al.*, Two Pairs of ON and OFF Retinal Ganglion Cells Are Defined by Intersectional Patterns of Transcription Factor Expression. *Cell reports* **15**, 1930-1944 (2016).

151. J. Y. Chen *et al.*, Hoxb5 marks long-term haematopoietic stem cells and reveals a homogenous perivascular niche. *Nature* **530**, 223-227 (2016).

152. M. F. Cuccarese *et al.*, Heterogeneity of macrophage infiltration and therapeutic response in lung carcinoma revealed by 3D organ imaging. *Nature communications* **8**, 14293 (2017).

153. F. M. Davis *et al.*, Single-cell lineage tracing in the mammary gland reveals stochastic clonal dispersion of stem/progenitor cell progeny. *Nature communications* **7**, 13053 (2016).

154. J. Li *et al.*, Single-Cell Lineage Tracing Reveals that Oriented Cell Division Contributes to Trabecular Morphogenesis and Regional Specification. *Cell reports* **15**, 158-170 (2016).

155. W. C. McFadden *et al.*, Perfusion fixation in brain banking: a systematic review. *Acta Neuropathologica Communications* **7**, 146 (2019).

156. K. G. Helander, Kinetic studies of formaldehyde binding in tissue. *Biotechnic & histochemistry : official publication of the Biological Stain Commission* **69**, 177-179 (1994).

157. P. B. Medawar, III.—THE RATE OF PENETRATION OF FIXATIVES. *Journal of the Royal Microscopical Society* **61**, 46-57 (1941).

158. B. Metz *et al.*, Identification of formaldehyde-induced modifications in proteins: reactions with model peptides. *The Journal of biological chemistry* **279**, 6235-6243 (2004).

159. B. Metz *et al.*, Identification of formaldehyde-induced modifications in proteins: reactions with insulin. *Bioconjugate chemistry* **17**, 815-822 (2006).

160. S. R. Sompuram, K. Vani, E. Messana, S. A. Bogen, A molecular mechanism of formalin fixation and antigen retrieval. *American journal of clinical pathology* **121**, 190-199 (2004).

161. T. Y. Leong, A. S. Leong, How does antigen retrieval work? *Advances in anatomic pathology* **14**, 129-131 (2007).

162. G. M. Halliday *et al.*, Distribution of substance P-like immunoreactive neurons in the human medulla oblongata: co-localization with monoamine-synthesizing neurons. *Synapse (New York, N.Y.)* **2**, 353-370 (1988).

163. J. A. Kiernan, Formaldehyde, Formalin, Paraformaldehyde And Glutaraldehyde: What They Are And What They Do. *Microscopy Today* **8**, 8-13 (2018).

164. P. Somogyi, H. Takagi, A note on the use of picric acid-paraformaldehyde-glutaraldehyde fixative for correlated light and electron microscopic immunocytochemistry. *Neuroscience* **7**, 1779-1783 (1982).

165. K. Seroogy *et al.*, Further analysis of presence of peptides in dopamine neurons. Cholecystokinin, peptide histidine-isoleucine/vasoactive intestinal polypeptide and substance P in rat supramammillary region and mesencephalon. *Experimental brain research* **72**, 523-534 (1988).

166. U. Homberg, N. T. Davis, J. G. Hildebrand, Peptide-immunocytochemistry of neurosecretory cells in the brain and retrocerebral complex of the sphinx moth Manduca sexta. *The Journal of comparative neurology* **303**, 35-52 (1991).

167. R. M. Hebert, A. M. Jackovitz, in *Wildlife Toxicity Assessments for Chemicals of Military Concern,* M. A. Williams, G. Reddy, M. J. Quinn, M. S. Johnson, Eds. (Elsevier, 2015), pp. 271-277.

168. D. Hopwood, Theoretical and practical aspects of glutaraldehyde fixation. *The Histochemical journal* **4**, 267-303 (1972).

169. E. Murray *et al.*, Simple, Scalable Proteomic Imaging for High-Dimensional Profiling of Intact Systems. *Cell* **163**, 1500-1514 (2015).

170. B. Yang *et al.*, Single-cell phenotyping within transparent intact tissue through whole-body clearing. *Cell* **158**, 945-958 (2014).

171. J. B. Treweek *et al.*, Whole-body tissue stabilization and selective extractions via tissue-hydrogel hybrids for high-resolution intact circuit mapping and phenotyping. *Nature protocols* **10**, 1860-1896 (2015).

172. R. Tomer, L. Ye, B. Hsueh, K. Deisseroth, Advanced CLARITY for rapid and high-resolution imaging of intact tissues. *Nature protocols* **9**, 1682-1697 (2014).

173. V. Gradinaru, J. Treweek, K. Overton, K. Deisseroth, Hydrogel-Tissue Chemistry: Principles and Applications. *Annual review of biophysics* **47**, 355-376 (2018).

174. S. Y. Kim *et al.*, Stochastic electrotransport selectively enhances the transport of highly electromobile molecules. *Proceedings of the National Academy of Sciences of the United States of America* **112**, E6274-6283 (2015).

175. F. Chen, P. W. Tillberg, E. S. Boyden, Optical imaging. Expansion microscopy. *Science (New York, N.Y.)* **347**, 543-548 (2015).

176. J. B. Treweek *et al.*, Whole-body tissue stabilization and selective extractions via tissue-hydrogel hybrids for high-resolution intact circuit mapping and phenotyping. *Nature protocols* **10**, 1860-1896 (2015).

177. T. Ku *et al.*, Multiplexed and scalable super-resolution imaging of three-dimensional protein localization in size-adjustable tissues. *Nature biotechnology* **34**, 973-981 (2016).

178. E. L. Sylwestrak, P. Rajasethupathy, M. A. Wright, A. Jaffe, K. Deisseroth, Multiplexed Intact-Tissue Transcriptional Analysis at Cellular Resolution. *Cell* **164**, 792-804 (2016).

179. Y. G. Park *et al.*, Protection of tissue physicochemical properties using polyfunctional crosslinkers. *Nature biotechnology*, (2018).

180. A. Greenbaum *et al.*, Bone CLARITY: Clearing, imaging, and computational analysis of osteoprogenitors within intact bone marrow. *Science Translational Medicine* **9**, eaah6518 (2017).

181. Y. Chen *et al.*, Three-dimensional imaging and quantitative analysis in CLARITY processed breast cancer tissues. *Scientific Reports* **9**, 5624 (2019).

182. A. E. Siegman, *Lasers*. (Oxford University Press, Mill Valley, CA, 1986, 1986).

183. R. Tomer, L. Ye, B. Hsueh, K. Deisseroth, Advanced CLARITY for rapid and high-resolution imaging of intact tissues. *Nat. Protocols* **9**, 1682-1697 (2014).

184. D. P. Ryan *et al.*, Automatic and adaptive heterogeneous refractive index compensation for light-sheet microscopy. *Nature communications* **8**, 612 (2017).

185. R. Tomer *et al.*, SPED Light Sheet Microscopy: Fast Mapping of Biological System Structure and Function. *Cell* **163**, 1796-1806 (2015).

186. M. V. Gomez-Gaviro *et al.*, Optimized CUBIC protocol for three-dimensional imaging of chicken embryos at single-cell resolution. *Development (Cambridge, England)* **144**, 2092-2097 (2017).

187. M. Stefaniuk *et al.*, Light-sheet microscopy imaging of a whole cleared rat brain with Thy1-GFP transgene. *Sci Rep* **6**, 28209 (2016).

188. C. J. Niedworok *et al.*, Charting monosynaptic connectivity maps by two-color light-sheet fluorescence microscopy. *Cell reports* **2**, 1375-1386 (2012).

189. F. F. Voigt *et al.*, The mesoSPIM initiative: open-source light-sheet microscopes for imaging cleared tissue. *Nature methods* **16**, 1105-1108 (2019).

190. K. Tainaka *et al.*, Whole-body imaging with single-cell resolution by tissue decolorization. *Cell* **159**, 911-924 (2014).

191. E. A. Susaki *et al.*, Advanced CUBIC protocols for whole-brain and whole-body clearing and imaging. *Nature protocols* **10**, 1709-1727 (2015).

192. P. J. Keller, A. D. Schmidt, J. Wittbrodt, E. H. Stelzer, Reconstruction of zebrafish early embryonic development by scanned light sheet microscopy. *Science (New York, N.Y.)* **322**, 1065-1069 (2008).

193. J. Huisken, J. Swoger, F. Del Bene, J. Wittbrodt, E. H. Stelzer, Optical sectioning deep inside live embryos by selective plane illumination microscopy. *Science (New York, N.Y.)* **305**, 1007-1009 (2004).

194. T. A. Planchon *et al.*, Rapid three-dimensional isotropic imaging of living cells using Bessel beam plane illumination. *Nature methods* **8**, 417-423 (2011).

195. B. C. Chen *et al.*, Lattice light-sheet microscopy: imaging molecules to embryos at high spatiotemporal resolution. *Science (New York, N.Y.)* **346**, 1257998 (2014).

196. Y. Wu *et al.*, Spatially isotropic four-dimensional imaging with dual-view plane illumination microscopy. *Nat Biotech* **31**, 1032-1038 (2013).

197. R. K. Chhetri *et al.*, Whole-animal functional and developmental imaging with isotropic spatial resolution. *Nature methods* **12**, 1171-1178 (2015).

198. J. Swoger, P. Verveer, K. Greger, J. Huisken, E. H. Stelzer, Multi-view image fusion improves resolution in three-dimensional microscopy. *Optics express* **15**, 8029-8042 (2007).

199. L. A. Royer *et al.*, Adaptive light-sheet microscopy for long-term, high-resolution imaging in living organisms. *Nature biotechnology* **34**, 1267-1278 (2016).

200. L. A. Royer, W. C. Lemon, R. K. Chhetri, P. J. Keller, A practical guide to adaptive light-sheet microscopy. *Nature protocols* **13**, 2462-2500 (2018).

201. D. Sage *et al.*, DeconvolutionLab2: An open-source software for deconvolution microscopy. *Methods* **115**, 28-41 (2017).

202. K. Becker *et al.*, Deconvolution of light sheet microscopy recordings. *Sci Rep* **9**, 17625 (2019).

203. M. Oheim, E. Beaurepaire, E. Chaigneau, J. Mertz, S. Charpak, Two-photon microscopy in brain tissue: parameters influencing the imaging depth. *Journal of neuroscience methods* **111**, 29-37 (2001).

204. A. Singh, J. D. McMullen, E. A. Doris, W. R. Zipfel, Comparison of objective lenses for multiphoton microscopy in turbid samples. *Biomedical optics express* **6**, 3113-3127 (2015).

205. A. Boniface, M. Mounaix, B. Blochet, R. Piestun, S. Gigan, Transmission-matrix-based point-spread-function engineering through a complex medium. *Optica* **4**, 54-59 (2017).

206. B. Choi *et al.*, Determination of chemical agent optical clearing potential using in vitro human skin. *Lasers in Surgery and Medicine* **36**, 72-75 (2005).

207. Z. Mao, D. Zhu, Y. Hu, X. Wen, Z. Han, Influence of alcohols on the optical clearing effect of skin in vitro. *Journal of biomedical optics* **13**, 021104 (2008).
208. J. Jiang, R. K. Wang, Comparing the synergistic effects of oleic acid and dimethyl sulfoxide as vehicles for optical clearing of skin tissuein vitro. *Physics in medicine and biology* **49**, 5283-5294 (2004).
209. C. Rylander *et al.*, Dehydration mechanism of optical clearing in tissue. *Journal of biomedical optics* **11**, 041117 (2006).
210. T. Yu, X. Wen, Q. Luo, D. Zhu, V. Tuchin, Quantitative analysis of dehydration in porcine skin for assessing mechanism of optical clearing. *Journal of biomedical optics* **16**, 095002 (2011).
211. D. Zhu, K. V. Larin, Q. Luo, V. V. Tuchin, Recent progress in tissue optical clearing. *Laser & Photonics Reviews* **7**, 732-757 (2013).
212. S. Johnsen, E. A. Widder, The Physical Basis of Transparency in Biological Tissue: Ultrastructure and the Minimization of Light Scattering. *Journal of Theoretical Biology* **199**, 181-198 (1999).
213. E. Lee *et al.*, ACT-PRESTO: Rapid and consistent tissue clearing and labeling method for 3-dimensional (3D) imaging. *Scientific Reports* **6**, 18631 (2016).
214. T. Boothe *et al.*, A tunable refractive index matching medium for live imaging cells, tissues and model organisms. *eLife* **6**, e27240 (2017).